INTERACTIONS BETWEEN NUCLEOID ASSOCIATED PROTEINS AND DNA IN THE PRESENCE OF MECHANICAL AND CHEMICAL FORCES

BY

KATELYN DAHLKE

DISSERTATION

Submitted in partial fulfillment of the requirements
for the degree of Doctor of Philosophy in Chemical Engineering
in the Graduate College of the
University of Illinois at Urbana-Champaign, 2019

Urbana, Illinois

Doctoral Committee:

Assistant Professor Charles E. Sing, Chair
Professor Aleksei Aksimentiev
Professor Charles M. Schroeder
Assistant Professor Diwakar Shukla

Abstract

The way that DNA is organized within a cell controls its physiological behavior. DNA must be condensed in order to fit into the much smaller cell, but must also be accessible to proteins responsible for biological processes. Architectural proteins assist with this large-scale arrangement of DNA to achieve the correct balance between these two competing requirements. The structural proteins that interact with DNA in prokaryotes are known as nucleoid associated proteins (NAPs). These proteins play a vital role in shaping the DNA and assist in many cell processes, including gene expression, replication, and transcription. NAPs have been studied extensively in order to elucidate how their physical properties (such as binding kinetics or DNA manipulation) aid in regulating cell function.

It has been shown in experiment and simulation that NAPs can adopt multiple binding states (i.e., the protein can be partially associated with its DNA substrate), which leads to complex binding and unbinding kinetics. For a simple binary system, where a protein can either be bound or unbound, the kinetics are relatively straightforward: there is a concentration dependent on-rate (k_{on}) and a concentration independent off-rate (k_{off}). When a protein-substrate complex has a non-binary set of bound states (including an intermediate "partially bound" state), other molecules in solution can impact the dissociation behavior. In fact, these competitors compete with the original protein for binding sites, which enhances the dissociation of the protein from its original substrate. This concentration-dependent dissociation is called "facilitated dissociation" (FD).

We have developed a coarse-grained model of a typical NAP-DNA system that is built up from local interactions, such as the mutlivalent binding that leads to FD as well as physical

deformations of DNA induced by protein binding. This methodical coarse-graining allows us to investigate the effect that these short-range interactions have on the mesoscale behavior of the system. We have investigated the cooperative and competing behavior of NAP-DNA interactions that result in concentration-, force-, and topology-dependent changes to both protein kinetics and physical DNA behavior. Our model qualitatively matches experimental observations, and provides a physical explanation for the observed behavior based on cooperative local interactions.

We demonstrate how the competition for binding sites along a DNA strand is affected by the energy barriers between the three possible bound states in the system (bound, partially bound, and unbound). This is the driving force behind facilitated dissociation; thus, changing the level of binding competition changes the dissociation behavior. Our model allows us to manually manipulate the binding energy landscape that other methods are unable to achieve. We can independently change the energy barriers between the three bound states, which in turn changes a protein's preferred bound state. This leads to three different concentration-dependent FD kinetic regimes: a concentration-independent off-rate, a linear dependence on c, and a combination of the two.

The multivalent binding also leads to multiple dissociation pathways: spontaneous and facilitated. The dissociation pathway a protein undergoes is dependent on a number of factors including force, the local geometric deformation, and protein concentration. We investigate how these factors impact the dissociation kinetics of a system that undergoes FD by expanding our model to account for the physical bends that NAPs induce in DNA upon binding in the DNA model, and also in the energy barrier landscape. At low forces, more proteins will be bound due to the more relaxed nature of the DNA strand that more easily allows local kinks caused by NAPs. As force is increased, there will be fewer bound proteins because of the more extended nature of the DNA strand, which is in a less preferential conformation. This force-enhanced unbinding and force-inhibited binding changes how a protein dissociates from DNA, either through FD at low force or spontaneously at high force. We observe two

two classes of dissociation: a classical "slip bond," where a bond weakens with force, and a "catch bond," where a bond is strengthened with force.

The physical deformation that NAPs cause affects not only the binding and unbinding kinetics; it also impacts the long-scale equilibrium and dynamic DNA elasticity. As more NAPs are bound to the DNA, there are more local kinks, decreasing the end-to-end distance of the single DNA strand. Because NAPs can adopt two possible binding states, DNA can undergo two different types of deformations. This leads to a non-monotonic effect of concentration on the force-extension behavior of the DNA strand. Our method allows us to study non-equilibrium elastic behaviors as well, such as DNA extending dynamically. The competition between the two characteristic time scales of the system (unbinding time and pulling time) leads to extension-rate dependent effects on both DNA elasticity and binding behavior.

We are able to show that NAPs help stabilize DNA supercoils due to these same local, cooperative effects. DNA supercoiling occurs when DNA wraps around itself to relieve torsional stress. Both DNA supercoiling and NAPs are present in prokaryotic cells, but the role of NAPs in supercoiling activity is not fully understood. Our model demonstrates that NAPs are more likely to bind to supercoiled DNA, due to the protein's preference to bind to already-bent DNA, which in turn stabilizes the supercoil. This leads to a concentration-dependent change of the phase transition between extended and supercoiled DNA in the force-torque ensemble. We are able to use a combination of simulation data and theoretical predictions of the various energies of the system, such as the stretching, bending, and excluded volume energies, as a function of both force and concentration. This information can be used to develop a theory that provides a thorough understanding of how NAPs affect DNA supercoiling.

This work has been based on single-molecule studies ($\approx 1\ \mu$m) but is capable of extending to much longer length scales. Other NAPs and their local effects on DNA can be added to the system in the same way that FIS has been used in this work. We can understand the effect that these proteins have on the mesoscale behavior of DNA, and these mesoscale behaviors in turn affect the large-scale structure and organization of the nucleoid.

To my grandpa, for his unwavering support of all my endeavors
and to my sisters

Acknowledgments

First and foremost, I would like to thank my advisor Prof. Charles Sing for convincing me to take a chance on computational research. He has been a supportive presence during my time at the University of Illinois, knowing just how hard to push me and encouraging me every step of the way. I appreciate everything he has done for me at Illinois, and I would not be the scientist I am today without his guidance and mentorship.

I also wish to thank the faculty members who have served on my committee, Drs. Charles Schroeder, Diwakar Shukla, Mary Kraft, and Aleksei Aksimentiev. I am grateful to other faculty in the chemical engineering department, especially Drs. Simon Rogers and Damien Guironnet, for mentorship and support during my graduate career. I am also appreciative of the funding I received while at Illinois: the Chemical Biology Interface Training Program Grant, the Harry G. Drickamer Fellowship, and the Mavis Future Faculty Program Fellowship.

I want to extend my profound gratitude to the members of the Sing group for their camaraderie. To the original group members, Michael, Mithun, and Tyler, thank you for being part of a wonderful start to graduate school and making it a true pleasure to come to work and struggle alongside you. Tyler, thank you for being the best coworker I could have possibly asked for from the beginning to the end. Jason and Charlie, I am so grateful for the entertaining conversations that made our offices fun. Gary, Sarit, Tianyuan, and Lili, I am grateful for the new energy you brought into the group. To my incredibly talented undergraduate, Jing, thank you for your hard work and dedication.

To the many, many others who have made a huge impact on my life at Illinois, thank

you for letting me grow as a person and have a fulfilling life. To David, thank you for your patience while teaching me programming basics and helping me write my initial code. To Maggie Metzger, thank you for answering all of my inane questions and going above and beyond on a regular basis. To the Legends dinner group, especially Arif, Becca, and Anthony, thank you for your friendship and acquaintanceship. To the rouge book club, Megan, Lexi, Pranjali, Angeli, and Maggie, you are the group of girlfriends I hoped I would have in my lifetime; I am grateful I met you all and even more thankful that you forgave me time and again for failing to actually read the assigned book. To the many other graduate students I have met through the ChBE department, GradSWE, and ENVISION, thank you for making my experience here an incredibly satisfying one.

I would not be where I am today without the support from mentors in my past, especially Jay Kuecker, Rick Lindeman, Eric Mandernach, Drs. Maria Santore and Jen Heinen. Thank you for your belief in me.

To Danielle, thank you for everything you have done for me, from midday coffee runs to picnic lunches to panicked midnight messages. You are the person I can turn to for advice of any kind, and I am so grateful that our time at Illinois overlapped. To Brendan, thank you for teaching me how to solve a Rubik's cube, feeding me on a regular basis, and keeping me functional when that seemed like an insurmountable task. Every moment with you makes my life better. To my family, thank you for your love and support during the entirety of my educational journey. Lastly, I want to thank my cats, Toothless and Pixel. While they are mediocre sounding boards and scientific assistants, they bring a little bit of joy and love into my life every day, and I would not have made it through graduate school without them.

Table of Contents

Chapter 1

Introduction

Structure and function in biology are closely related. This concept is typically applied to proteins, but it extends to other biomolecules as well, including DNA. DNA organization within a cell is critical for proper cell function, and in order to have a full understanding of cell physiology, there must be a full understanding of how DNA is physically structured and organized. This organization occurs on multiple levels, from the full genome all the way down to the base-pair level. Because of the many orders of magnitude that play a role in DNA organization, **there is a challenge to comprehensively study the hierarchical structure of DNA within a cell.**

1.1 Scales of DNA Organization

DNA has millions or billions of base pairs for prokaryotic or eukaryotic cells, respectively [1]. As such, DNA is anywhere from 500-50,000 times longer than the cell itself, and requires significant compaction in order to fit within the cell. In eukaryotic cells, chromosomal DNA is stored in the membrane-enclosed nucleus, while in prokaryotic cells, a circular plasmid is stored in the analogous membrane-less nucleoid. Within these structures, DNA can be condensed in a number of different ways, including looping, compartment segregation, and supercoiling [2–11], which can be seen in Fig. 1.1A and B.

Compartmentalization occurs between megabase segments of DNA that are loosely interacting, yet their relative locations are strongly correlated [7, 12–14], shown by the light gray and white checkerboard pattern in a sample Hi-C contact map shown in Fig. 1.1A [8]

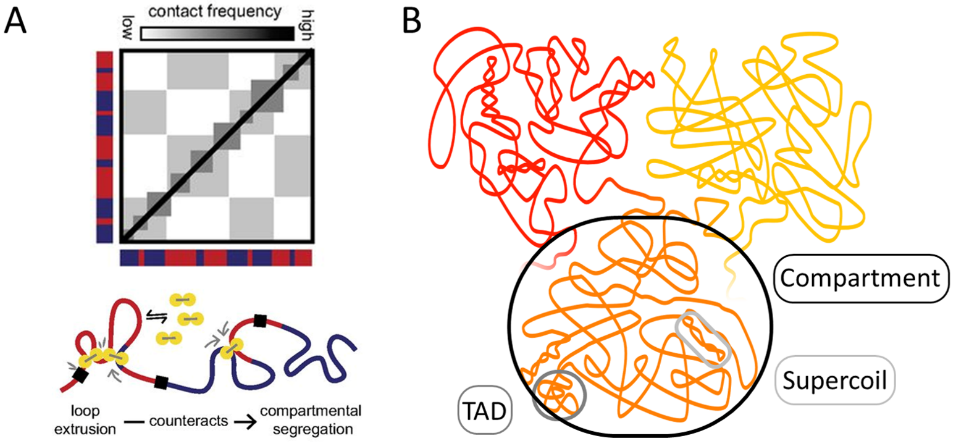

Figure 1.1: **A.** A cartoon showing how compartments and TADs are differentiated using a Hi-C contact map [8]. TADs are identified via the dark gray squares along the diagonal of the contact frequency box and shown by the close-contact red loops in the cartoon below. Compartments are the light-gray checkerboard pattern, and are denoted by the different colored strands in the cartoon below. **B**. A schematic showing the relationship between compartments, TADs, and supercoils.

and the black circled region in the schematic in 1.1B. These compartments have genetic and epigenteic features in common, such as overall contact frequency (low or high), amount of coded DNA and frequency of gene expression [5, 7]. The exact mechanism of compartment formation and physiological effects are still in question.

One mechanism that affects compartment organization is DNA looping, where two distant sites along the DNA backbone are connected by some molecular bridge. This leads to the formation of topologically associated domains (TADs), which are "locally" associated domains on the order of $\sim 10 - 100$ kb with sharp, well-defined boundaries that often correspond to transcription start sites or other protein-specific binding sites [4, 6, 15]. These domains are often defined using contact maps, where these domains can be found along the diagonal of the contact map (shown by the dark gray squares in Fig. 1.1A [8]) and are smaller than compartment regions (see Fig. 1.1B). The organization at this length scale affects a number of biological processes. For example, loops can act as gene regulators, since two distant sites, such as a gene enhancer and a gene promoter can be brought in close proximity in order for a gene to be expressed [16]. By changing loop formation, different promoters might interact with a given enhancer, which will change how or what genes are expressed. Loop extrusion simulations (where loops are actively lengthened or shortened) has been shown to affect both TADs and compartment organization [8].

Supercoiling occurs when twists are either added or removed from DNA (positively or negatively supercoiled, respectively), which torsionally stresses the DNA strand. To relax, DNA wraps around itself, which consequently decreases the end-to-end distance of the DNA strand. DNA is negatively supercoiled in both prokaryotic and eukaryotic cels, meaning that there are fewer twists in the DNA that completely relaxed DNA (fewer than 1 turn for every 10.5 base pairs) [17–19]. This assists in processes that require the DNA strand to “unzip,” such as gene expression and replication [19–22]. These same processes generate positively supercoiled DNA when the two strands are separated, adding twists to the flanking dsDNA [23, 24]. Supercoiling topology is modulated by polymerases [17, 25] and topoisomerases [17, 26]. Supercoiled domains can be found within TADs [17, 27, 28] and compartments can contain different levels of supercoiling [29].

While these mechanisms can significantly compact the DNA, DNA must simultaneously be transiently accessible to DNA-binding proteins such as helicases, polymerases, topoisomerases, transcriptases, and transcription factors that must bind to DNA in order to carry out their physiological function. These proteins can bind and unbind from DNA, and even move along the DNA strand as needed. These behaviors are inherently dynamic, where different sections of DNA will need to be accessible at different times under different conditions. One example of this is DNA replication in prokaryotic cells [30]. When cells are in the exponential growth phase where they are rapidly dividing, DNA will need to be replicated more often than cells in the stationary or death phase. The origin of replication ($oriC$) needs to be accessible to DNA helicases that bind to double stranded DNA (dsDNA) and disrupt the hydrogen bonds. This breaks apart the strand into two single-strands of DNA (ssDNA) to prepare for DNA polymerase binding and subsequent DNA synthesis. Consequently, DNA near this newly formed ssDNA is overtwisted, and proteins such as topoisomerases can assist in relaxing the newly torsionally stressed DNA. All of these interactions are highly cooperative and dynamic, and these proteins require uninhibited access in order to act on the DNA. **There is an inherent competition between the need to significantly compact DNA in a cell and the need for sections of DNA to be readily accessible.** In order to achieve the perfect balance between these two requirements, architectural proteins bind to DNA and and assist in the long-scale structuring of DNA that satisfies the need for both compaction and accessibility.

1.2 Nucleoid Associated Proteins

Architectural proteins known as nucleoid associated proteins (NAPs) are responsible for the hierarchical genome structure in prokaryotic cells [31]. These proteins bind to DNA non-specifically, although there are some preferred sequences for individual proteins. Upon binding, NAPs manipulate both the short- and long-scale DNA structure by bending, twisting, and looping [32–46]. These effects that occur at the scale of a single protein-DNA complex ($\approx$ 15-30 base pairs, or 5-10 nm) or between two distant DNA sites (DNA-NAP-DNA) via looping, are responsible for the structure of the overall genome; however, the exact mechanism by which this happens is not understood. These proteins are not solely structural; they play a role in different biological processes, such as gene expression [32, 38, 47–51], DNA transcription [32, 41, 52–55], and replication [32, 56, 57].

NAPs are analogous to histones that wrap and organize DNA within eukaryotic cells, although there are some notable differences which can be seen in the example crystal structures seen in Fig. 1.2A-D. A histone octamer, composed of two of each of the histones H2A, H2B, H3, and H4, has a molecular weight of $\approx$ 110 kDa and forms a disk-like complex. DNA is wrapped twice around this short, cylindrical core, leading to a nucleosome core that binds $\approx$ 140 base pairs of DNA, shown in Fig. 1.2A [59, 61]. NAPs are significantly smaller than histones ($10 - 20$ kDa), often found in a dimer form with two arms that fit into the grooves

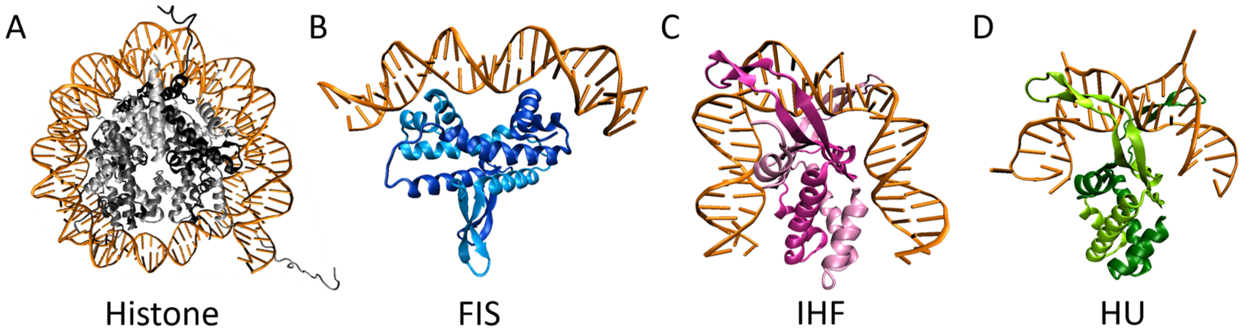

Figure 1.2: Crystal structures of architectural proteins created with VMD [58]. **A.** Crystal structure of a eukaryotic nucleosome, with the histone octamer shown in grayscale and wrapped DNA in orange [59]. **B.** Structure of the homodimer NAP FIS (blue) and DNA binding site (orange) [44]. **C.** Structure of the heterodimer NAP IHF (pink) and DNA binding site (orange) [41]. **D.** Structure of a homodimer HU (green) and DNA binding site (orange) [60]. HU can also be found in a different homodimer form, as well as a heterodimer form.

of DNA. As a result, NAPs bind to a much shorter section of DNA ($\approx 15-30$ base pairs) than histones. Crystal structures of typical NAP-DNA complexes that demonstrate this can be seen in Fig. 1.2B-D [41, 44, 60]. Both of these classes of architectural proteins can link distant sites of DNA, via linker histones in eukaryotes and NAP-NAP or DNA-NAP-DNA interactions in prokaryotes [62–64].

Additionally, the histone core is relatively conserved throughout eukaryotic cells, where all nucleosomes behave in a relatively similar manner. In the many different types of prokaryotic cells, there are a large number of NAPs, each of which have different binding properties and biological functions [32–38, 40, 50, 51, 66, 66–68]. Some of the most prevalent NAPs in prokaryotes include factor for inversion stimulation (FIS) [42, 45, 46, 53, 57, 69], histone-like protein (HU) [43, 54, 60, 70], integration host factor (IHF) [41, 49, 71], histone-like nucleoid-structuring protein (H-NS) [47, 72–75], DNA protection during starvation (Dps) [76, 77], and StpA [78, 79], although this list is non-exhaustive. FIS, IHF, and IU complexed to DNA can be seen in Fig. 1.2B-D, respectively. Many of these proteins are conserved over different genuses and species. Their physiological and architectural roles, as well as their different levels within the in the cell are summarized in Table 1.1. Each NAP in Table 1.1 is natively found in either a homo- or hetero-dimeric form, and some of these NAPs, such as Dps or

Table 1.1: A non-comprehensive summary of the most widely-studied NAPs. These proteins can wrap DNA like histones in eukaryotes, bend DNA, or connect two DNA strands and form a type of “bridge” between them. Their concentrations within the cell vary with growth conditions, which corresponds well with their physiological roles [35, 65].

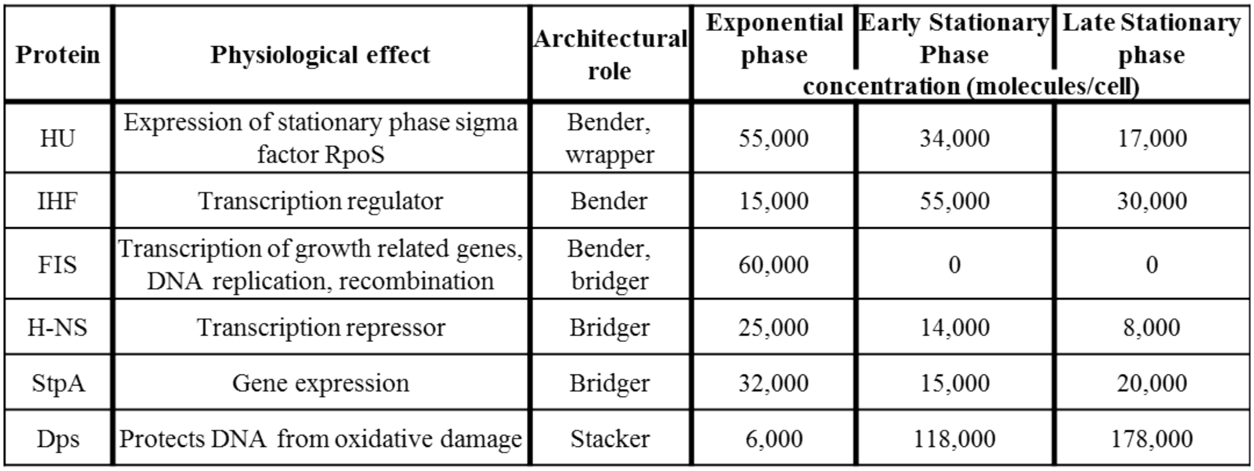

Protein	**Physiological effect**	**Architectural role**	**Exponential phase**	**Early Stationary Phase**	**Late Stationary phase**
			concentration (molecules/cell)		
HU	Expression of stationary phase sigma factor RpoS	Bender, wrapper	55,000	34,000	17,000
IHF	Transcription regulator	Bender	15,000	55,000	30,000
FIS	Transcription of growth related genes, DNA replication, recombination	Bender, bridger	60,000	0	0
H-NS	Transcription repressor	Bridger	25,000	14,000	8,000
StpA	Gene expression	Bridger	32,000	15,000	20,000
Dps	Protects DNA from oxidative damage	Stacker	6,000	118,000	178,000

HU, can een form higher ordered structures [77, 80]. This is a common trait amongst NAPs, although it is not necessarily a requirement for a protein to be classified as a NAP. While NAPs have been studied for several decades, new NAPs and the physical and physiological roles that they play in the cell are still being discovered [81–84].

1.2.1 Extreme length-scales and time scales for NAP study

There are many *in vivo*, *in vitro*, and *in silico* methods that are currently used to study NAP-DNA interactions, and these interactions generally fall into one of two extremes: near-atomistic scale and near-nucleoid scale, examples of which are shown in Fig. 1.3. Information about the local, static structure of a NAP-DNA complex can be obtained experimentally via x-ray crystallography, which is available for a large number of NAPs listed in Table 1.1 and shown in Fig. 1.2 [41–46]. This provides insight into the structure of the protein, such as whether or not it is an oligomer, which amino acids are critical to binding, and the size of the binding site, as well as the local effect it has on DNA, such as strand breakages, bending deformations, and twisting deformations [32].

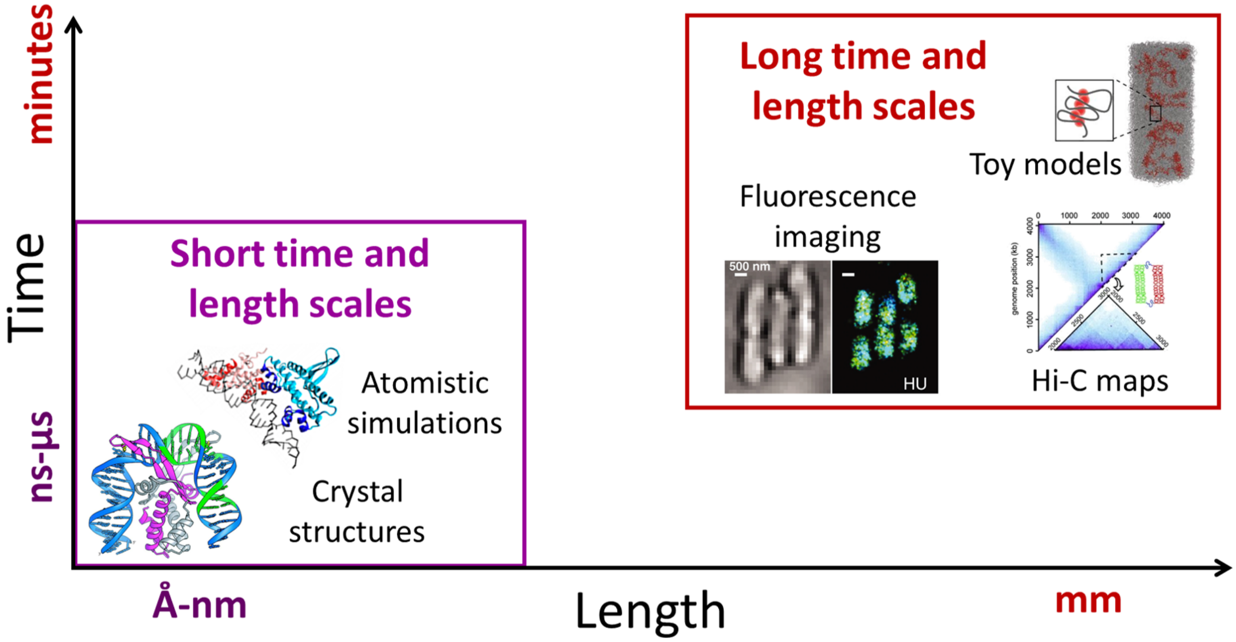

Figure 1.3: NAP-DNA interactions are studied at a range of length scales, including two limiting cases: short time and length scales (lower left, purple box) and long time and length scales (upper right, red box). Crystal structures and atomistic simulations can provide information about the local interactions between NAPs and DNA (on the order of nm and ns) [43, 85]. At the other extreme, fluorescence imaging of the cell, toy simulation models, and Hi-C contact maps provide information of NAP-DNA interactions at the full genome level [88, 94, 95].
Atomistic simulation image adapted with permission from Tsai *et al.* [85], copyright 2016 American Chemical Society. Fluorescent image adapted from Wang, *et al.* [88], reprinted with permission from AAAS. Toy model figure adapted from Naumova, *et al.* [94], reprinted with permission from AAAS. Hi-C map adapted from Le, *et al.* [95], reprinted with permission from AAAS.

In order to get at non-static information at this scale, one can turn to atomistic simulations that are able to provide information about the binding mechanisms and the dynamics of the protein at very short time scales (<microseconds) [45, 55, 69, 85, 86, 86, 87]. While these types of simulations are able to supply information at the angstrom to nm level, there is a consequential computational cost to extend them to longer time or length scales. Even with significant computational power, atomistic simulations are computationally intractable on nucleoid-relevant time and length scales (>seconds and >microns).

In contrast to very small-scale effects that are studied, experimentalists can use microscopy to study the full-scale nucleoid [88–93]. These studies are useful to understand the long-scale effects of NAPs and how they might be generally clustered within the nucleoid as a function of global changes to the cell. This can include experiments such knockout studies, where an entire type of NAP is no longer present in the cell [88], or cells that are subjected to external stressors [94]. However, there are limitations due to imaging constraints where local NAP-DNA interactions cannot be resolved. Large scale, phenomenologically motivated simulation or theoretical models can also be used to describe large-scale nucleoid behavior, but these models are far removed from the small-scale physical properties of a real nucleoid [94, 96, 97]. Hi-C maps, showing contacts throughout the entire genome, are created using a combination of experimental and computational techniques and can show the effect that large-scale changes to NAP-DNA interactions have on the structure of the nucleoid [95, 98].

1.2.2 Bridging the gap

The studies done at extreme time and length scales provide valuable information about NAP-driven structuring of DNA, but **there exists a big challenge to connect and understand the relationship between the two disparate length scales**. However, there are some promising tools that are able to address this mesoscale region. Single molecule experiments can start to bridge the gap by studying longer time and length scales (1-10 microns and >seconds) [39, 64, 67, 68, 75, 86, 99–103]. Initial efforts in the literature to study NAP-DNA complexes have revealed a rich set of physical behaviors that emerge at the mesoscale, and are expected to play an important role in biological function.

Single molecule experiments have demonstrated that NAP-DNA complexes are stable, where proteins stay bound for very long periods of time (>minutes to hours) [39, 68, 100]. However, when other molecules such as short DNA oligomers or DNA-binding proteins (such as NAPs or other transcription factors) are introduced into solution, the dissociation rate increases [99, 100, 104, 105], shown by the sample fluorescent images and related data in Fig. 1.4A-B. Initial studies using structurally distinct proteins FIS, HU, and NHP6A found that the dissociation rate depended linearly on the protein concentration in solution [99],

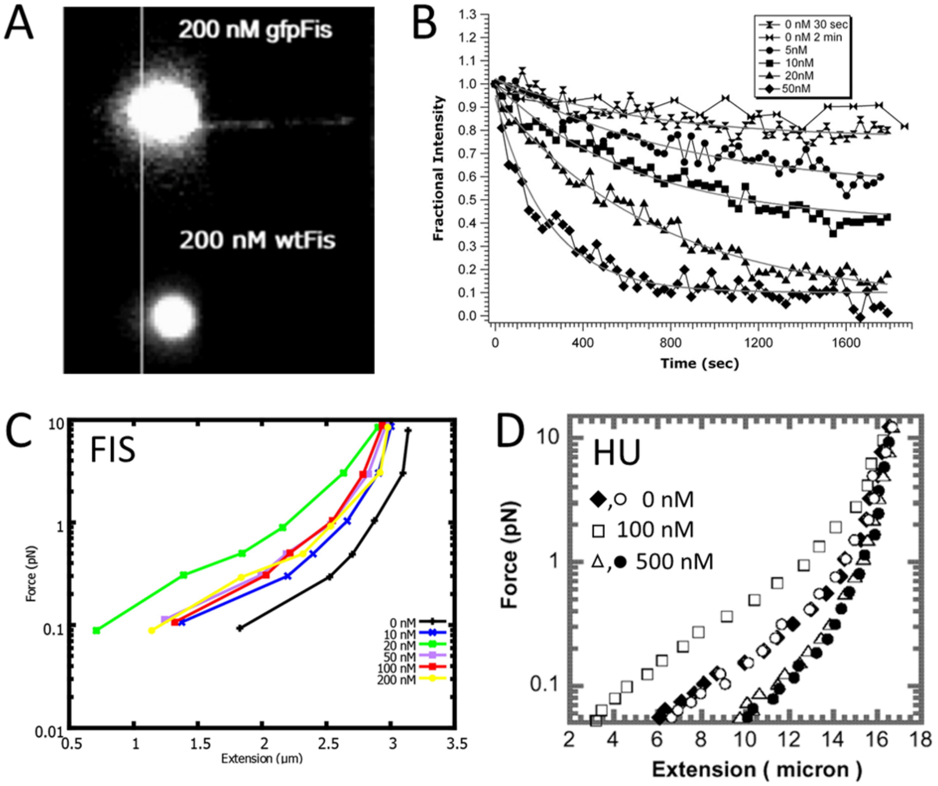

Figure 1.4: Sample figures from NAP-DNA single molecule experiments. **A.** A sample fluorescence image from a protein exchange experiment, where DNA is coated with gfp-tagged FIS proteins (top) that then undergoes an exchange with untagged FIS proteins in solution (bottom) [99]. **B.** From experiments like those shown in panel (A), the fluorescence as a function of time and concentration can be measured, which provides the dissociation rate of proteins as a function of solution concentration [99] **C.** The force-extension behavior of DNA as a function of FIS concentration [100]. The extension shifts to a higher force as c is increased to 20 nM (green line) and decreases as c is increased to 200 nM (yellow line). **D.** DNA force extension as a function of HU concentration [39]. With a concentration of 100 nM, there is an increase in the force. However, when $c = 500$ nM, there is a stiffening effect where the force at a given extension is lower than the case for bare DNA.

Panels (A) and (B) adapted from Graham *et al.* [99], by permission of Oxford University Press. Panel (C) reprinted from Giuntoli, *et al.* [100], with permission from Elsevier. Panel (D) adapted with permission from Skoko, *et al.* [39], copyright 2004 American Chemical Society.

while later studies demonstrated that the dissociation rate was linearly dependent on the concentration DNA oligomers in solution at low c, while concentration-independent at high c [100]. This "facilitated dissociation" phenomena (named so because a molecule in solution *facilitates* the dissociation of a protein bound to its substrate) is thought to occur due to the nmultivalent binding nature of these proteins, i.e. they are not limited to a simple, binary on or off state. A third "partially associated" conformation has been supported by both *in vitro* and *in vivo* experiments [99, 100, 104, 105], coarse grained models [106], and atomistic simulations [85].

This three-state binding landscape leads not only to complex binding and unbinding kinetics, but also multiple effects on DNA elasticity. Structures of NAP-DNA complexes (some of which can be seen in 1.2B-D) demonstrate that NAPs strongly deform the local structure of DNA [41, 43–45, 57, 60]. In fact, NAPs can induce degrees of bending at the binding site up to 160° [43, 44, 46]. Consequently, several NAPs bound along the DNA change end to end distance of a DNA strand, which can be measured in a typical optical tweezers or magnetic bead experimental set up [39, 67, 75, 86, 100, 103, 107]. The DNA can become more compact when there are high degrees of bending along the contour length [39, 100] or can become more stiff (no degree of bending with extra rigidity) [67, 68, 102, 108]. For a system with a single binding state, there would be a single trend in extension behavior as a function of protein concentration (i.e., as more bending proteins are added, the more the DNA will compact until the strand is saturated). However, NAPs have generally demonstrated non-monotonic extension behaviors (i.e., there is an initial decrease in extension and an increase in extension as the DNA strand becomes saturated) shown in Fig. 1.4C and D, due to the bound and partially bound states these proteins can adopt [67, 71, 100].

These local bends caused by NAPs can also impact tertiary DNA structures, like large-scale writhes that occur when DNA is supercoiled. NAPs are thought to affect DNA supercoiling since both are present *in situ* [10, 80, 112, 113]; however, the way that NAPs help form and stabilize these writhes is not understood.

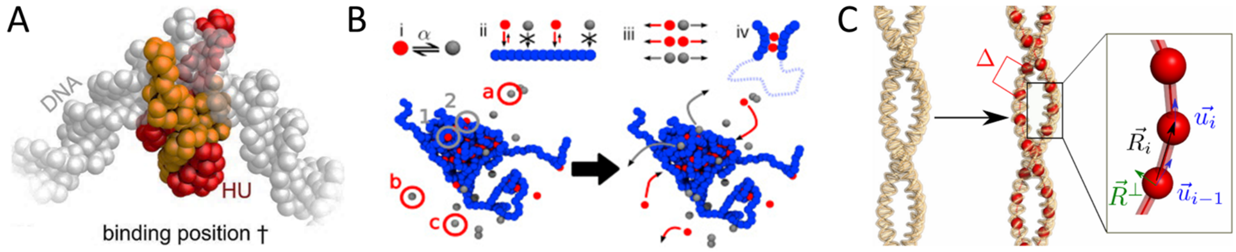

Figure 1.5: Sample simulation snapshots from coarse-grained models. **A.** A coarse grained model of DNA (3 beads per base, white) and HU (1 bead per amino acid, red and orange) that demonstrates how HU slides along DNA to find a binding site [109]. **B.** A bead-spring model of a chromatin fiber (blue) with active and inacive proteins (red and blue, respectively) that can bind to two chromatin beads [110]. **C.** A multi-scale coarse-grained model of DNA that can demonstrate DNA supercoiling at multiple length scales controlled by Δ [111].
Panel (A) reprinted with permission from Tan, *et al.* [109], copyright 2016 American Chemical Society. Panel (B) reprinted from Brackley, *et al.* [110], with permission from Elsevier. Panel (C) reprinted from Krajina, *et al.* [111], with permission from Elsevier.

This level of behavior can also be investigated using coarse-grained computational models [114, 115]. One commonly used model is the 3 sites per nucleotide (3SPN) model developed by the de Pablo group [116–118]. Proteins can be similarly coarse-grained based on atomic interactions to a single bead per amino acid (AICG model) [119]. Simulations utilizing this level of coarse-graining have been used to study dynamic NAP-DNA interactions, such as NAPs searching for a binding site along a short strand of DNA (35 bp), shown in Fig. 1.5A [109]. DNA up to a length of ~ 1 μM can be simulated with this method, which is on the same length scale as experimental single molecule studies [116]. However, a system with several NAPs and a DNA of this length, let alone on the scale of the nucleoid ($\sim$ mm), is not computationally tractable.

DNA can also be coarse-grained to a much further extent, where many base pairs are modeled as a single bead. The short-scale detail is removed (such as specific sequence and double helix shape), but retains the appropriate long-scale behavior [111, 120, 121]. This type of coarse-graining has been used extensively to study eukaryotic chromatin [110, 122–130] and mesoscale behavior of DNA [111, 131]. Snapshots from a simulation showing DNA binding proteins interacting with chromatin [110] and multiscale modeling of DNA supercoiling [111] can be seen in Fig. 1.5B-C, respectively. While this ultra coarse-grained method has provided a number of insights into the mesoscale behavior of the eukaryotic genome, it has not extended to the analogous, yet distinct, NAP-DNA systems. **There is a significant need to develop methods to study the intermediate time and length scales of NAP-DNA interactions that can be extended to the full size of the nucleoid.**

1.3 Dissertation Overview

In this work, we have developed a model of DNA and NAPs that is capable of investigating mesoscale phenomena while maintaining the importance of local interactions. We utilize FIS as a model NAP due to the extensive work in the literature ranging from atomistic simulations to *in vivo* studies [44–46, 53, 57, 85, 99, 100, 104]. This model incorporates a multi-state binding landscape and the geometric deformations of DNA in the NAP-DNA complex, specifically the bending that occurs. We are able to investigate the concurrent effects that this has on the NAP binding and unbinding kinetics, DNA elasticity, and DNA topology.

In Chapter 1, we investigate the effect that the binding energy landscape has on the large-scale dissociation of NAPs from DNA. Prior work had investigated symmetric energy barriers between states and focused on the effect that external concentration of proteins have on facilitated dissociation [106]. By independently changing the energy barriers between bound states (bound, partially bound, and unbound), and thus changing how a protein prefers to be bound to its DNA substrate, we observe a range of different types of concentration-dependent dissociation kinetics, including a concentration-independent off-rate, a linear dependence on c, and a plateauing off-rate. We are able to show how these non-symmetric energy barriers contribute to different dissociation kinetics by looking at the cooperative behavior of individual proteins in our system. Our model is capable of qualitatively matching experimentally observed kinetics [99, 100, 104], and extends the understanding of what is occurring in systems undergoing facilitated dissociation.

In Chapter 2, we continue our investigation into facilitated dissociation by studying how other external factors, specifically force, can impact the dissociation kinetics. To do this, we incorporate the fact that NAPs physically deform DNA via bending into the simulation model and also in the binding/unbinding energy landscape. Because proteins bend the DNA, there will be more bound when DNA is relaxed and can easily adopt many local kinks. As DNA becomes more straight, there are fewer proteins bound because DNA is biased away from the preferred bent conformation. This behavior is ensured by increasing the energy barrier for binding and a lowering the energy barrier for unbinding as more force is applied.

If we consider a single NAP-DNA complex, this force-dependence has a straightforward consequence on the unbinding kinetics: proteins dissociate more quickly as more force is applied. This is the classical "slip bond," where a bond weakens with force. However, when we consider NAP-DNA complexes in a field of competitor proteins, the dissociation kinetics become more complicated. The competing molecules are inhibited from binding, which means that facilitated dissociation is inhibited, slowing down the overall dissociation as force is increased. This phenomena is known as a "catch bond," where a bond lifetime is extended with force. We are able to demonstrate an extrinsic catch bond, where the individual bonds are weakened, but the overall dissociation behavior slows with applied force. This complex dissociation is dependent on a number of factors, including geometric deformation, concentration, and how strongly different energy barriers are dependent on force.

The physical deformation that NAPs cause does not only affect the binding and unbinding kinetics; it also impacts the long-scale DNA elasticity, which we discuss in Chapter 3. As more NAPs are bound to the DNA, there are more local kinks, decreasing the end-to-end distance of the single DNA strand. However, due to the multiple binding states that NAPs can adopt (partially bound, fully bound, or two partially bound at one binding site), there are multiple deformations that DNA can undergo, making the effect of concentration on the force-extension behavior of the strand non-monotonic. We see semi-quantitative matching of our simulated force-extension behavior to reported experimental data [100]. Because we use a coarse-grained Brownian dynamics simulation, we can investigate non-equilibrium behaviors, such as the dynamic extension of a DNA strand. Different time scales of the system, such as the pulling time and unbinding time, work in tandem to affect the NAP-DNA system. When these two characteristic time scales are similar, we see extension rate dependent changes in the system, which includes the force required to extend the DNA strand and the number of bound proteins. This suggests that the relative time scales of dynamic processes play a role in NAP-DNA systems.

Lastly, in Chapter 4, we look at the behavior that NAPs have on DNA topology, specifically DNA supercoiling. The occurs when DNA is torsionally stressed and forms large-scale writhed structures by wrapping around itself to relieve this stress. As mentioned earlier, DNA is naturally supercoiled in prokaryotic cells and has been extensively studied in experiment, simulation, and theory [111, 131–135]. However, the role that NAPs play in supercoil formation or stabilization has not been as thoroughly investigated. Our coarse-grained model can look at DNA supercoiling in the presence of NAPs. Proteins are more likely to bind to DNA in the supercoiled state due to the preference for DNA in bent conformations, and this in turn stabilizes the DNA supercoil. We demonstrate a concentration-dependent change of the force and torque necessary to form DNA supercoils. This shifts the phase transition between extended and supercoiled DNA to a higher force at a given torque, enabling the formation of supercoils at lower τ.

Simulations provide information about the system, such as the extension behavior, bending energy, and excluded volume for extended and supercoiled DNA that is dependent on both concentration and force. This in turn informs theory that provides a rigorous, physical understanding of how NAPs affect supercoiling behavior. We are able to demonstrate qualitative matching between our simulations and theory, which can inform how DNA supercoiling might be impacted by other proteins or external factors in the cell.

Chapter 2

Facilitated dissociation kinetics of dimeric nucleoid-associated proteins are described by a universal curve[i]

2.1 Introduction

Physical interactions between proteins and DNA are an important and persistent area of scientific interest [32, 136–138]. A full understanding of these behaviors requires an accounting of how DNA and proteins work together or compete at a molecular level. These connections govern cellular processes, such as mRNA transcription [32, 41, 52–55], gene expression [32, 38, 47, 48], and cell division [32, 56]. An important example of this is the interplay between genomic DNA and nucleoid associated proteins (NAPs) in prokaryotes [51, 65, 71, 72, 77, 104]. Increased understanding about the role of proteins in the nucleoid has led to an appreciation of the wide variety of behavior, both physical and biological, among NAPs [32, 34, 38]. NAPs are required for cell processes to occur, often relying on their ability to manipulate nucleoid architecture; however, the exact mechanisms involved in these processes are still not fully understood [32, 33, 36, 40, 139].

The properties of the bound NAP-DNA complex has been extensively studied, due to the importance of NAP-DNA interactions [39, 42, 57, 68, 69, 73, 140, 141] and binding kinetics [103, 104] in determining cell physiology. Experimental work has demonstrated that once NAPs are bound to DNA, they are typically stable and stay bound for long periods of time in the absence of other molecules, such as freely diffusing proteins or protein-free DNA [39, 68, 100]. The presence of these molecules, however, has a pronounced effect on NAP-

---

[i] Adapted with permission from Dahlke, K. and C.E. Sing. 2017. Facilitated Dissociation Kinetics of Dimeric Nucleoid-Associated Proteins Follow a Universal Curve. *Biophys. J.* 112:543-551.

DNA dissociation kinetics. Recent single-molecule measurements, using force spectroscopy and fluorescence microscopy, have determined the unbinding kinetics of a variety of NAPs, including FIS and HU in the presence of other NAPs in solution [99, 100]. These molecules are thought to facilitate the dissociation of the proteins bound to the DNA by competing for binding locations. Initial studies with competing NAPs in solution unexpectedly found a linear concentration-dependent unbinding rate [99]:

$$k_{\text{off}} = k_0 + k_1 c \tag{2.1}$$

Here, k_0 is the unbinding rate constant in the limit of zero concentration and k_1 is the unbinding coefficient that incorporates the linear protein concentration c dependence of the unbinding rate constant.

Further studies incorporated an external DNA concentration instead of an external protein concentration [100]. These studies showed a different concentration-dependent unbinding rate,

$$k_{\text{off}} = \frac{c}{Ac + B} \tag{2.2}$$

where A and B are constants that can be fit experimentally, and c is the freely-diffusing DNA concentration. The off-rate increases and then plateaus, indicating that the addition of any more competitor (DNA) will not further facilitate the dissociation of the bound NAPs.

Facilitated dissociation mechanisms, both general and system-specific, have been proposed to describe these different behaviors [100, 106, 142–148]. Some mechanisms predict a purely linear relationship between the competitor concentration and k_{off} [106], while others predict that k_{off} will plateau at high competitor concentrations [100, 142, 147]. Mechanisms that describe the plateau behavior include two limiting behaviors: an initial linearly-dependent increase in the off-rate, then leveling of to a concentration-independent (or pseudo-saturated) off rate [100]. Recent work from Giuntoli *et al.* provides a hypothesized model for dimeric NAP dissociation facilitated by DNA strands in solution [100]. Their model is capable of capturing the general trends seen experimentally, but has not been directly related to the binding and unbinding energy landscape.

The NAP FIS has been shown to demonstrate both linear and plateau behavior depending on the nature of the competitor. Motivated by the FIS-DNA system, the intent of this work is to build upon previous protein-DNA binding and unbinding models to capture both the linear and plateau unbinding rates of FIS from DNA [99, 100, 106]. Our simulations show that both experimentally-observed trends arise from the same general model, and are part of a larger continuum between facilitated, non-facilitated, and maximally-facilitated dissociation behaviors. We expect that our work has broader implications than just the FIS-DNA system that may be extended to NAP-DNA or other biomolecular systems that undergo facilitated dissociation [40, 149–151].

2.2 Materials and Methods

In order to investigate the binding and unbinding kinetics of dimeric NAPs from DNA, we use a coarse-grained Brownian Dynamics (BD) model that incorporates NAP dimeric structure and a proposed binding energy landscape. The simulations are designed such that they mimic the single-molecule experiments performed by Graham *et al.*[99] and Giuntoli *et al.*[100], and also build on previously proposed models of the system [106]. We initialize our system with a static linear chain of N beads of radius $a = 2.0$ nm to represent the tethered DNA strand. FIS proteins are modeled as n_D dimers of beads, and freely diffusing DNA strands are modeled as n_s chains of M beads. The simulation box size is $200a \times 200a \times 224a$ with periodic boundary conditions. Simulation snapshots are shown in Fig. 2.1A.

The movement of individual beads of index i is governed by the Langevin equation:

$$\frac{\partial \mathbf{r}_i}{\partial t} = -\sum_{j}^{N_{total}} \mu_{\mathbf{ij}} \cdot \nabla_j U(t) + \xi_i \tag{2.3}$$

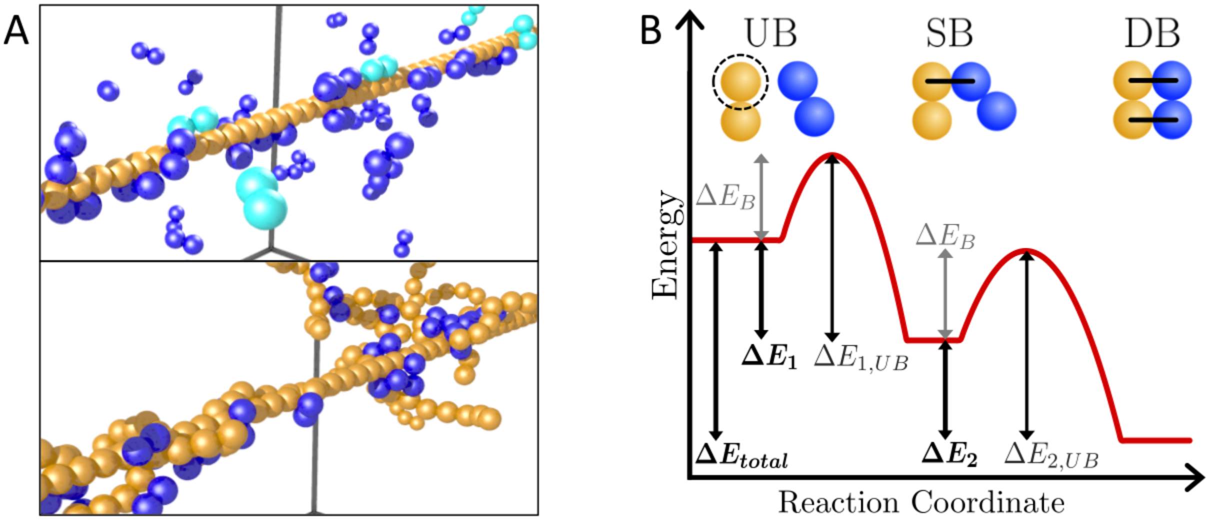

Figure 2.1: **A.** Snapshots from the simulations. "Tagged" proteins are colored light blue, untagged or non-tagged proteins are dark blue, and DNA is yellow. **B.** Energy landscape of the system, demonstrating relevant variables. Three states are present: unbound (left), singly-bound, and doubly-bound (right). $\Delta\tilde{E}_1$ is the energy difference between unbound and singly bound, and $\Delta\tilde{E}_2$ is the energy difference between singly bound and doubly bound. $\Delta\tilde{E}_{total} = \Delta\tilde{E}_1 + \Delta\tilde{E}_2$, and $\Delta\tilde{E}_i = \Delta\tilde{E}_{i,UB} - \Delta\tilde{E}_B$.

where each particle i has a radius of a and position $\mathbf{r_i}$. $\mu_{\mathbf{ij}} = \delta_{ij}\delta/(6\pi\eta a)$ is the freely-draining Stokes mobility matrix, η is the solvent viscosity, δ is the identity matrix, ξ_i is a random velocity that satisfies $\langle\xi_i\xi_j\rangle = 2k_BT\mu_{\mathbf{ij}}\delta_{ij}$, and δ_{ij} is the Kronecker delta. The energy of the system is normalized by k_BT ($\tilde{U} = U/k_BT$), distances are normalized by a ($\tilde{r}_{ij} = r_{ij}/a$), and time is normalized by the diffusion time of a single bead $\tau_D = 6\pi\eta a^3/(k_BT)$. A tilde indicates that a value is normalized and dimensionless.

The potential energy of the system, U, is the sum of three contributions, $U = U_S + U_{LJ} + U_B$, representing connectivity, excluded volume, and bending, respectively. U_S is a harmonic spring potential:

$$\tilde{U}_S = \frac{\tilde{\kappa}_s}{2}\sum_{ij}(\tilde{r}_{ij} - \tilde{r}_0)^2 \tag{2.4}$$

where $\tilde{r}_{ij}$ is the distance between the two beads i and j, and the spring constant is set to $\tilde{\kappa_s} = 200.0$ to prevent large deviations from the equilibrium bond length, $\tilde{r}_0 = 2.0$. Beads in the protein dimers are connected via this harmonic potential, as are the DNA beads in the freely-diffusing strands.

The repulsive part of a Lennard-Jones (LJ) potential, U_{LJ} accounts for excluded volume interactions between beads:

$$\begin{cases} \tilde{U}_{LJ} = \tilde{\epsilon} \sum\limits_{ij} \left[\left(\frac{\tilde{r}_0}{\tilde{r}_{ij}} \right)^{12} - 2 \left(\frac{\tilde{r}_0}{\tilde{r}_{ij}} \right)^{6} + 1 \right] & \tilde{r}_{ij} \leq 2.0 \\ 0 & \tilde{r}_{ij} > 2.0 \end{cases} \tag{2.5}$$

where the LJ parameter $\tilde{\epsilon} = 0.41$ sets the magnitude of the excluded volume potential.

The bending potential, U_B, is included for freely-diffusing DNA strands:

$$\tilde{U}_B = \frac{\tilde{\kappa}_\theta}{2} \sum_{i=1}^{m-1} (\theta_i - \theta_0)^2 \tag{2.6}$$

where θ_i is the angle between the bonds of beads $i-1$ and i, and i and $i+1$. θ_0 is the equilibrium angle between the bonds of beads $i-1$ and i, and i and $i+1$ and is set to $\theta_0 = 0.0$. The bending force constant is set at $\tilde{\kappa}_\theta = 12.5$, which is chosen to match the dsDNA persistence length of 50 nm.

The binding energy landscape of the system is controlled by the binding and unbinding barriers, shown in Fig. 2.1B. Each bead in the protein dimer can independently bind (and unbind) to DNA, and the protein can therefore be in one of three states, shown in Fig. 2.1B. The dimer can be completely unbound from the DNA (UB), bound by a single bead to the DNA (SB), or bound by both beads in the dimer to the DNA (DB). Each DNA bead can only bind to a single protein bead, so doubly bound proteins occupy two adjacent DNA beads. The binding and unbinding steps occur via a Monte Carlo update step occurring every $\tilde{\tau}_0 = 0.05$, which demonstrates the statistical results expected from a Bell Model type reaction [152]. The connectivity of a protein bead (i) and DNA bead (j) is modeled as a harmonic potential that is recalculated every $\tilde{\tau}_0$ as follows:

$$\tilde{U}_C = \frac{\tilde{\kappa}_s}{2} \sum_{ij} \omega_{ij}(\tilde{r}_{ij} - \tilde{r}_0)^2 \tag{2.7}$$

$$\omega_{ij}(t) = \begin{cases} \begin{cases} 1 \text{ if } \Xi < e^{-\Delta E_B} \\ 0 \text{ if } \Xi > e^{-\Delta E_B} \end{cases} & \text{if } \sum_k (\omega_{kj}(\tilde{t} - \tilde{\tau}_0) + \omega_{ik}(\tilde{t} - \tilde{\tau}_0)) = 0 \text{ \& } \tilde{r}_{ij} < 2.1 \\ \begin{cases} 1 \text{ if } \Xi < e^{-\Delta E_{\mathrm{UB},2}} \\ 0 \text{ if } \Xi > e^{-\Delta E_{\mathrm{UB},2}} \end{cases} & \text{if } \omega_{ij}(\tilde{t} - \tilde{\tau}_0) = 1 \text{ \& DB} \\ \begin{cases} 1 \text{ if } \Xi < e^{-\Delta E_{\mathrm{UB},1}} \\ 0 \text{ if } \Xi > e^{-\Delta E_{\mathrm{UB},1}} \end{cases} & \text{if } \omega_{ij}(\tilde{t} - \tilde{\tau}_0) = 1 \text{ \& SB} \end{cases} \tag{2.8}$$

where Ξ is a random number between 0 and 1 generated for each i. The reaction radius $\tilde{r}_{ij} < 2.1$ is informed by previous work which demonstrates that this choice leads to the appropriate binding thermodynamics and kinetics [153]. Updates to $\omega_{ij}(t)$ are performed randomly to avoid biasing the binding behavior based on chain index.

Inspired by the nearly symmetric geometry of a bound FIS-DNA complex [154], previous literature considers identical energy barriers of binding for each bead in the dimer, regardless of the protein's state ($\Delta\tilde{E}_1 = \Delta\tilde{E}_2$) [106]. This allowed for only one degree of freedom in the binding landscape, $\Delta\tilde{E}_{total}$. In the current model, each of the beads in the dimer can unbind with different energy barriers, allowing for an extra degree of freedom ($\Delta\tilde{E}_1$ and $\Delta\tilde{E}_2$) and therefore a wider set of possible solutions. Recent work by Tsai *et al.* supports this three state model and non-symmetric energies [85]. $\Delta\tilde{E}_B = 3.0$ is kept constant to ensure that the binding time, τ_B, is equal to the diffusive time of the bead, $\tau_D = \tau_B = 1/\nu_0 e^{\Delta\tilde{E}_B} = 6\pi\eta a^3/(k_B T)$, where $\nu_0 = 1/\tau_0$ is the Monte Carlo update frequency.

Simulations measuring unbinding kinetics are initialized with 25 dimers that are doubly bound to the stationary DNA chain. These dimers are 'tagged', while competitors (other dimers or freely moving DNA chains) are initialized randomly throughout the box to obtain the desired concentration, c. When a tagged dimer diffuses a distance $6a$ from the tethered DNA strand, it becomes untagged and is removed from the system. This allows for rapid rebinding to occur, but does not increase the amount of free protein that can act as a competitor in the system. The number of tagged molecules, n_B, is tracked over time.

2.3 Results and Discussion

2.3.1 Equilibrium Behavior

Facilitated dissociation dynamics are reflected in the equilibrium behavior of FIS-DNA binding, which is readily accessible in experiment via standard titration assays [155]. We demonstrate this by simulation and analytical calculations of the average amount of FIS bound to DNA for a given set of energies ($\Delta\tilde{E}_1$ and $\Delta\tilde{E}_2$). Comparison of the analytical value to the simulated equilibrium behavior also verifies that the simulation reflects the intended energy landscape. The simulations are initiated with a static DNA strand of $N = 50$ beads and dimers randomly placed throughout the box to obtain the desired concentration c. We define dimer concentrations as the number of dimer molecules, n_D per volume. After the system reaches equilibrium, the number of filled binding sites n_p is averaged over $> 1.0 \times 10^8$ time steps, which is substantially longer than the relaxation time of the system. We track the number of filled binding sites, n_p, as a function of $\Delta\tilde{E}_2$ and $\Delta\tilde{E}_{total}$ for various dimer concentrations c. $\Delta\tilde{E}_{total} = 13.0$ is shown in Fig. 2.2A, and a similar plot for $\Delta\tilde{E}_{total} = 10.0$ can be seen in Fig. 2.2B. Symmetric energies ($\Delta\tilde{E}_1 = \Delta\tilde{E}_2$) follow the same trends as observed in Sing, et al [106].

The effect of non-symmetric energies is evident in this equilibrium data. At at high $\Delta\tilde{E}_2$ (and low $\Delta\tilde{E}_1$), proteins have a very low probability of moving from the doubly bound state to the singly bound state. Dimers spend most of their time bound to the DNA in the doubly bound state, taking up two binding sites along the DNA strand. The consequence is fewer proteins binding to the DNA, and the DNA being nearly saturated with doubly bound proteins at high enough concentrations. Alternatively, very low $\Delta\tilde{E}_2$ (and high $\Delta\tilde{E}_1$ in relation),

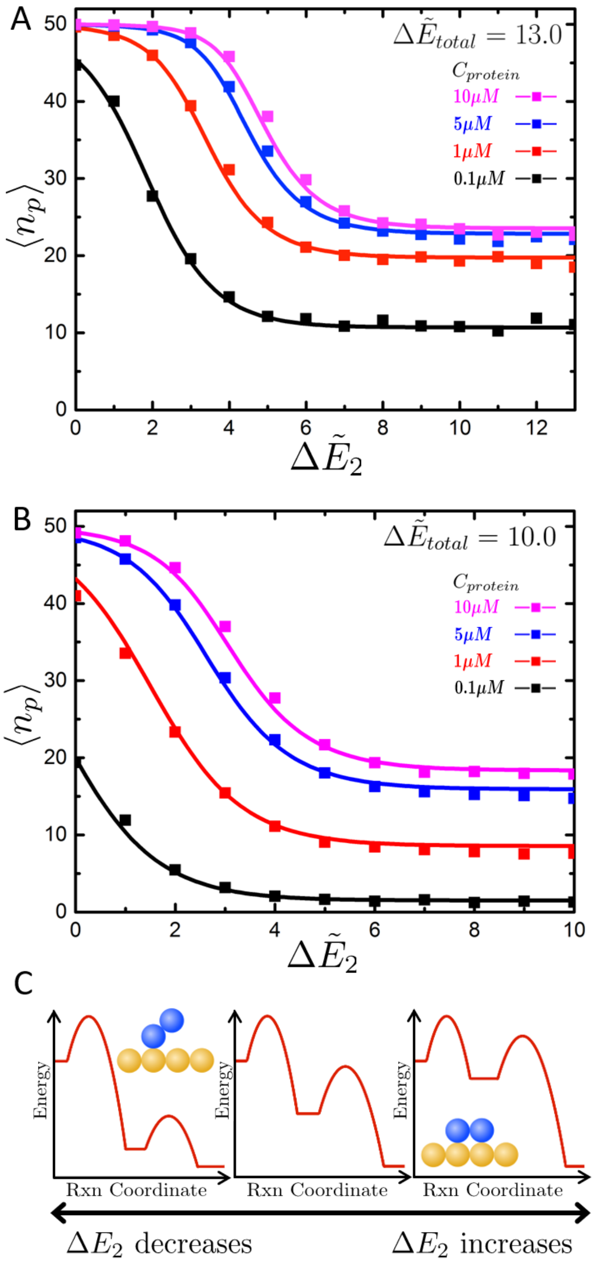

Figure 2.2: **A-B:** Number of bound proteins n_p as a function of $\Delta\tilde{E}_2$ for a total energy of $\Delta\tilde{E}_{total} = 13.0$ (**A**) and $\Delta\tilde{E}_{total} = 10.0$ (**B**). The solid lines indicate the analytical value, and the data points are obtained from simulations. **C.** Energy diagrams depicting the three extreme states: left, $\Delta\tilde{E}_2$ is low and proteins prefer to be in the singly bound state over the doubly bound state; center, $\Delta\tilde{E}_2 = \Delta\tilde{E}_1$; right, $\Delta\tilde{E}_2$ is high and proteins prefer to be in the doubly bound state over the singly bound state.

the proteins have a very high probability of moving between the doubly bound state and the singly bound state (see Fig. 2.2C). While proteins can be found in the doubly bound state, the time spent in that state is much less than the time spent in the singly bound state. This allows more open binding sites along the DNA strand, and at high enough concentrations, the DNA is saturated with singly bound proteins. This over-bound state has been experimentally observed for a number of DNA-binding proteins [39, 108], which creates a much "stiffer" DNA strand.

The equilibrium adsorption behavior can be described with an analytical expression, derived using a transfer matrix calculation of the partition function. This method is well-established in statistical mechanics, and is used by Sing *et al.* to derive their adsorbtion equation for a similar system [106]. The grand partition function of the multi-energy system ($\Delta E_1 \neq \Delta E_2$) in vector notation is shown below:

$$\Xi = \sum_{\vec{n}_B} e^{\beta\left[\vec{n}_{B1}\cdot\left(\Delta\vec{E}_1+\vec{\mu}\right)+\vec{n}_{B2}\cdot\left(\Delta\vec{E}_2-2.0\right)\right]} \tag{2.9}$$

where $\vec{n}_B$ represents the "occupancy" of the system: each i can be in one of three states (unbound, partially bound, or fully bound). $n_{B1} = 0$ indicates that i is *not* in the partially (singly) bound state, and $n_{B1} = 1$ indicates that i *is* in the partially bound state. This occupancy definition is the same for n_{B2} and the fully (doubly) bound state. $\Delta\vec{E}_1$ is the energy upon binding for a partially bound protein, and $\Delta\vec{E}_2$ is the energy upon binding for a fully bound protein. μ is the chemical potential, and the 2.0 is a simulation-dependent protein degree of freedom term.

The grand partition function can be calculated by multiplication of matrices instead of by direct summation. These matrices, $\mathbf{M}_{i,j}$ represent probabilities of a state at i based on the possibilities of what the state was at $i-1$. Because there are three possible states, a 3×3

matrix is required:

$$\mathbf{M}_{i,j} = \begin{bmatrix} 1 & 1 & 1 \\ P & P & P \\ 0 & Q & 0 \end{bmatrix} \tag{2.10}$$

where $P = e^{\Delta\tilde{E}_1+\tilde{\mu}}$ and $Q = e^{\Delta\tilde{E}_2-2.0}$. $\tilde{\mu}$ is the ideal gas chemical potential, $\tilde{\mu} = \tilde{\mu}_0 + \ln(c)$, where $\tilde{\mu}_0 = 5.7$ is the constant reference chemical potential obtained from fits to the simulation data. Each term of the matrix is the contribution at position i given the contribution at position j to the partition function. The first row holds the contributions of moving from any state (unbound, corresponding to the first column, partially bound, corresponding to the second column, or fully bound, corresponding to the third column) to the unbound state. The second row are the contributions (P) moving from any state (unbound, partially bound, or fully bound) to the partially bound position. The third row are the contributions (Q) moving from any state to the fully bound state. Movement from unbound to fully bound or fully bound to fully bound is not possible, so those contribution terms are always 0.

The matrix multiplication form of the grand partition function is

$$\Xi = \vec{\phi}_N \mathbf{M}_{i,j}^{N-2} \vec{\phi}_0 \tag{2.11}$$

where $\vec{\phi}_N = \vec{\phi}_0 = 1P$ are the contributions of the ends of the chain of length N to the partition function. With a large enough value of N, this equation can be approximated by the largest eigenvalue of $\mathbf{M}_{i,j}$, λ_0, to the Nth power:

$$\Xi \approx \lambda_0^N \tag{2.12}$$

We note that the matching between simulation and theory provides *a posteriori* justification for the large-N assumption. For this multi-energy, multi-state system, the largest eigenvalue is

$$\lambda_0 = \frac{1}{2}\left[1 + P + \sqrt{(1+P)^2 + 4PQ}\right] \tag{2.13}$$

where P and Q are the partition function contributions shown earlier.

To find the equilibrium number of proteins, we use the thermodynamic relationship

$$k_B T \ln[\Xi] = G - \mu n_p \tag{2.14}$$

where n_p is the number of proteins bound to the DNA (either partially or fully bound). When we substitute λ_0 in for Ξ, we can solve for $\langle n_p \rangle$:

$$\langle n_p \rangle = \frac{k_B T N}{\lambda_0}\frac{\partial \lambda_0}{\partial \mu} = NP\left[\frac{1 + \frac{2Q+1+P}{\sqrt{(1+P)^2+4QP}}}{1 + P + \sqrt{(1+P)^2 + 4QP}}\right] \tag{2.15}$$

which is a more general version of the expression found in Sing *et al.* for symmetric binding energies. This analytical result is plotted as lines in Fig. 2.2A and B, and demonstrates matching with simulation for both symmetric and asymmetric binding energies.

2.3.2 Unbinding Model

While the model proposed by Sing *et al.* successfully described the linear concentration-dependent behavior of competing proteins in solution [106], later experimental work showed different behavior when the identity of the competitor was changed [100]. Giuntoli *et al.* proposed a dissociation mechanism based on DNA competitors, shown by states 0-3 in Fig. 2.3.

A mean reaction time model was used to calculate the average time it takes for a protein starting in state 0 (doubly bound) to be removed from the tethered DNA strand (state 3) [156]:

$$\langle \tau_{03} \rangle = \frac{k_{01}(k_{12} + k_{21} + k_{23}) + k_{10}(k_{21} + k_{23}) + k_{21}k_{23}}{k_{01}k_{12}k_{23}} \tag{2.16}$$

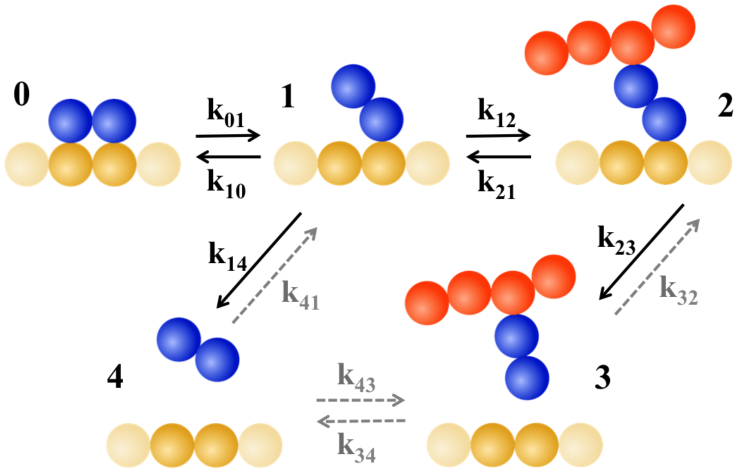

Figure 2.3: Proposed unbinding mechanism. The blue dimers are proteins, the light orange strand represents the tethered DNA strand, and the dark orange strands represent the DNA competitors. The k_{ij}'s are the rate constants for moving from state i to state j. Because very little dissociation is seen without competitor in solution, there is an assumption that movement to and from state 4 is negligible, leading to states 0-3 being used to derive Eq. 2.16.

where k_{ij} are the rates moving from state i to state j and $k_{\mathrm{off}} = {\tau_{03}}^{-1}$. The concentration dependence is built into k_{12}, where the rate is multiplied by the concentration of competing DNA molecules, c. A simplified version of Eq. 2.16 was used to describe the unbinding kinetics observed experimentally:

$$k_{\mathrm{off}} = c/(Ac + B) \tag{2.17}$$

where A and B are functions of the rates moving from state i to state j, k_{ij}, and c is the concentration of competing DNA molecules.

This result from Giuntoli *et al.* can be fit to the observed facilitated dissociation kinetics k_{off}; however, the relationship to the underlying energy landscape was not explored. We connect the rate constants k_{ij} to energetic and structural parameters, providing a connection between experimental observations of facilitated dissociation and molecular details of FIS-DNA interactions.

We determine the transition rates k_{ij} using the values from the energy landscape in Fig.

2.1B, along with system specific values, such as the binding and unbinding testing frequency, ν_0. The rate constant k_{01} is dependent only on the unbinding energy of a doubly bound protein ($\Delta\tilde{E}_{UB,2}$) and ν_0. Because both of the beads in the dimer can unbind with the same probability, there is a factor of two in the rate constant, leading to $k_{01} = 2\nu_0 e^{-\Delta\tilde{E}_{UB,2}}$. Rate constants k_{21} and k_{23} are similarly calculated using $\Delta\tilde{E}_{UB,1}$, leading to $k_{21} = k_{23} = 2\nu_0 e^{-\Delta\tilde{E}_{UB,1}}$.

k_{10} represents the transition from state 1 to state 0 (singly to doubly bound). This transition rate depends not only on the binding energy, $\Delta\tilde{E}_B$, but is also dependent on the number of available DNA binding positions open within 2.1a. This leads to k_{10} as a function of the expected $\Delta\tilde{E}_B$ and ν_0, but indirectly as a function of $\Delta\tilde{E}_{UB,2}$, since this simulation value impacts how many DNA binding positions are available. A prefactor value in k_{10}, α, takes into account this contribution, leading to $k_{10} = \alpha\nu_0 e^{-\Delta\tilde{E}_B}$. This prefactor decreases with increasing $\Delta\tilde{E}_{UB,2}$, because as $\Delta\tilde{E}_{UB,2}$ increases, proteins are predominantly found in the doubly bound position, leaving fewer open DNA binding sites. This results in a lower probability that a singly bound protein can bind to the DNA, leading to a smaller k_{10} value.

The rate constant k_{12} appears in the concentration-dependent term of k_{off}: $k_{12}c$. We introduce a prefactor β to the rate constant k_{12} to account for the correlation of competitor binding opportunities. When there is no competitor within binding range at t, it may be more likely than average that there remains no competitor at $t+\tau_0$. This is a correlation effect that becomes significant at low $\Delta\tilde{E}_2$, where the singly and doubly bound states interchange rapidly. This leads to the expression $k_{12} = \beta\nu_0 e^{\Delta\tilde{E}_B}$. The different competitor geometries and methods of competition lead to different binding correlations at different $\Delta\tilde{E}_2$.

Using the predicted k_{ij} values, the full mean reaction rate equation can be simplified to the following:

$$k_{\text{off}} = \gamma \frac{\beta c}{\dfrac{\beta c}{2e^{-\Delta\tilde{E}_{1,UB}}} + \dfrac{2e^{-\Delta\tilde{E}_{2,UB}} + \alpha e^{-\Delta\tilde{E}_B} + e^{-\Delta\tilde{E}_{1,UB}}}{e^{-\Delta\tilde{E}_{2,UB}-\Delta\tilde{E}_B}}} \tag{2.18}$$

where γ is the simulation-dependent constant that takes into account the testing frequency, and α and β are the aforementioned prefactors.

2.3.3 Facilitated Dissociation Simulations

We test a variety of simulation conditions for DNA competitors to verify the hypothesized model: we consider different $\Delta\tilde{E}_{total}$, $\Delta\tilde{E}_2$, and DNA competitor concentrations, defined by the number of DNA beads ($M \cdot n_s$) per volume. For each specified set of values, the number of tagged proteins in the system is tracked over time for 30 individual trajectories. In Fig. 2.4A we plot the averaged number of bound proteins $\langle n_B \rangle$ for different values of $\Delta\tilde{E}_2$ at constant $\Delta\tilde{E}_{total} = 13.0$ and constant $c = 20.0\text{ng}/\mu\text{L}$. This set of curves is an example of those seen at other values of $\Delta\tilde{E}_{total}$ and c; data for different $\Delta\tilde{E}_{total}$ (and symmetric energies, $\Delta\tilde{E}_1 = \Delta\tilde{E}_2$) can be seen in seen in Fig. 2.4B. An unbinding rate constant k_{off} can be calculated from unbinding curves, like those shown in Fig. 2.4A and B, via a fit to the following expression:[ii]

$$\langle n_B \rangle = n_{B,0} e^{-k_{\text{off}} \tilde{t}} \tag{2.19}$$

Rate constants k_{off} corresponding to a constant $\Delta\tilde{E}_{total} = 13.0$ are plotted in Fig. 2.4C as a function of concentration c and $\Delta\tilde{E}_2$. A similar plot for k_{off} as a function of $\Delta\tilde{E}_{total}$ and c is shown in Fig. 2.4D.

The facilitated dissociation simulations were repeated with proteins as the competitor in solution, using the same method to calculate the unbinding constants k_{off}. Very similar behavior (both qualitative- and quantitatively) is observed and can be seen in Fig. 2.5A-D.

We can directly track the average time it takes to move from state i to state j and average it over all simulation times and trajectories to verify the theoretical k_{ij} values. From

---

[ii] We account for the differences between the theoretical and simulated k_{off} values by adding a k_0 to the theoretical k_{off}. The theory-based equation only accounts for the concentration dependent dissociation pathway, and the addition of k_0 accounts for non-concentration dependent dissociation that is seen in our simulations (but not experimentally). Modified simulations that prevent unfacilitated dissociation show matching between the unmodified theory and simulated k_{off} values.

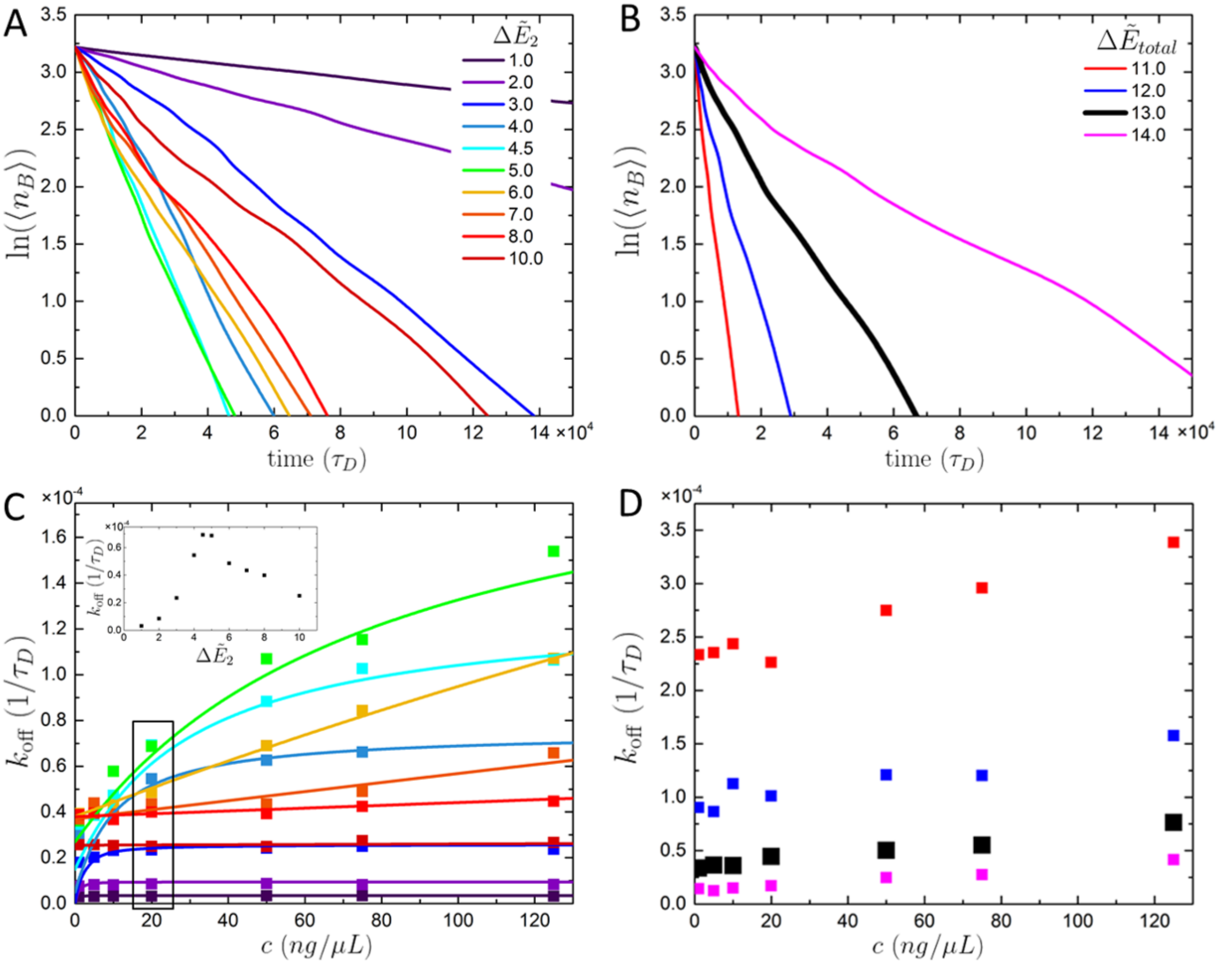

Figure 2.4: Data from DNA facilitated dissociation simulations. **A-B:** Unbinding curves for external $c = 20 ng/\mu L$. The system starts with 25 tagged proteins doubly bound to the stationary DNA strand, and DNA strands are initialized throughout the simulation box to obtain a concentration of $c = 20 ng/\mu L$. This corresponds to 120 competitor DNA beads. When a tagged protein moves $6a$ from the tethered DNA, the protein is removed, and we observe that the number of tagged proteins (n_B) in the system decreases exponentially. Panel **A** shows data for different $\Delta\tilde{E}_2$ at a constant $\Delta\tilde{E}_{total} = 13.0$, and panel **B** shows data for different $\Delta\tilde{E}_{total}$ with symmetric energies (bolded black lines correspond to $\Delta\tilde{E}_{total} = 13.0$). **C-D:** The off-rate constant, k_{off} as a function of c at different $\Delta\tilde{E}_2$ (**C**) and $\Delta\tilde{E}_{total}$ (**D**). The solid lines in **C** are values calculated from Eq. 2.16. An example of the k_{off} for $c = 20 ng/\mu L$ at $\Delta\tilde{E}_{total} = 13$ is shown in the inset to panel **C**.

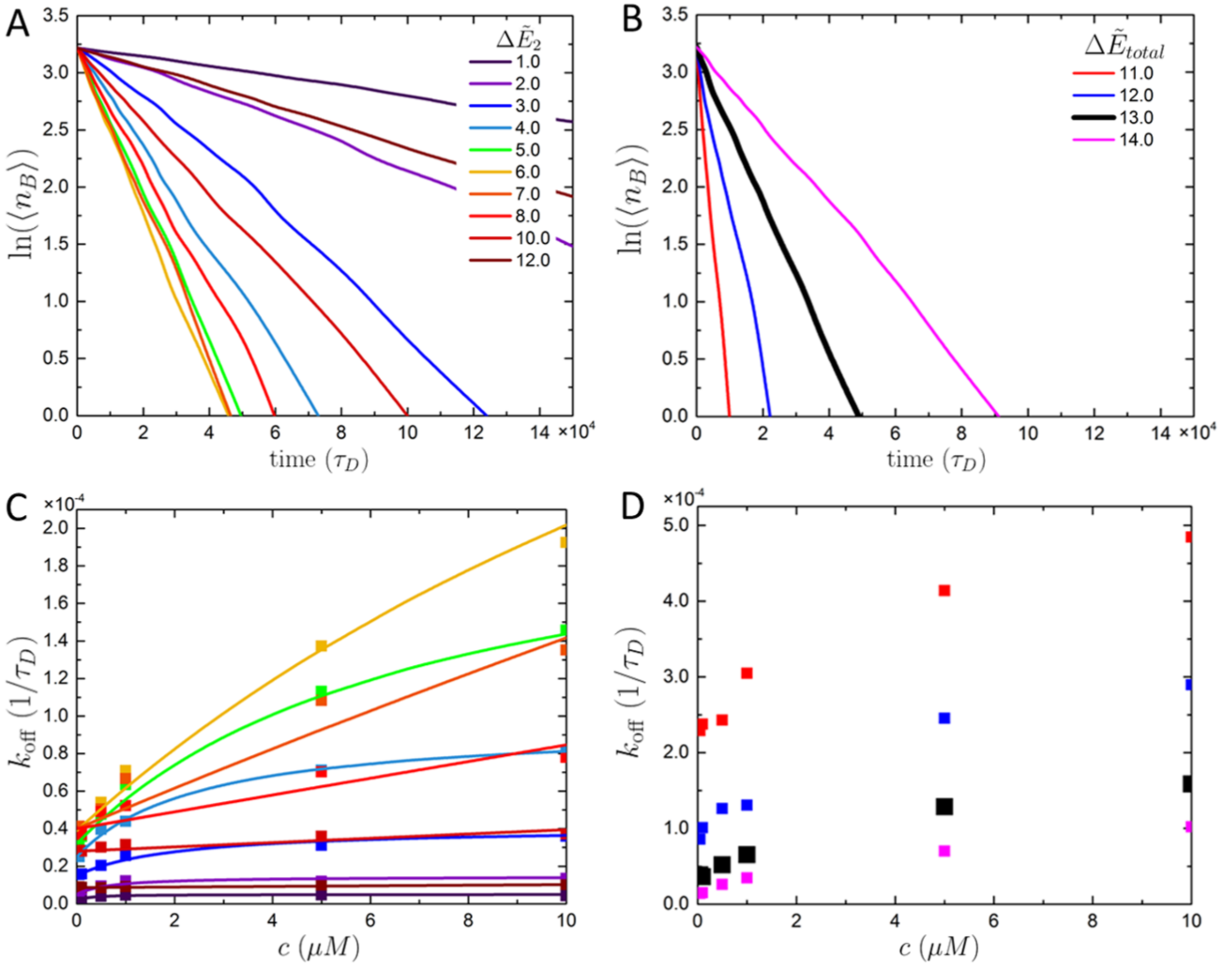

Figure 2.5: Data from protein facilitated dissociation simulations. **A-B:** Unbinding curves for external $c = 1/$. The system starts with 25 tagged proteins doubly bound to the stationary DNA strand, and protein dimers are initialized throughout the simulation box to obtain a concentration of $c = 1$. This corresponds to 86 protein beads, or 43 protein dimers. When a tagged protein moves $6a$ from the tethered DNA, the protein is removed, and we observe that the number of tagged proteins (n_B) in the system decreases exponentially. Panel **A** shows data for different $\Delta\tilde{E}_2$ at a constant $\Delta\tilde{E}_{total} = 13.0$, and panel **B** shows data for different $\Delta\tilde{E}_{total}$ with symmetric energies. **C-D:** The off-rate constant, k_{off} as a function of c at different $\Delta\tilde{E}_2$ (**C**) and $\Delta\tilde{E}_{total}$ (**D**). The solid lines are values calculated from Eq. 2.16.

these simulations, we are able to calculate the values of the prefactor α directly from the measurement of k_{10}, which range from 0.15 to 0.06 with increasing $\Delta\tilde{E}_2$. The values of β are determined from the overall k_{off} behavior by fitting Eq. 2.18 to data, and are dependent on competitor identity. For DNA competitors, β ranges from 0.001 to 0.000045 with increasing $\Delta\tilde{E}_2$, and for protein competitors, β values range from 0.00013 to 0.04 as $\Delta\tilde{E}_2$ increases. Both of these prefactors are independent of concentration.

When considering the unbinding constants for symmetric energies ($\Delta\tilde{E}_1 = \Delta\tilde{E}_2$) at low concentrations of either competitor, we observe the linear behavior described by previous experiments and simulations [99, 106]. However, if we go to higher concentrations or non symmetric energies, we see that the both competitors can display the plateau off-rate seen experimentally with DNA competitors.

When at a single concentration and total energy (as in Fig. 2.4A), the dissociation rate (k_{off}) shows non-monotonic behavior. It initially increases as $\Delta\tilde{E}_2$ increases; however, after k_{off} reaches its maximum value at a "turnaround" $\Delta\tilde{E}_2$, it begins to decrease. This non-monotonic behavior can be explained with the asymmetric unbinding energy effect included in our simulations. At low $\Delta\tilde{E}_2$ (high $\Delta\tilde{E}_1$), proteins are preferentially in the singly-bound rather than the doubly-bound state. The high energy barrier associated with $\Delta\tilde{E}_1$ must be overcome when moving from the singly-bound to unbound state, leading to long unbinding times. Alternatively, at high $\Delta\tilde{E}_2$, the proteins are strongly bound in the doubly-bound position. They must overcome the high $\Delta\tilde{E}_2$ barrier to become singly bound, but once they do they only need to overcome the small $\Delta\tilde{E}_1$ barrier to fully unbind. Both of these limits result in long unbinding times because the large energy barriers $\Delta\tilde{E}_1$ or $\Delta\tilde{E}_2$ become the bottlenecks of the dissociation mechanism.

At these two extremes, the competitors in solution do not play as much of a role in moving the tagged protein from doubly-bound to singly-bound to unbound. At mid-range $\Delta\tilde{E}_2$, however, the competitors play a large role in preventing the tagged protein from moving from the singly-bound state to the doubly-bound state. The existence of an intermediate

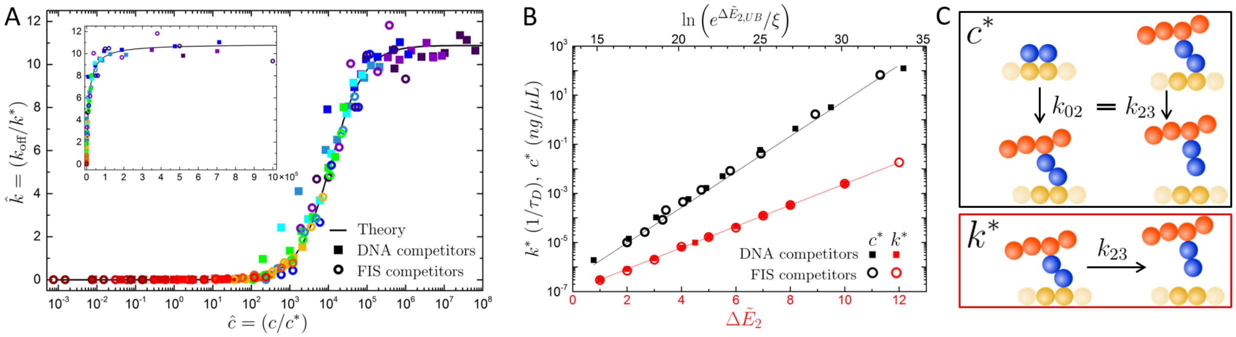

Figure 2.6: **A.** Universal curve for both DNA and protein competitors for $\Delta\tilde{E}_{total} = 13.0$. Each data point is normalized by k^* and c^*, and the solid line is an arbitrary theroy curve calculated from Eq. 2.16. **B.** The c^* and k^* values used to normalize the data points in (**A**) plotted as a function of $\Delta\tilde{E}_2$ on the lower x-axis (for k^*) and $\ln(\Delta\tilde{E}_{2,UB}/\xi)$ on the upper x-axis (for c^*), where $\xi = (e^{-\Delta\tilde{E}_{2,UB}-\Delta\tilde{E}_B})/(2e^{-\Delta\tilde{E}_{2,UB}} + \alpha e^{-\Delta\tilde{E}_B} + e^{-\Delta\tilde{E}_{1,UB}})$. **C.** Conceptual schematic describing the normalizing factors. c^* is the concentration at which the rate from state 0 to state 2 is equal to the rate from state 2 to state 3. k^* is the final step of dissociation, moving from state 2 to state 3.

position is vital for facilitated dissociation, and there is no long-lived intermediate state at the two extremes of $\Delta\tilde{E}_2$. The fastest dissociation occurs when the competitors play the strongest role in the overall unbinding, which is where the "turnaround" point occurs at a mid-range $\Delta\tilde{E}_2$ (dependent on competitor identity and $\Delta\tilde{E}_{total}$).

2.3.4 Rescaling of Facilitated Dissociation Kinetics

All unbinding rate $k_{\rm off}$ versus concentration c curves share similar features, such as an initial linear increase and for some conditions, an eventual plateau value (seen in the inset of Fig. 2.6A). Indeed, we find that for both competitors and for all values of $\Delta\tilde{E}_2$, we can normalize $k_{\rm off} \to k_{\rm off}/k^*$ and $c \to c/c^*$ such that they fall along a single, universal curve independent of the energy landscape parameters or competitor identity (Fig. 2.6A). This is also true of the theoretical fits, indicated by the solid line in in Fig. 2.6A. The two normalization constants, k^* and c^* exhibit regular trends as a function of system parameters (Fig. 2.6B).

The normalization constants k^* and c^* can be understood in the context of Eq. 2.18 and two physical limiting cases. The saturated $k_{\rm off}$ value occurs at high concentration, where the limiting step in the overall off rate is the final dissociation of the tagged protein from the

DNA strand. This can be seen mathematically with Eq. 2.18: when c is very large, Eq. 2.18 can be approximated by

$$k_{\text{off}} \approx \gamma \frac{\beta c}{\frac{\beta c}{2e^{-\Delta \tilde{E}_{1,UB}}}} \propto e^{-\Delta \tilde{E}_1} \propto e^{\Delta \tilde{E}_2} \tag{2.20}$$

This relationship can be seen for both DNA and protein competitors by the red data points in Fig. 2.6B. When the overall k_{off} is normalized by $k^* \sim e^{\Delta \tilde{E}_2}$, all unbinding curves approach the same maximum off-rate.

The transition point from linearly increasing to plateau occurs at a critical concentration, c^*, when the rate going from state 0 to 2 (low concentration regime) is equivalent to the rate going from state 2 to 3 (high concentration regime), $k_{02} = k_{23}$, shown in Fig. 2.6C. As stated above, the high concentration limit is $k_{23} \sim e^{\Delta \tilde{E}_2}$. The rate from state 0 to 2 can be approximated by the low concentration limit of Eq. 2.18:

$$k_{\text{off}} \approx \gamma \frac{\beta c e^{-\Delta \tilde{E}_{2,UB} - \Delta \tilde{E}_B}}{2e^{-\Delta \tilde{E}_{2,UB}} + \alpha e^{-\Delta \tilde{E}_B} + e^{-\Delta \tilde{E}_{1,UB}}} \tag{2.21}$$

When the low concentration limit and high concentration limit of Eq. 2.18 are equal, we see

$$c^* \propto \frac{e^{\Delta \tilde{E}_2}}{\frac{\beta e^{-\Delta \tilde{E}_{2,UB} - \Delta \tilde{E}_B}}{2e^{-\Delta \tilde{E}_{2,UB}} + \alpha e^{-\Delta \tilde{E}_B} + e^{-\Delta \tilde{E}_{1,UB}}}} = \frac{e^{\Delta \tilde{E}_2}}{\xi} \tag{2.22}$$

where ξ is the low concentration limit. This relationship can be seen in the by the black data points in Fig. 2.6B. Normalizing c by c^* moves the transition point to the same universal location for all unbinding curves.

The different $\Delta \tilde{E}_2$ regimes effect the low concentration limit. At low $\Delta \tilde{E}_2$, $2e^{-\Delta \tilde{E}_{2,UB}}$ is the dominant term in the denominator due to the prefactor of 2 (and the α prefactor of the binding term), leading to $\xi \approx \beta e^{-\Delta \tilde{E}_B}/2$. At midrange $\Delta \tilde{E}_2$, the term with $\Delta \tilde{E}_B$ is the dominant term, even with the small α prefactor, leading to $\xi \approx \beta e^{-\Delta \tilde{E}_{2,UB}}$. At very high $\Delta \tilde{E}_2$, the $\Delta \tilde{E}_{1,UB}$ begins to be dominant, leading to $\xi \approx \beta e^{-\Delta \tilde{E}_{2,UB} - \Delta \tilde{E}_B} / e^{\Delta \tilde{E}_{1,UB}}$.

There are some differences between the simulation and experimentally observed off rate behaviors. The energy barriers used in the simulations are much smaller than the real world experimental values to allow us to observe dissociation on computationally accessible time scales. The non-negligible k_{off} at a concentration of 0 observed in the simulations reflects this difference. The model is otherwise not dependent on the size of the energy barriers (on the order of $k_B T$) and resulting time scales ($< 10\ ms$) used in the simulations. It can be extended to far longer times ($>$ 1000 s) seen experimentally [99, 100]. The off-rate plateau observed in our protein-competitor simulations had not been observed in initial work [99, 106], but is consistent with more recent experiments showing saturated dissociation at sufficiently high concentrations [104].

2.4 Conclusion

Solution phase concentration-dependent dissociation has been experimentally observed for NAPs and other DNA binding proteins [99, 100, 104, 147], as well as other biological binding partners, such as DNA duplexes [142]. Different concentration dependencies were observed, and multiple models have been proposed to explain the concentration dependence of different systems [100, 106, 142–146]. The present simulation work confirms the physical behavior suggested by Giuntoli *et al.* as a result of their three-state mean reaction time model.

Our simulations allow us to understand the effect of energetic and physical parameters on the mechanism of facilitated dissociation. Regardless of the competitor identity and parameter values, all dissociation rates can be normalized to the same universal curve, which encompasses all of the different aspects of the concentration-dependent dissociation behaviors observed. At low concentrations for both simulated protein and DNA competitors, we see the linearly-concentration dependent behavior that is experimentally observed with proteins in solution [99]. We also see the plateau behavior seen in DNA-competitor experiments [100], once again for both the simulated proteins and DNA with certain parameter values.

The simulations in this work were designed to mimic single-molecule experiments involving NAPs and DNA, but they can easily be expanded to other systems. By altering the binding energy ΔE_B for individual DNA beads to correspond to favorable or unfavorable binding events, we can, in principle, simulate sequence-specificity of protein binding, which is important for proteins like transcription factors [138, 157]. We note that slight differences in sequence specificity can also quantitatively affect facilitated dissociation, which has previously been considered in previous work by one of the authors [106]. Other changes to the system such as untethering the DNA strand, incorporating effects such as DNA allostery [158], initializing with a DNA strand that is not saturated with proteins, or adding in additional forces, all of which correspond to *in vivo* behaviors, can, in principle, be added. The dissociation model can also be extended to other molecules that have a multi-state binding mechanism, even if molecular features are the cause of the behavior, and not the dimeric binding domains often seen in NAPs [32].

While the model used in this work is more complex than the model proposed by Sing *et al.*, we are able to capture the linearly increasing and eventual plateau of the unbinding rate trends while still retaining a robust, physical understanding of the dissociation behavior. Scaling of the low and high concentration regimes come directly from the off-rate Eq. 2.18 that is composed of system-specific parameters. The shifting of these two different regimes with different $\Delta\tilde{E}_2$ can provide information about experimentally observed facilitated dissociation. Proteins that are strongly bound in the fully bound state (high $\Delta\tilde{E}_2 : \Delta\tilde{E}_1$ ratio) demonstrate seemingly linear behavior, and proteins that are strongly bound in the partically bound state (low $\Delta\tilde{E}_2 : \Delta\tilde{E}_1$ ratio) demonstrate rapid plateau behavior.

Our findings have shown a continuum of facilitated dissociation from concentration-dependent facilitation to saturated facilitation behavior, which has implications for NAP and nucleoid function. NAP concentrations in cells vary with different growth conditions [65], leading to different protein-DNA dissociation rates and consequently different protein-DNA association times. These varying NAP concentrations also compact the DNA differently [68, 100, 102], allowing a higher (or lower) local concentration of DNA to facilitate protein dissociation.

Future experimental and simulation studies with additional NAPs can provide more information about where the dissociation rate behavior of different NAPs falls along the spectrum of facilitated dissociation.

Chapter 3

Force-dependent facilitated dissociation can generate protein-DNA catch bonds[i]

3.1 Introduction

Molecular mechanical forces play an important role in genomic function, governing physiological behaviors including mechanical signaling, gene transcription and expression, and genome structure [159–163]. Reaction-rate theory [152, 164–170] and *in vivo* [161, 171–173] and *in vitro* [174–176] experiments suggest that cells may transduce these mechanical stimuli through alterations to ligand-substrate interactions, such as protein-DNA association and dissociation kinetics. For many biomolecular interactions, dissociation requires escaping a single potential energy well, and forces accelerate unbinding by lowering the energy barrier for the dissociation. However, multivalent proteins, *i.e.*, those with more than a simple binary set of "on" or "off" states, may dissociate from DNA through multiple, distinct kinetic pathways. These additional kinetic pathways are commonly facilitated by DNA binding by competitor biomolecules from solution [99, 105, 150, 177]. Because of such "facilitated dissociation" phenomena, the unbinding kinetics of DNA-binding proteins may be considerably more complicated when DNA is subjected to mechanical forces.

Recent work with a variety of biomolecules, such as transcription factors [99, 100, 104, 105, 178–181], metalloregulators [55, 150], chromatin effectors [182], DNA polymerases [183–187], antibody-antigen complexes [188], and other biological complexes [142, 177, 189–198] has demonstrated that facilitated dissociation, in which protein dissociation rates depend on ambient protein or other biomolecule concentration, is a widespread phenomenon both *in*

---

[i] Submitted to *Biophys. J* on April 23, 2019.

vitro and *in vivo*. Facilitated dissociation contrasts with classical kinetic models of bimolecular complexes that undergo a simple, binary on/off transitions, and have concentration-dependent association rates and concentration-independent dissociation rates. Instead, many proteins undergoing facilitated dissociation are multivalent, so that they may be associated with their substrates in one of several distinct binding states.

As a protein unbinds from DNA via facilitated dissociation, it forms an intermediate state between the fully bound and fully dissociated states, in which it is partially associated with its DNA substrate (Fig. 3.1A, state P). This partially bound state permits other biomolecules in solution, such proteins or DNA strands, to compete for contacts with either the protein or the DNA. Subsequent binding by a competitor molecule inhibits the initially bound protein from fully rebinding (Fig. 3.1A, state S). This accelerates (or "facilitates") the unbinding of the original protein from its binding site by inhibiting full rebinding of the partially bound protein and providing an additional dissociation pathway [85, 100, 105, 106, 144–146, 177, 178, 193, 199]. Since spontaneous unbinding without competitor biomolecules may be slow for these protein-DNA complexes (*e.g.*, $< 10^{-3}$ s^{-1} for the bacterial protein FIS), facilitated dissociation can lead to as much as a 100-fold enhancement in the dissociation rate at physiological protein concentrations ($\sim$ 10 nM for FIS) [99, 105].

Protein-DNA dissociation kinetics may be further modulated by applied forces. *In vivo*, $\gtrsim 1 - 10$ pN tension within DNA (or chromatin) can be induced by a number of intracellular and extracellular factors, including transmitted cytoskeletal forces [161, 173], transcription [200–203], and chromatin compaction [204–206], among other factors. Since many proteins that undergo facilitated dissociation preferentially associate with bent DNA, flexible DNA, or DNA that is not under tension [44, 67, 68, 100, 103], these *in vivo* forces may alter dissociation kinetics through their effects on the geometry of the DNA substrate. While the number of proteins bound to DNA indeed decreases under tension *in vitro* [67, 103, 207], the kinetics of tension-dependent proteins are unclear. Tension should increase the spontaneous dissociation rate of DNA-bound proteins [152, 164–166, 175]. However, since tension suppresses protein binding, it should also suppress the facilitated dissociation pathway of protein unbinding. These apparently competing effects suggest that the coupling between force and ligand-substrate geometry may generically lead to unexpected protein-DNA dissociation kinetics within cells.

Indeed, previous work on protein dissociation and unfolding demonstrated that complex force-dependent kinetics can be achieved for structures with multiple transition pathways. For example, for reactions that may occur by two different pathways, inhibition of one pathway can reduce the total reaction rate [170, 208–213]. When inhibition is driven by increasing applied force, the bound complex is referred to as a "catch bond" [214, 215]. A common conceptual picture for such bonds is that one of the transition states for dissociation resides at a smaller physical distance than the bound state, so that force drives the complex away from that transition [208, 209, 211, 212]. However, there are several different generic mechanisms by that may underlie such bonds [215]. Correspondingly, catch bonds have been experimentally observed for a wide variety of biological proteins and complexes that must withstand physiological forces. These include cellular adhesion proteins in humans (P- and L-selectin and integrin) [209, 210, 216, 217], metazoans (cadherin-catenin-actin) [218], and bacteria (FimH) [219, 220], the molecular motors myosin [221], dynein [222, 223], and PICH [224], microtubule-kinetochore interactions [225], and T-cell receptors under certain conditions [226]. In these models and experiments, bond strengthening and slowing of spontaneous dissociation with force are an intrinsic properties of the bound complex. In contrast, in the case of facilitated dissociation, it is the *extrinsic* effects of competitor biomolecules that may lead to anomalous kinetics, without bond strength enhancement and the suppression of spontaneous dissociation.

We hypothesize that the two dissociation pathways of DNA-binding proteins that undergo facilitated dissociation may together effectively generate catch-bond dissociation kinetics. We predict that when the spontaneous dissociation pathway dominates protein dissociation, increasing force on the DNA substrate enhances the dissociation rate, as is typical of slip bonds. In contrast, when the facilitated dissociation pathway dominates so that a biomolecule from solution must bind DNA to facilitate unbinding of the DNA-bound protein, the applied force should inhibit dissociation by inhibiting competitor binding; thus, we predict catch-bond behavior in this regime. We develop a coarse-grained simulation model and corresponding theoretical model for DNA-bending proteins interacting with DNA, and we explore their force-dependent facilitated dissociation kinetics in the geometry of a common *in vitro* single-molecule experiment (Fig. 3.1B) [106, 199, 227]. Within the model, we identify several distinct types of force-dependent dissociation kinetics: classical slip bonds, catch bonds, delayed onset catch bonds, and force-insensitive bonds. These bonds occur in different physical regimes, depending on the ratio of force sensitivities of each pathway. We investigate how different physical variables, including the preferred binding geometry of the protein-DNA complex and concentration of competitor molecules, may impact force-dependent dissociation. Altogether, the simulations and calculations demonstrate that applied or local mechanical stresses could dramatically modulate the facilitated dissociation of proteins, which could be probed in single-molecule experiments.

3.2 Mathematical and Computational Models and Methods

To explore the consequences of forces facilitated dissociation in the presence of applied forces, we consider a generic stochastic kinetic model (Fig. 3.1). In this model, a protein is initially fully bound to DNA (state F), and it must sequentially pass from fully to partially bound (state P) before dissociating into the unbound state (state U). While in the partially bound state, a competitor protein may invade the binding site in order to "saturate" it; in this state the binding site is simultaneously occupied by two partially bound proteins (state S). In the model, competitor binding prevents a partially bound protein from returning to the fully bound state. Experimentally, this may also transition the ligand-substrate complex

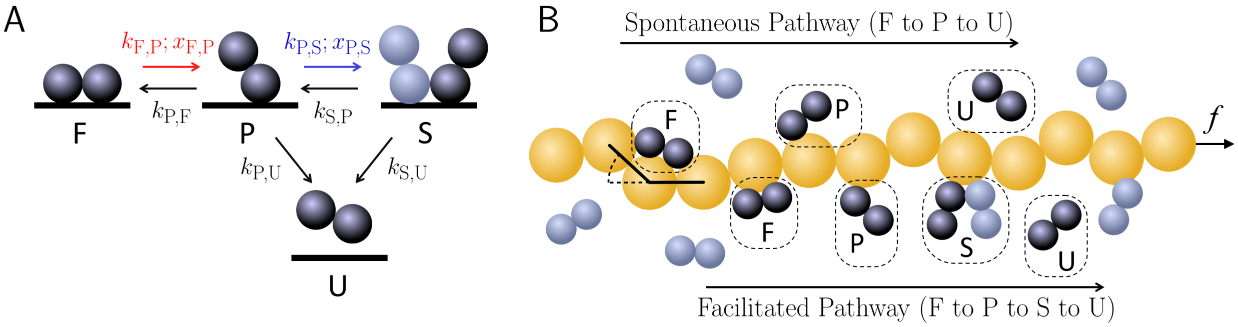

Figure 3.1: **A.** A schematic of the generic four-state model for protein-DNA dissociation kinetics. The protein-DNA complex may be have single fully bound protein (F), a single partially bound protein (P), two partially bound proteins (saturated, or S), or in the unbound state, no bound protein (U). In the model, the F to P and P to S unbinding steps are force dependent; these steps are indicated with the colored arrows. **B.** A drawing of the many proteins on a long DNA molecule, undergoing the dissociation kinetics depicted in (**A**). The top depicts spontaneous dissociation pathway, in which an initially fully bound protein first transitions to the partially bound state, and subsequently, to the unbound state, as shown by the proteins from left to right. The bottom shows the facilitated dissociation pathway, in which an initially fully bound protein transitions to the partially bound state, and then, upon competitor binding, to the saturated state, and finally to the unbound state (from left to right).

into a highly unstable configuration [85, 105]; however, this additional dissociation-enhancing effect is not considered here. In contrast to other schematically similar two-pathway reaction models [208, 209, 211–213], a factor extrinsic to the physical state of the bound complex, *i.e.*, the concentration of competitor biomolecules in solution, may be tuned to shift the relative weights of the two dissociation pathways. Despite the coarse-grained nature of the model, it has the salient features of facilitated dissociation: two dissociation pathways and extrinsic regulation by competitor proteins. Thus, the reaction scheme describes the unbinding kinetics of various DNA-binding proteins, such as RPA, FIS, and NHP6A [105, 193].

We focus on proteins that bind and bend a long DNA molecule, which is subjected to tension, f, as in single-molecule experiments (Fig. 3.1B) [39, 67, 100, 103, 228, 229] or certain *in vivo* conditions [55]. In this setup, when force is applied to DNA, it becomes more difficult to bend, and thus the protein binding affinity should decrease. Therefore, we assume that the rates, $k_{\mathrm{F,P}}$ and $k_{\mathrm{P,S}}$, of partial unbinding and competitor binding, respectively, depend on the force applied to the DNA.

We explore this generic model via two complementary approaches, described below. We develop a hybrid Brownian dynamics/kinetic Monte Carlo simulation model to explore force- and concentration-dependent protein dissociation behavior for proteins with different force sensitivities and binding geometries. In parallel, we perform numerical calculations for a theoretical model based on the simulations in order to more easily study the kinetics of individual proteins, analyze the contributions of the two dissociation pathways, and explore regimes of parameter space that are impractical to simulate. Together, the two approaches provide elucidate how the kinetics described by Fig. 3.1A may be manifested in the typical experimental scenarios depicted in Fig. 3.1B.

3.2.1 Hybrid Brownian Dynamics/Kinetic Monte Carlo Simulations

Model for DNA Polymer Dynamics

We adapt a coarse-grained Brownian dynamics simulation model for DNA-binding proteins binding that demonstrates both spontaneous and facilitated dissociation (Fig. 3.1B) [199, 227]. DNA is represented by a strand of $N = 100$ beads, indexed by i, of radius $a = 4$ nm at positions $\mathbf{r}_i$. The strand is tethered to a stationary boundary at one end, and a pulling force f is applied to the other end. Units are non-dimensionalized as follows: distance in with respect to bead radius ($\tilde{r}_{ij} = r_{ij}/a$), time with respect to the diffusion time of a single bead ($\tilde{t} = t/\tau_D$), and energy with respect to k_BT ($\tilde{U} = U/k_BT$). Throughout the text, variables with tildes denote non-dimensionalized quantities.

Neighboring beads in the DNA polymer are connected by Hookean springs, which is governed by the stretching potential:

$$\tilde{U}_S = \frac{\tilde{\kappa}_S}{2} \sum_{i,j=i+1} (\tilde{r}_{ij} - \tilde{b}_0)^2, \tag{3.1}$$

where $\tilde{r}_{ij}$ is the distance between adjacent beads i and j, and $\tilde{b}_0 = 2.0$ is the equilibrium distance between two beads. $\tilde{\kappa}_S = 200$ to prevent large deviations of $\tilde{r}_{ij}$ from $\tilde{b}_0$.

Excluded volume is included via a shifted Lennard-Jones potential:

$$\tilde{U}_{LJ} = \begin{cases} \tilde{\epsilon} \sum\limits_{ij} \left[\left(\frac{\tilde{b}_0}{\tilde{r}_{ij}} \right)^{12} - 2 \left(\frac{\tilde{b}_0}{\tilde{r}_{ij}} \right)^{6} + 1 \right] & \tilde{r}_{ij} \leq 2.5\tilde{b}_0, \\ 0 & \tilde{r}_{ij} > 2.5\tilde{b}_0, \end{cases} \tag{3.2}$$

where the magnitude of the potential is controlled by $\tilde{\epsilon} = 0.41$, and $\tilde{b}_0 = 2.0$ is location of the minimum.

A bending potential is included to maintain the stiffness of DNA as well as to incorporate the effects of the local bending deformations that may be induced by DNA-binding proteins:

$$\tilde{U}_B = \frac{\tilde{\kappa}_B}{2} \sum_{i=1}^{m-1} (\theta_i - \theta_{0,\mathrm{A}})^2, \tag{3.3}$$

where $\tilde{\kappa}_B = 6.25$ ensures a DNA persistence length of 50 nm, and θ_i is the angle between bonds of beads i and $i-1$ and beads i and $i+1$. $\theta_{0,\mathrm{A}}$ is the equilibrium angle between these two vectors, and its value depends on whether protein is bound to DNA bead i, which is denoted by the state index A.

Monomer dynamics are overdamped and governed by a Langevin equation that includes three potentials described above:

$$\frac{\partial \mathbf{r}_i}{\partial t} = - \sum_{j}^{N_{total}} \mu_{\mathbf{ij}} \cdot \nabla_j U(\mathbf{r}_{ij}; t) + \xi_i(t), \tag{3.4}$$

where $\mu_{\mathbf{ij}} = \delta_{ij}\boldsymbol{\delta}/(6\pi\eta a)$ is the freely-draining Stokes mobility matrix, η is the solvent viscosity, $\boldsymbol{\delta}$ is the identity matrix, δ_{ij} is the Kronecker delta, $U = U_S + U_{LJ} + U_B$ is the sum of all bead potentials, ξ_i is a random velocity that satisfies the fluctuation-dissipation theorem, $\langle \xi_i(t)\xi_j(0)\rangle = 2k_BT\mu_{\mathbf{ij}}\delta_{ij}\delta(t)$.

Model for Protein Binding and Unbinding Kinetics

Proteins in the system are implicitly modeled as a field of proteins that interacts with the DNA strand. A four-state model is used to describe the possible states of a DNA bead: fully bound (F), partially bound (P), saturated (S), and unbound (U), as shown in Fig. 3.1A. The partially bound and fully bound states correspond to a single protein interacting with a single DNA bead, while the saturated state corresponds to each of two proteins partially binding the same single DNA bead. DNA in either the unbound (U) or partially bound (P) states locally has an equilibrium bending angle of $\theta_{0,\mathrm{U}} = \theta_{0,\mathrm{P}} = 0$, while a non-zero equilibrium angle is associated with the fully bound (F) and saturated states (S): $\theta_{0,\mathrm{F}} = \theta_{0,\mathrm{S}} > 0$.

Transitions between two states, A and B, are dictated by state-dependent energy barriers, $\Delta\tilde{E}_{\mathrm{A,B}}$. The binding state of a DNA bead, denoted by Ω_i, is updated with a Monte Carlo step every $\tilde{\tau}_{MC} = 0.05$. This time step is chosen to ensure that if an (implicit) protein is found to have diffused so that it is near the DNA binding site, the subsequent binding time, τ_b, matches the diffusion time, τ_D, of a single bead [199]. A random number, $0 \leq \zeta < 1$, is generated, and for DNA site i in state $\Omega_i = \mathrm{A}$, the binding update occurs as follows:

$$\Omega_i(t) = \begin{cases} \mathrm{B} \text{ if } \zeta < e^{-\Delta E_{\mathrm{A,B}}}, \\ \mathrm{A} \text{ if } \zeta > e^{-\Delta E_{\mathrm{A,B}}}. \end{cases} \tag{3.5}$$

Most transitions in this model have fixed energy barriers for binding or unbinding: $\Delta\tilde{E}_{\mathrm{U,P}} = 3$, $\Delta\tilde{E}_{\mathrm{P,F}} = 5$ (where the additional $2k_BT$ accounts for entropy loss upon full binding [227]), and $\Delta\tilde{E}_{\mathrm{P,U}} = \Delta\tilde{E}_{\mathrm{S,P}} = 10$. Due to the universal nature of facilitated dissociation, the results are broadly applicable beyond this particular set of energy barrier choices [199].

However, two key transitions have energy barriers that vary as a function of force. The form of the energy barrier for the competitor protein binding event to DNA site i in the facilitated dissociation pathway (P to S) is:

$$\Delta\tilde{E}_{\mathrm{P,S}} = x_{\mathrm{P,S}}\frac{\tilde{\kappa}_B}{2}\left(\theta_i - \theta_{0,\mathrm{S}}\right)^2 + \Delta\tilde{E}^*_{\mathrm{b}}, \tag{3.6}$$

where the first term in Eq. 3.6 accounts for the effect of applied force on the binding energy and the second term is a constant energy barrier. As more force is applied to the DNA strand, the average angle, θ_i, between DNA bead bond vectors increases. Therefore, on average, the DNA binding site is further from its preferred binding geometry ($\theta_{0,\mathrm{S}}$) at higher applied forces, which decreases the likelihood of protein binding. The force sensitivity parameter, $x_{\mathrm{P,S}} > 0$, controls the strength of the effect of force on the binding energy barrier. To ensure that the zero-force ($f = 0$) total protein dissociation rate, $\tilde{k}_{\mathrm{off}}$, is the same for all parameters, we include an adjustable parameter $\Delta\tilde{E}^*_b$ to account for the effects of the force-dependent term on the zero-force off rate, listed in Table 3.1.

The energy barrier for the force-dependent partial unbinding step (F to P) has the form:

$$\Delta\tilde{E}_{\mathrm{F,P}} = x_{\mathrm{F,P}}[\tilde{\kappa}_B\left(\theta_i - \theta_{0,\mathrm{F}}\right)] + \Delta\tilde{E}^*_{\mathrm{Ub}}, \tag{3.7}$$

where the second term is a constant unbinding energy barrier. The first term is the derivative of the bending energy term in Eq. 3.6 ($\frac{\tilde{\kappa}_B}{2}\left(\theta - \theta_{0,\mathrm{B}}\right)^2$), but multiplied by the force sensitivity parameter $x_{\mathrm{F,P}}$; it accounts for the change in the unbinding energy barrier due to the local bending conformation of DNA, which is related to the force applied to the DNA strand [227]. The force sensitivity $x_{\mathrm{F,P}} > 0$ controls the strength of the force-dependent term. Similar to Eq. 3.6, the last term, $\Delta\tilde{E}_{\mathrm{Ub}}$, is an adjustable parameter that matches $\tilde{k}_{\mathrm{off}}$ at $f = 0$ for all parameters and can be found in Table 3.2. Physically, we may interpret $x_{\mathrm{F,P}}$ as the distance

Table 3.1: Reference energy barrier values ($\Delta\tilde{E}_b^*$) used in Eq. 3.6. These values are found by parameterizing Eq. 3.6 to match all k_{off} at $f = 0$. All other values in Eq. 3.6 are constant (other than the variable θ, which is measured instantaneously in the simulation).

$\theta_{0,\text{S}}$ and $\theta_{0,\text{F}}$	$x_{\text{P,S}}$	$\Delta\tilde{E}_b^*$
$\pi/6$	1	1.2
	5	0.72
	10	0.4
	25	-0.06
$\pi/3$	1	0.1
	5	-4
	10	-9
	25	-24
$\pi/2$	1	-2.6
	5	-17.1
	10	-35.5
	25	-90

Table 3.2: Reference energy barrier values used in Eq. 3.7. These values are found by parameterizing Eq. 3.7 to match all k_{off} at $f = 0$.

$\theta_{0,\text{S}}$ and $\theta_{0,\text{F}}$	$x_{\text{F,P}}$	$\Delta\tilde{E}_{Ub}^*$
$\pi/6$	≤ 0.01	10
	0.1	9.95
	0.2	9.88
	0.3	9.83
	0.5	9.84
	0.75	9.95
	1.0	10.16
	2.0	11.7
$\pi/3$	≤ 0.25	10
	0.3	10.01
	0.5	10.16
	0.75	10.5
	1.0	10.95
	2.0	14.35
$\pi/2$	≤ 0.1	10
	0.2	10.1
	0.3	10.17
	0.5	10.42
	1.0	11.54
	2.0	15.75

a protein must be displaced in order to partially dissociate, or the position of the transition energy barrier [165–167, 212, 215].

The force dependence of $k_{\mathrm{F,P}}$ but not $k_{\mathrm{P,U}}$ models insensitivity of spontaneous dissociation to applied forces, while partial dissociation events depend on force. These kinetics are suggested by observations of DNA-binding proteins such as NHP6A, HMGB, and HU [39, 229]. Furthermore, the force dependence of the saturation transition models the inhibition of protein binding by tension (*e.g.*, [103]), which we have assumed is relevant to competitor protein binding.

We define the sensitivity ratio as $x_{\mathrm{P,S}}/x_{\mathrm{F,P}}$, which is a measure of the relative sensitivities to force of each dissociation pathway. A high ratio (> 100) indicates that the facilitated pathway is much more sensitive to force, whereas a low ratio (< 10) indicates that the a spontaneous pathway is much more sensitive to force.

We measure the off rate, $\tilde{k}_{\mathrm{off}}$, in simulations by counting the number, $n_B(t)$, of initially bound proteins that remain bound to the DNA over time. We initialize the DNA strand with every nonspecific binding site in the fully bound state, and then allow these originally bound proteins to unbind and competitors to bind over time. We simulate until all originally bound proteins unbind. We take the average of 100 independent trajectories to obtain $\langle n_B(t) \rangle$, and thus the mean dissociation rate, $\tilde{k}_{\mathrm{off}}$.

3.2.2 Theoretical Geometric Model and Numerical Calculations of Mean-First Passage Time

To gain a better understanding of the geometric protein-DNA binding model, we numerically compute the expected dissociation rates for a corresponding theoretical using standard statistical mechanical methods.

Within the stochastic kinetic model described by Fig. 3.1A and the equations above, we calculate the average protein dissociation rate as the inverse of the mean first-passage time

[105, 230]:

$$k_{\text{off}} = \langle \tau \rangle^{-1} = \frac{k_{\text{F,P}}(k_{\text{P,S}}k_{\text{S,U}} + k_{\text{P,U}}(k_{\text{S,P}} + k_{\text{S,U}}))}{k_{\text{P,F}}(k_{\text{S,P}} + k_{\text{S,U}}) + k_{\text{F,P}}(k_{\text{P,S}} + k_{\text{S,P}} + k_{\text{S,U}}) + k_{\text{P,S}}k_{\text{S,U}} + k_{\text{P,U}}(k_{\text{S,P}} + k_{\text{S,U}})}, \tag{3.8}$$

where $k_{\text{A,B}}$ is the transition rate from state A to state B. As above, $k_{\text{F,P}}$ and $k_{\text{P,S}}$ depend on force. In addition, $k_{\text{P,S}}$ is proportional to the concentration of competitor protein.

The expected dissociation rate is given by Eq. 3.8. To use that expression, we must calculate the mean rates of partial dissociation, $\langle k_{\text{F,P}} \rangle$, and binding-mediated saturation, $\langle k_{\text{P,S}} \rangle$. These are given by averaging with respect to the equilibrium distribution of local DNA bending angles, which is weighted by the potentials of the geometric model above and the force that tends to align the DNA polymer along the tension axis. Thus, the partial dissociation rate is given by:

$$\langle k_{\text{F,P}}(f) \rangle = \frac{\int_0^\pi \nu e^{\Delta \tilde{E}_{\text{F,P}}(\theta)} e^{-(\tilde{U}_B(\theta) - 2b_0 f \cos\theta)} \sin\theta d\theta}{\int_0^\pi e^{-(\tilde{U}_B(\theta) - 2b_0 f \cos\theta)} \sin\theta d\theta}, \tag{3.9}$$

where $\nu = 1/\tau_{\text{MC}}$ is the attempt rate for partial unbinding, which is chosen to match the simulations. Similarly, the competitor binding (saturation) rate is given by:

$$\langle k_{\text{P,S}}(c, f) \rangle = \frac{\int_0^\pi \gamma c e^{\Delta \tilde{E}_{\text{P,S}}(\theta)} e^{2b_0 f \cos\theta} \sin\theta d\theta}{\int_0^\pi e^{2b_0 f \cos\theta} \sin\theta d\theta}, \tag{3.10}$$

where c is the concentration of competitor proteins and γ is the binding attempt rate, which is again chosen to match the simulations.

We numerically compute these average rates and insert them into Eq. 3.8 to obtain the mean dissociation rate. All rate constants are reported as non-dimensionalized quantities, which are normalized by the corresponding zero-force, zero-concentration rate constants. This mimics the adjustable energy barriers in Eqs. 3.6 and 3.7.

3.3 Results

3.3.1 Geometric Model Coupling Force and Dissociation

The four-state model described above allows proteins to unbind via two different dissociation pathways, which are illustrated in Fig. 3.1B. The first is a spontaneous dissociation pathway, in which a protein (black dimer) sequentially transitions from fully bound to partially bound to unbound spontaneously, without the participation of competitor protein (gray dimer). The second dissociation pathway is the concentration-dependent facilitated pathway, where a protein transitions from fully bound to partially bound, and then a competitor protein binds to the partially vacated binding site and assists the original protein in unbinding. The fully bound and saturated proteins physically interact with the DNA substrate by bending the DNA polymer. This changes the local equilibrium bond angle, $\theta_{0,\mathrm{A}}$. There are two force dependencies included in the models, which are governed by the force sensitivity parameters, $x_{\mathrm{F,P}}$ and $x_{\mathrm{P,S}}$ (see methods section above and Fig. 3.1A). In general, these two force dependencies enable the applied force, f, to accelerate the F-P transition and inhibit the P-S transition. By varying the force dependencies of the rates associated with the two different pathways, we observe a range of bond dissociation behaviors, described below.

3.3.2 Dissociation Rates in Limiting Scenarios

To demonstrate the main phenomenological features of our model, we first investigate the simplest scenarios, in which the system has only one force dependence (*i.e.*, one of either $x_{\mathrm{F,P}} > 0$ or $x_{\mathrm{P,S}} > 0$). In these cases, the net protein dissociation rate depends in a simple manner on the single force-dependent transition rate (either $k_{\mathrm{F,P}}$ or $k_{\mathrm{P,S}}$).

Force-Dependent Spontaneous Dissociation

We first consider the protein-DNA binding model with the force dependence restricted to only the spontaneous dissociation pathway. Thus, we vary $x_{\mathrm{F,P}}$ while fixing $x_{\mathrm{P,S}} = 0$ so that only the unbinding transition from fully bound to partially bound depends on force. Here, the model demonstrates the canonical slip bond behavior; the bond is weakened as more force is applied, so the bond lifetime decreases. This is manifested in the model by an observed increase in the dissociation rate, $\tilde{k}_{\mathrm{off}}$. The force dependence of partial unbinding models the force dependence of observed "microdissociation" events, which is observed, for example, in experiments with HMGB and NHP6A [229].

As force is applied to the DNA polymer, it straightens, which decreases the local bending angle, θ. This frustrates the fully bound protein conformation, which has binding energy proportional to $(\theta - \theta_{0,\mathrm{F}})$, with $\theta_{0,\mathrm{F}} > 0$ (Eq. 3.7). Any $x_{\mathrm{F,P}} > 0$ for both the theoretical and simulation model incorporates this decrease in the bending force in the F to P unbinding step, leading to a more favorable unbinding step at high forces. This leads faster protein dissociation as force is increased, and results in the slip-bond behavior in simulation. This is true even when competitor proteins facilitate dissociation (in a force-independent manner), as shown in Figs. 3.2A and A.1A.

As $x_{\mathrm{F,P}}$ increases, the total dissociation rate becomes more force sensitive. As illustrated by the transition rate numerically calculated from Eq. 3.9, shown in Fig. 3.2B, the spontaneous dissociation rate, $k_{\mathrm{F,P}}$ increases more rapidly with force for larger $x_{\mathrm{F,P}}$. Thus, in scenarios in which only partial dissociation depends on force, tension within DNA may accelerate dissociation of multivalent DNA-bending proteins.

Force-Dependent Facilitated Dissociation

We also investigate the case in which only the facilitated dissociation pathway depends on force, $x_{\mathrm{P,S}} > 0$ and $x_{\mathrm{F,P}} = 0$; this leads to catch-bond behavior. This force dependence

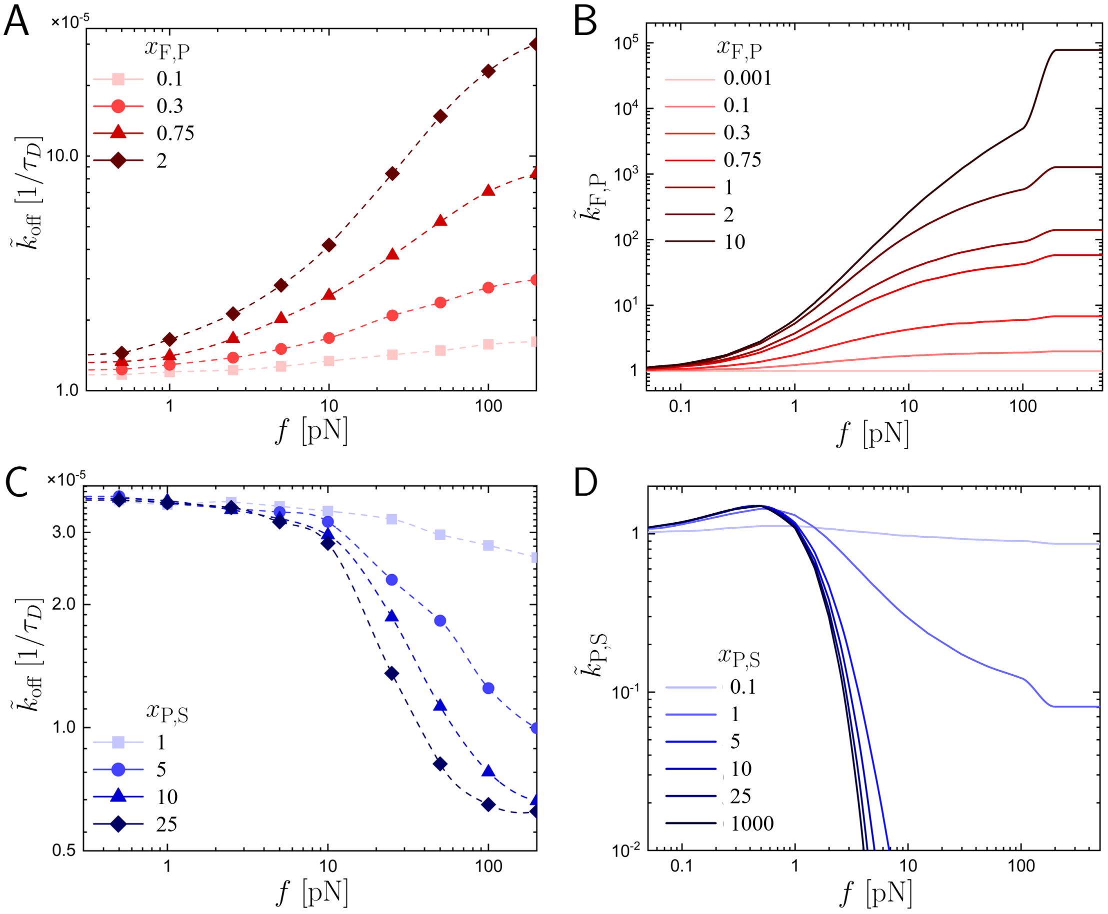

Figure 3.2: **A.** In simulations with force dependence only for partial dissociation (*i.e.*, $x_{\mathrm{F,P}} > 0$ and $x_{\mathrm{P,S}} = 0$), the overall dissociation rate, $\tilde{k}_{\mathrm{off}}$, increases with force, f. The force dependence strengthens with increasing force sensitivity, $x_{\mathrm{F,P}}$ (light to dark red). **B.** The normalized partial dissociation rate, $\tilde{k}_{\mathrm{F,P}}$ (which is different from the overall k_{off} shown in panel A), calculated from Eq. 3.9. As $x_{\mathrm{F,P}}$ increases, the partial dissociation rate, $k_{\mathrm{F,P}}$, increases; this underlies the slip-bond behavior observed in simulations. **C.** In simulations with force sensitivity only only for competitor binding ($x_{\mathrm{F,P}} = 0$ and $x_{\mathrm{P,S}} > 0$), the dissociation rate, $\tilde{k}_{\mathrm{off}}$, decreases with increasing force. As the force sensitivity, $x_{\mathrm{P,S}}$, increases (light to dark blue), the force dependence of the dissociation rate becomes sharper and the onset of strong force dependence shifts to lower forces. **D.** The normalized competitor binding rate, $k_{\mathrm{P,S}}$ (different than k_{off} shown in panel C) calculated from Eq. 3.10. For large enough forces, $k_{\mathrm{P,S}}$ is generally suppressed by increasing force, which results in catch-bond kinetics. As $x_{\mathrm{P,S}}$ increases, $k_{\mathrm{P,S}}$ is suppressed more sharply and for smaller f. Results in all panels are for $c = 100$ μM. Simulation results (A and C) are for $\theta_{0,\mathrm{F}} = \theta_{0,\mathrm{S}} = \pi/6$ and theoretical results (B and D) are for $\theta_{0,\mathrm{F}} = \theta_{0,\mathrm{S}} = \pi/3$.

increases the energy barrier for a competitor protein to bind to a partially occupied DNA site. This models the inhibition of binding by DNA-bending proteins when DNA bending is inhibited by tensile forces [103, 227].

Applied forces in this scenario decrease the total dissociation rate by suppressing competitor binding, and thus slowing protein dissociation via the facilitated pathway. In the model, force decreases the average bending angle $\langle\theta\rangle$. This increases the energy barrier for competitor protein binding, which is proportional to $(\theta - \theta_{0,\mathrm{S}})^2$. As shown in Fig. 3.2C, for finite competitor concentrations, the off rate, $\tilde{k}_{\mathrm{off}}$, decreases with increasing force, f, in simulations, as expected for a catch bond.

For sufficiently high forces, f, and force sensitivities, $x_{\mathrm{P,S}}$, the off rate is insensitive to force, as seen for $f > 100$ pN and $x_{\mathrm{P,S}} = 25$. For even sharper force dependencies (larger $x_{\mathrm{P,S}}$), competitor binding should be suppressed for any $f > 0$. Under such conditions, the facilitated dissociated pathway is so strongly inhibited by force that proteins can effectively only dissociate via the spontaneous pathway, leading to a force-independent k_{off}. This trend can be inferred from the observed shift with increasing $x_{\mathrm{P,S}}$ in simulations (from light to dark blue) and for very large $x_{\mathrm{P,S}}$ in the theory (Fig. A.1B). The numerically calculated transition rate, $k_{\mathrm{P,S}}$, shown in Fig. 3.2D illustrates the changes in the facilitated rate with $x_{\mathrm{P,S}}$ and f that govern the total dissociation rate. The theoretical $k_{\mathrm{P,S}}$ is mostly consistent with simulations, but contrary to expectations from the simulations, the calculated rate is non-monotonic in force, increasing for small f. This occurs in the theoretical model because low forces shift the angular distribution toward the equilibrium angle (for $\theta_{0,\mathrm{S}} < \pi/2$), which enhances the competitor binding rate. In simulations, this effect is suppressed by excluded volume interactions, which reduce the mean bending angle at zero force.; however, excluded volume can be incorporated into a more detailed version of the theoretical model (Fig. A.2).

The two distinct variable force dependencies in the model thus have opposing effects on the total dissociation rate. However, in contrast to these limiting scenarios, physiological protein dissociation may have multiple force-dependent kinetic barriers. These force dependencies have differing degrees of control over the protein dissociation kinetics in different physical regimes, described below.

3.3.3 Multivalent Protein Dissociation with Multiple Force Dependencies

While the effect of force on each dissociation pathways is straightforward when considered independently, we observe more complex behavior in scenarios in which both pathways are force dependent. In this case, inhibition of competitor protein binding by force suppresses the facilitated pathway, which competes with the force-enhanced partial unbinding that accelerates the spontaneous dissociation pathway.

As we observe in Fig. 3.3A and B, this competition between the two pathways leads to three classes of bonds: the slip and catch bonds discussed above, and a hybrid bond we refer to as a "delayed catch bond." The delayed catch bond is characterized by an off rate with a slip-bond force dependence for low forces and a transition to catch-bond behavior with increasing force; hence the onset of the catch bond is delayed as a function of force. At very high forces, the off rate may either increase with force (reverting to a slip bond) or be essentially insensitive to force. Fig. 3.3A and B show the transitions between catch, delayed catch, and slip bonds as a function of the force sensitivity ratio, $x_{\mathrm{P,S}}/x_{\mathrm{F,P}}$ for the particular parameter choice $x_{\mathrm{P,S}} = 10$.

For low sensitivity ratios, the force dependence of the facilitated dissociation pathway is weak compared to that of the spontaneous pathway, whereas for high sensitivity ratios, the force dependence of the facilitated pathway is stronger. In both simulations and theory, for low sensitivity ratios, the protein-DNA complex acts as a slip bond, dissociating more rapidly with increasing force (red lines). As before, this occurs because force stimulates spontaneous dissociation while having relatively little effect on the competitor protein binding required for facilitated protein unbinding (*e.g.*, in Fig. 3.2, compare derivatives of dark lines in B to light lines in D).

As the sensitivity ratio is increased, the force has a greater inhibitory effect on the facilitated dissociation pathway. For moderate sensitivity ratios, this manifests itself at ~ 10 pN forces in the model as a change from an increasing to a decreasing off rate (dark red and purple lines in Fig. 3.3A and B). The onset of catch-bond kinetics is delayed in this scenario because the spontaneous pathway has a non-negligible force dependence, while the competitor binding rate, $k_{\mathrm{P,S}}$, in the facilitated pathway is less sensitive to small forces. This disparity arises because $k_{\mathrm{F,P}}$ depends purely exponentially on the bending angle, $\theta_{0,\mathrm{F}}$, whereas the competitor binding rate has a broad ($x_{\mathrm{P,S}}$-dependent) peak around the preferred binding angle, $\theta_{0,\mathrm{S}}$ (see Eqs. 3.6 and 3.7). Moreover, at low forces, by accelerating the transition from fully to partially bound, the facilitated dissociation pathway is also effectively accelerated because the protein-DNA complex is more frequently susceptible to invasion by a competitor protein.

For very high sensitivity ratios, the force dependence of the facilitated pathway is dominant. Here, we observe catch-bond kinetics in the simulation, while the numerical calculation predicts that the onset of the catch bond is delayed to higher forces (blue lines in Fig. 3.3A and B). This discrepancy occurs because the Gaussian chain approximation used in the theoretical model results in a small enhancement in the rate $k_{\mathrm{P,S}}$ for small forces (Fig. 3.2). This effect is suppressed in simulations by the additional chain stiffness imparted by excluded volume interactions. Nonetheless, we observe predominantly catch-bond kinetics in this regime because the facilitated dissociation pathway is far more sensitive than the spontaneous pathway to the applied force.

To characterize the broader force-dependent dissociation kinetics of this model, we measure the derivative of the dissociation rate for a range of sensitivity ratios, $x_{\mathrm{P,S}}/x_{\mathrm{F,P}}$, and forces, f. Fig. 3.3C and D shows the resulting phase diagrams for the simulations and theory. Here, we observe three types of force-dependent dissociation kinetics: force-insensitive bonds ($|\partial \tilde{k}_{\mathrm{off}}/df| < \sigma$, where $\sigma \ll 1$ is a threshold value; gray points), slip bonds ($\partial \tilde{k}_{\mathrm{off}}/df > \sigma$;

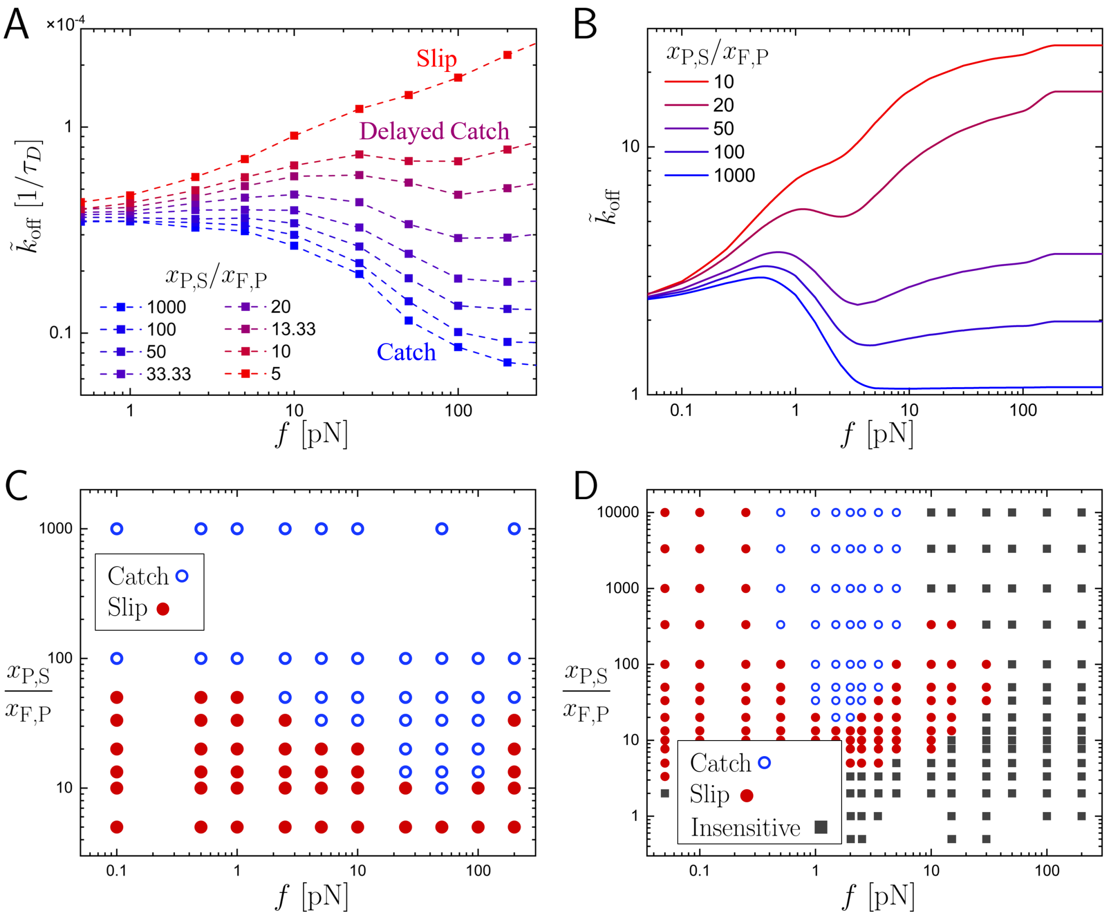

Figure 3.3: **A.** Simulation off rates, $\tilde{k}_{\mathrm{off}}$, as a function of force, f and sensitivity ratio, $x_{\mathrm{P,S}}/x_{\mathrm{F,P}}$, at $x_{\mathrm{P,S}} = 10$ and $c = 100\mu\mathrm{M}$. As the sensitivity ratio decreases (by increasing $x_{\mathrm{F,P}}$), dissociation kinetics change from catch-bond (blue) to delayed-catch-bond (purple and dark red) to slip-bond (red) behavior. **B.** Theoretical off rates as a function of force and sensitivity ratio. Similar to the simulation data, as the ratio $x_{\mathrm{P,S}}/x_{\mathrm{F,P}}$ decreases, the protein-DNA complex crosses over from catch-bond to delayed-catch-bond to slip-bond kinetics. **C.** A phase diagram in the ratio-force plane, constructed from the simulation data, shows physical regimes of decreasing k_{off}, corresponding to catch bonds (open blue circles), and increasing k_{off}, corresponding to slip bonds (filled red circles). **D.** The theoretical diagram shows regimes with catch-bond, slip-bond, and force-insensitive-bond kinetics (blue hollow circles, red filled circles, and gray filled squares, respectively). The theory agrees qualitatively with simulations, and reveals an additional force-insensitive regime for very low sensitivity ratios, $x_{\mathrm{P,S}}/x_{\mathrm{F,P}}$.

red), catch bonds ($\partial \tilde{k}_{\text{off}}/df < -\sigma$; blue). Combinations of these types of kinetics result in the three general classes of bonds described above.

For high force sensitivity ratios, where $x_{\text{P,S}} \gg x_{\text{F,P}}$, we always observe catch-bond kinetics in simulations ($\partial \tilde{k}_{\text{off}}/\partial f < -\sigma$). In contrast, the theoretical model predicts that the onset of catch-bond kinetics should arise at non-zero force for all sensitivity ratios. Again, this difference is due to the Gaussian chain approximation utilized in the theoretical model.

For lower force sensitivity ratios, we observe a growing domain of slip-bond behavior as $x_{\text{P,S}}/x_{\text{F,P}}$ decreases, and the transition to catch-bond kinetics occurs at higher forces. This occurs because the force dependence of competitor binding is weaker than that of partial dissociation. Below a critical sensitivity ratio, the force dependence of partial protein dissociation completely dominates, and only classical slip-bond kinetics are observed. For very low sensitivity ratios, below the minimum value tested in simulations, the theory predicts force-insensitive kinetics (Fig. 3.3D). In this regime, $x_{\text{F,P}}$ is large and the spontaneous pathway is so sensitive to force so that partial dissociation occurs almost instantaneously for any finite f. Thus, even though the facilitated pathway remains sensitive to force (via $x_{\text{P,S}}$), it no longer significantly accelerates dissociation; this is because because the rebinding transition (P to F) that is prevented by competitor binding no longer delays protein dissociation.

For all sensitivity ratios, the theoretical model predicts a force-insensitive domain for sufficiently high forces. This occurs because the facilitated pathway is completely suppressed by force and the spontaneous pathway cannot be further enhanced by additional application of force. In the simulations, this predicted force-independent regime likely occurs at forces above the maximum simulated f.

In summary, in our protein dissociation model, several varieties of force-dependent kinetics are possible. This behavior is largely controlled by the force sensitivity ratio, which determines the relative strength of the force dependence of the facilitated dissociation pathway as compared to that of the spontaneous dissociation pathway. The competition between the force dependencies of these two dissociation pathways leads to hybrid kinetic behaviors ("delayed catch bonds"), or in unbalanced cases, distinct limiting scenarios (slip or catch bonds).

3.3.4 Effects of Binding Geometry

A key determinant of protein-DNA interactions is the geometry of the binding interface. Critically, this local geometry can determine the strength and nature of the coupling between applied forces and dissociation kinetics. To study how geometric factors may alter the force dependence of proteins undergoing facilitate dissociation, we varied the parameter $\theta_{0,\mathrm{A}}$, which sets the equilibrium DNA bending angle for protein binding (Eq. 3.3). Alterations to $\theta_{0,\mathrm{A}}$ thus regulate how the applied force, f, changes the overall dissociation rate, $\tilde{k}_{\mathrm{off}}$.

We consider three different values of $\theta_{0,\mathrm{F}} = \theta_{0,\mathrm{S}} \equiv \theta_0$ in the simulation model: $\pi/6$, $\pi/3$, and $\pi/2$. We measure the dissociation rate, $\tilde{k}_{\mathrm{off}}$, at different forces, f, and force sensitivity ratios, $x_{\mathrm{P,S}}/x_{\mathrm{F,P}}$ (fixing $x_{\mathrm{P,S}} = 10.0$ and $\theta_{0,\mathrm{U}} = \theta_{0,\mathrm{P}} = 0$ for simplicity). Contour plots showing the dissociation rates for $\theta_0 = \pi/6$, $\pi/3$, and $\pi/2$ are shown in Fig. 3.4A-C, respectively. For all three cases, we see the same qualitative dissociation kinetics discussed above: catch bonds when the facilitated pathway is most sensitive to force (large $x_{\mathrm{P,S}}/x_{\mathrm{F,P}}$), slip bonds when the spontaneous pathway is most sensitive to force (smaller $x_{\mathrm{P,S}}/x_{\mathrm{F,P}}$), and delayed catch bonds when the force dependencies of the two pathways compete (intermediate $x_{\mathrm{P,S}}/x_{\mathrm{F,P}}$). These qualitative observations also hold for the theoretical model (Fig. A.3).

Nonetheless, binding geometry has a marked impact on the transitions between these dissociation behaviors. Most notably, as θ_0 is increased, the range of force sensitivity ratios, $x_{\mathrm{P,S}}/x_{\mathrm{F,P}}$, in which delayed catch bonds are observed shrinks. This effect arises because protein-DNA complexes with a large equilibrium DNA-bending angle are most strongly impacted by the applied force; straight DNA conformations induced by applied force have an energetic cost for protein binding that increases with θ_0 (see Eqs. 3.6 and 3.7). Consequently, for large preferred bending angles, even small forces can induce sharp changes to the partial

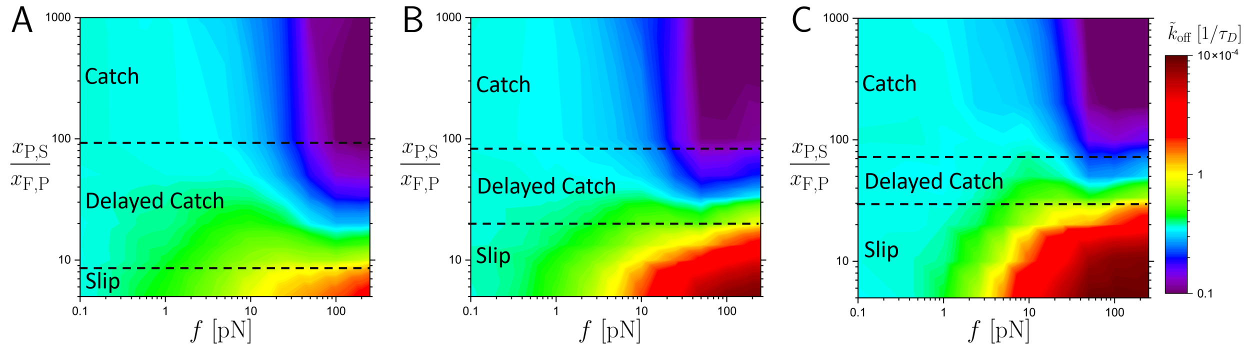

Figure 3.4: Contour plots of $\tilde{k}_{\mathrm{off}}$ as a function of applied force, f, and sensitivity ratio, $x_{\mathrm{P,S}}/x_{\mathrm{F,P}}$, for bending angles $\theta_{0,\mathrm{F}} = \theta_{0,\mathrm{S}} \equiv \theta_0 = \pi/6$, $\pi/3$, and $\pi/2$ (**A-C**, respectively) with $x_{\mathrm{P,S}} = 10$ and $c = 100$ μM. Approximate boundaries between catch bond, delayed catch bond, and slip bond regimes are denoted by black dotted lines. Large off rates, corresponding to faster dissociation, are red, while small off rates (slower dissociation) are purple.

dissociation and competitor binding rates. Thus, the regime in which the two pathways compete narrows for highly bent interfaces because their respective force-dependent rates, $k_{\mathrm{F,P}}$ and $k_{\mathrm{P,S}}$, vary over different narrow force scales.

In addition to qualitative changes in the transitions between different regimes, we observe quantitative differences in the off rate as a function of θ_0. In Fig. 3.4, purple regions of the contour plots indicate a slow $\tilde{k}_{\mathrm{off}}$, while red regions indicate fast $\tilde{k}_{\mathrm{off}}$. For larger bending angles, the red region extends to lower forces, which indicates that slip dissociation can be rapid even for small forces because of the mechanical energetic cost for the protein to remain bound to DNA. In contrast, $\tilde{k}_{\mathrm{off}}$ for the catch-bond regime is not drastically altered because it is minimized as the facilitated pathway is suppressed by force.

Altogether, altering the binding geometry by varying θ_0 changes the degree of coupling between mechanics and kinetics. This coupling modulates the energy barriers between different binding states by determining the energy required for the protein to bend DNA. Thus, the binding geometry is a critical factor in regulating the competition between dissociation pathways and determining the force dependence of the overall protein dissociation rate.

3.3.5 Effects of Competitor Concentration

Since the phenomenon of facilitated protein dissociation is characterized by concentration-dependent off rates, we study the force-dependent kinetics at different ambient concentrations of competitor molecules. At zero force, as the competitor concentration, c, increases, more initially bound proteins dissociate via the facilitated dissociation pathway. We thus hypothesized that increasing c could lead to the facilitated pathway becoming dominant for small forces and force sensitivity ratios; in turn, catch-bond kinetics would become more prevalent.

We consider the two limiting scenarios of high and low sensitivity ratios, which respectively, exhibit catch- and slip-bond kinetics at $c = 100\ \mu$M. We investigate how changing the concentration from 1 μM to $> 10^4\ \mu$M modulates the dissociation behavior. Plots showing $\tilde{k}_{\mathrm{off}}$ as a function of force, f, and concentration, c, are shown in Fig. 3.5A-D for simulations (A and C) and theory (B and D). Their corresponding bond phase diagrams are shown in Fig. 3.5E-H.

We first study the effect of varying competitor concentration on the dissociation with a large force sensitivity ratio. For concentrations spanning at least three orders of magnitude in simulations, we observe only catch bonds or, at low c, force-insensitive bonds, as shown in Fig. 3.5A and E. The spontaneous pathway depends on force so weakly that almost completely irrespective of concentration, the facilitated pathway is more sensitive to force. For high concentrations (blue lines), this leads to a $\tilde{k}_{\mathrm{off}}$ that decreases with force, *i.e.*, a catch bond. For lower concentrations, $c \leq 10$ muM (red lines), there are very few competitor proteins available to participate in facilitated dissociation. So, while the facilitated dissociation pathway is sensitive to force, DNA-bound proteins rarely dissociate via this pathway, which leads to a nearly force-independent off rate.

As with varying the force sensitivity ratio, these observations hold for the theoretical model with the caveat that we observe delayed onset catch bonds instead of catch bonds

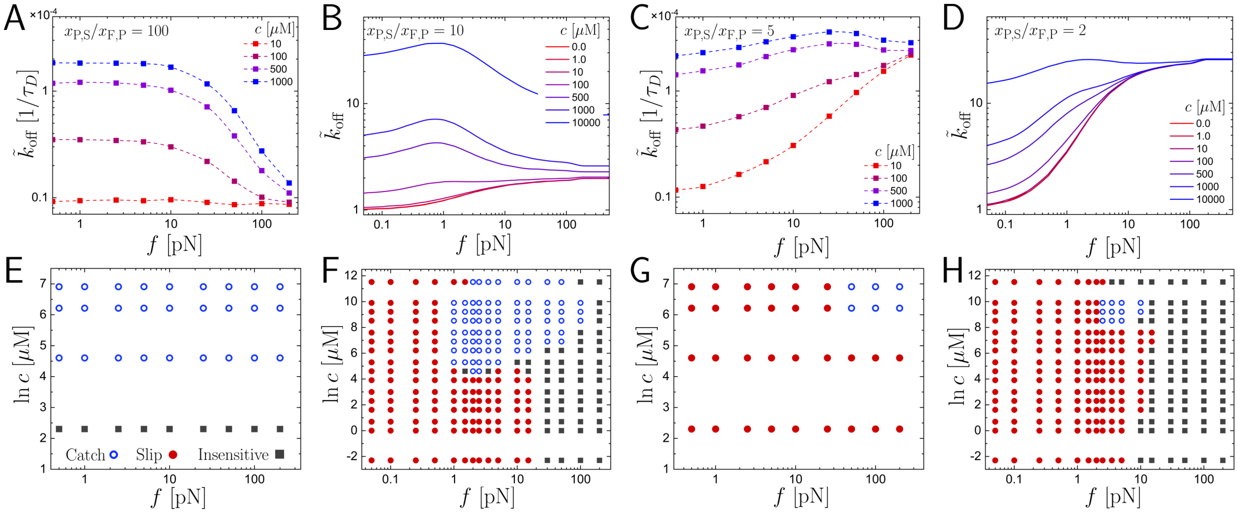

Figure 3.5: **A-B:** Off rates, $\tilde{k}_{\rm off}$, as a function of force, f, at various concentrations, c, for the simulation and theoretical models, respectively. Different colored curves show different competitor concentrations, ranging from low (red) to high (blue). For simulation results (A), $\theta_{0,\rm F} = \theta_{0,\rm S} = \pi/6$ and $x_{\rm P,S}/x_{\rm F,P} = 100$. For theoretical results (B) $\theta_{0,\rm F} = \theta_{0,\rm S} = \pi/3$ and $x_{\rm P,S}/x_{\rm F,P} = 10$. **C-D**: $\tilde{k}_{\rm off}$ for the simulation and theoretical models, respectively. For simulation results (C), $\theta_{0,\rm F} = \theta_{0,\rm S} = \pi/6$ and $x_{\rm P,S}/x_{\rm F,P} = 5$. For theoretical results $\theta_{0,\rm F} = \theta_{0,\rm S} = \pi/3$ and $x_{\rm P,S}/x_{\rm F,P} = 2$. **E-H:** Corresponding phase diagrams of indicating the bond type as determined by $\partial k_{\rm off}/\partial f$, plotted in the concentration-force plane. Each panel correspond to the $\tilde{k}_{\rm off}$ plots directly above it.

(Fig. 3.5B and F). Again, this is due to discrepancies between the low-force DNA conformations, and thus, competitor binding rates, found in the different models. Additionally, the theoretical model allows us to observe the slip-bond regime that is present for very low competitor concentrations. Because competitor proteins are scarce in this regime, the effect of the facilitated dissociation pathway is negligible, and its force dependence is unimportant.

We also investigate the alternative limiting case in which the force sensitivity ratio is small, so that the spontaneous pathway is most sensitive to force. Here, for low concentrations ($c = 10$ μM in simulations, red lines in Fig. 3.5C), we find pure slip-bond kinetics due to the force dependence of the partial unbinding transition. This is expected because there are very few proteins to facilitate the dissociation of the initially bound proteins, so variations in competitor binding rates contribute negligibly to the total dissociation rate. Moreover, because $x_{\rm F,P}$ is larger in this scenario, the slip regime can be observed in the simulations for small c (Fig. 3.5C and G). For sufficiently high concentrations (> 500 μM), we see delayed catch bonds. With these high competitor concentrations (blue and purple lines in Fig. 3.5C), proteins can easily dissociate via the facilitated pathway due to the frequency with which competitor proteins attempt to invade the DNA binding site. While force-induced inhibition of competitor binding is outweighed by force-enhanced partial dissociation pathway at low forces, for large forces, competitor proteins are strongly inhibited from binding. This shuts off a major dissociation pathway, which leads to the emergence of catch-bond behavior.

The numerical calculations with low sensitivity ratio, shown in panels D and H in Fig. 3.5, also reveal a change from slip-bond dissociation at low concentrations to delayed-catch-bond kinetics at high concentrations. Additionally, in the theoretical model, we clearly observe the high-force convergence of the off rates at different concentrations (Fig. 3.5D), which is only hinted at by the simulation data (Fig. 3.5C). This convergence occurs because the facilitated dissociation pathway is completely suppressed by large forces, and thus concentration does not regulate the off rate in the high-force regime.

These results indicate the fundamental role that competitor protein (or biomolecule) concentration plays in regulating force-dependent unbinding kinetics. Concentration sets the overall magnitude of the facilitated dissociation effect and is thus an essential ingredient of the catch bond exhibited by the model.

3.4 Discussion

We investigated the effect of a several key physical variables on force-dependent facilitated dissociation of proteins from DNA using both simulation and theory. With two force-dependent pathways for protein dissociation – spontaneous and facilitated – we observe three qualitatively distinct types of unbinding kinetics. Generically, catch bonds are observed when the facilitated pathway is strongly inhibited by applied force. Force suppresses competitor binding to DNA, which impedes the facilitated dissociation pathway (Fig. 3.2C and D). Slip-bond behavior, in contrast, is observed in cases in which the spontaneous pathway is more sensitive to force, so the complex exhibits canonical force-dependent dissociation kinetics (*e.g.*, Fig. 3.2A and B). Between these limiting scenarios, the force dependencies of the two pathways compete with each other. Here, we may observe delayed catch bonds, in which $\tilde{k}_{\text{off}}$ as a function of f initially increases, then decreases, and finally increases once again (Fig. 3.3A and B). More generally, the observable types of force-dependent dissociation kinetics depend on details of the system of interest. In particular, other rates in the process shown in Fig. 3.1 could depend on force, which could expand the range of dissociation behaviors considerably. Beyond the force sensitivities, we have found that several other factors – both intrinsic and extrinsic – regulate force-dependent dissociation kinetics of multivalent DNA-binding proteins (Figs. 3.4 and 3.5). Below, we discuss these factors, experimental evidence and tests for force-dependent facilitated dissociation, and the possible physiological relevance of our results.

3.4.1 Multivalent Proteins Can Form Catch Bonds via Extrinsic Factors

We have found the surprising behavior that protein-DNA complexes dissociating due to competition with other proteins in solution may dissociate more slowly when subjected to force. Thus, these complexes form "catch bonds," with force-dependent kinetics qualitatively similar to that of other proteins and complexes, including cell adhesion proteins and molecular motors [209, 210, 216, 218, 219, 221–224]. However, the catch bond we observe in this protein-DNA system differs from other complexes that are known to exhibit catch-bond behavior. Many catch bonds occur due to intrinsic factors, such as conformational changes within the protein-ligand complex, as is the case with the bacterial adhesion protein FimH [215, 219]. With facilitated dissociation, the observed catch bond is due to force-inhibited binding of a third competitor molecule, while the original protein-DNA complex in the absence of these competitor molecules actually demonstrates the classical slip-bond kinetics. Thus, whereas the force-induced affinity change in FimH is *intrinsic* to the molecular structure of the bond, the DNA-binding proteins that we consider undergo *extrinsic*, force-induced affinity changes due to the binding kinetics of competitor molecules. This extrinsic mechanism results in a similar two-pathway picture for protein dissociation, but it is regulated by a much broader collection of physical variables.

Among these variables, the competitor protein concentration, an extrinsic factor, is essential to drive facilitated dissociation; thus, it necessarily determines the nature of the overall force-dependent kinetics that we observe (Fig. 3.5). Low concentrations generally lead to only slip-bond kinetics due to the limited role of the facilitated dissociation pathway. As concentration is increased, if both the spontaneous and facilitated pathways are sensitive to force, we observe a transition from a slip bond to a delayed catch bond because the facilitated and spontaneous dissociation pathways compete. When the spontaneous pathway has a very weak force dependence or the facilitated pathway has a very strong force dependence, we may observe only catch bonds.

3.4.2 The Shape of the Binding Interface Couples to Force-Dependent Dissociation Kinetics

The preferred binding geometry of the protein on DNA, and thus the local geometry of the binding site is an important intrinsic factor that governs protein dissociation. The binding geometry is governed by two types of parameter in our model, the equilibrium bending angles, $\theta_{0,\mathrm{F}}$ and $\theta_{0,\mathrm{S}}$, and the force sensitivities, $x_{\mathrm{F,P}}$ and $x_{\mathrm{P,S}}$ (Figs. 3.2 and 3.4).

The force sensitivities, which directly govern dissociation kinetics, implicitly describe the geometry of the protein-DNA complex. We interpret the force sensitivities as dictating the degree to which a bound protein deforms when the DNA substrate is bent away from the equilibrium binding angle. For large force sensitivities, the protein (and/or the DNA binding site) is stiff. With a high force sensitivity for the partial unbinding transition (governed by $x_{\mathrm{F,P}}$ in Eq. 3.7), the protein is not strongly distorted as DNA is straightened by applied force. As a result, the energy barrier for partial unbinding decreases, so the protein-DNA bond weakens and the corresponding transition rate, $k_{\mathrm{F,P}}$, increases. Similarly, the force sensitivity $x_{\mathrm{P,S}}$ that can inhibit competitor binding describes the degree to which a protein (and binding site) may deform in order to saturate a partially bound binding site. When this sensitivity is high, the protein is stiff and difficult to deform into a conformation that can bind a straightened segment of DNA. Thus, together, these force sensitivities implicitly describe conformational changes that are possible for the protein and corresponding DNA binding site.

The preferred angle for protein-DNA binding explicitly incorporates geometric factors into the model. In the model, the equilibrium bending angle directly controls how strongly the force sensitivity couples to the transition energy barriers, so geometry alters the overall force dependence in a manner similar to that of the sensitivity ratio. Larger equilibrium bends in the DNA (governed by $\theta_{0,\mathrm{F}}$ and $\theta_{0,\mathrm{S}}$ in Eq. 3.3) make both the facilitated and spontaneous pathways more sensitive to force (Eqs. 3.6 and 3.7). In turn, as both pathways become more sensitive to force, the crossover between the catch and slip bond kinetic regimes narrows, and each regime is expanded (Fig. 3.4). Because the force dependencies become so extreme, the system inevitably falls into one of the two limiting scenarios due to the imbalance in the force dependencies of the partial dissociation and competitor binding rates ($k_{\mathrm{F,P}}$ and $k_{\mathrm{P,S}}$, respectively).

For more complicated binding geometries, we expect correspondingly more complicated force-dependent dissociation rates. For instance, we included only two force-dependent steps out of the possible six in the four-state model. Including additional force dependencies, even in steps that are not associated with a geometric change, could significantly alter the dissociation kinetics. Each dissociation pathway (facilitated and spontaneous) would then have multiple cooperating or competing force-dependent steps, which would lead to a more diverse set of dissociation behaviors. Moreover, the functional forms of the force dependencies may govern the observed dissociation kinetics. Consequently, we anticipate that in biological manifestations of protein-DNA facilitated dissociation, the force-dependent kinetics will depend on structural properties of the protein and the local DNA/chromatin environment. Indeed, it has been observed that the dissociation rates of the transcriptional regulators CueR and ZntR in bacteria are sensitive to local chromatin conformation [55]. Thus, while our simple four-state model illustrates the general phenomenology of force-dependent facilitated dissociation, forces may differentially govern kinetics through several biophysical mechanisms.

Intriguingly, these force-dependent kinetics may feedback into the local structure of the DNA substrate. Even at zero force, facilitated dissociation has been shown to regulate the conformation of stretched and twisted DNA [227]. Thus, further studies of DNA interacting with proteins with force-dependent facilitated dissociation kinetics could lead to novel insights into the structure and dynamics of protein-bound DNA and chromatin.

3.4.3 Single-Molecule Experiments to Test the Model

The force-dependent facilitated dissociation kinetics predicted in this work could be observed using established experimental setups. In particular, we propose that the *in vitro* single-molecule experiments that mirrors our model (Fig. 3.1B) would be able to measure the force dependence of facilitated dissociation. In these experiments, DNA is tethered to a surface at one end and a bead at the other (Fig. 3.1B). The bead is manipulated via optical or magnetic tweezers (*e.g.*, [39, 67, 68, 99, 100, 103, 228, 229]), which can exert $\sim 0.1 - 10$ pN tensile forces on the tethered DNA.

To measure dissociation rates, protein initially bound to DNA should be fluorescently labeled, as in previous experiments studying facilitated dissociation of the bacterial nucleoidassociating protein FIS [99]. Non-fluorescing competitor proteins may be flowed in so that as competitors from solution exchange with the initially bound fluorescent proteins, the tethered DNA strand becomes darker. Using an approach with distinguishable sets of protein is essential because simply measuring the number of bound proteins is insufficient to determine the dissociation rate because proteins may exchange, *i.e.*, when a protein vacates a DNA binding site, the binding site may nonetheless remain occupied by the competitor protein [55, 105, 150, 177]. However, with one species of "light" protein and one species of "dark" (competitor) protein, dissociation rates can be measured by observing the decay of the fluorescence signal along the tethered DNA. This experiment can probe kinetics at various tensile forces and competitor concentrations, and other physical variables, such as ionic concentration, can be varied to tune transition energy barriers [67, 104, 105, 231] or preferred binding geometry [228].

A variation of this experiment with single-stranded DNA binding protein (SSB) suggests that facilitated dissociation can lead to catch-bond-like force-dependent kinetics [232]. In this experiment, dissociation of SSB from its binding site is facilitated by "intersegment transfer," *i.e.*, DNA segments from the same DNA strand compete with binding by the protein to the initial binding site and eventually strip it from the binding site. In these experiments, force on the DNA suppresses the interaction of these distant DNA segments because DNA looping is inhibited by tension. Thus, force suppresses facilitated dissociation in this experiment, which is precisely what is required for the catch bond effect.

3.4.4 Relevance to *in vivo* Protein Kinetics and Function

Functionally, many catch bonds are complexes that must bear forces, such as adhesion proteins and molecular motors [209, 210, 216, 218, 219, 221–224]. Indeed, some proteins that undergo facilitated dissociation are architectural proteins, such as the bacterial protein FIS which can DNA stabilize loops against applied forces [68, 233]. In addition, several recent studies, suggest that facilitated dissociation may have important regulatory effects in living cells [55, 104, 177, 187, 234, 235]. Our model suggests that these facilitated dissociation kinetics may be modulated by mechanical stresses transmitted through DNA/chromatin, and more generally, the local conformation of the genome.

Our main prediction is that forces can inhibit the dissociation of a DNA-bound protein by inhibiting competitor-mediated dissociation and exchange with biomolecules from the surrounding environment. It has previously been suggested that cells may utilize facilitated dissociation to efficiently regulate transcription through modulation of transcription factor binding and unbinding kinetics [55, 177, 234, 235]. Our results suggest that large mechanical stresses within the genome would locally inhibit facilitated unbinding kinetics. Thus, transcriptional regulation by facilitated dissociation could be specifically targeted to mechanically relaxed regions of the genome.

It has also been shown that competitor DNA strands can facilitate protein dissociation by effectively stripping partially bound proteins from the protein-bound DNA [68, 100]. For this process, competitor binding (P to S in Fig. 3.1A) should depend far less sensitively on the conformation of protein-bound DNA because competitor DNA binds the partially bound protein. Instead, competitor binding should depend on the conformation of and tension within the competitor DNA molecule. In contrast to the case of competitor-protein-mediated dissociation described above, this process should favor protein transfer to DNA segments with lower mechanical stress. This may be relevant, for instance, during transcription, in which RNA polymerase may exert > 10 pN forces [201]. There, it has been observed that nucleosomes initially proximal to the translocating polymerase are ejected, and subsequently found on nearby strands of DNA [236–240]. This may be a prototypical example of force-dependent facilitated dissociation mediated by competitor DNA.

Force-dependent facilitated dissociation by competitor DNA may also regulate diffusive searches for target sites. For example, recent theoretical work suggests that protein target searches may be governed by the local chromatin conformation [241]. Again, the force dependence of protein dissociation may either assist proteins searching for mechanically relaxed regions of chromatin or inhibit intersegment transfer as observed *in vitro* [232].

More generally, our work illustrates how mechanical forces may regulate facilitated protein-DNA dissociation. We anticipate that a wide variety of multivalent proteins may be subjected to these non-canonical, extrinsically regulated kinetics *in vivo*.

Chapter 4

Force-extension behavior of DNA in the presence of DNA-bending nucleoid associated proteins[i]

4.1 Introduction

The genomic material in a prokaryotic cell is contained within the cellular structure known as the nucleoid, composed of DNA and nucleoid associated proteins (NAPs). NAPs act as architectural proteins by helping organize the overall nucleoid structure [32–34, 37, 38, 242, 243]. These proteins bind non-specifically to the DNA and can alter the local structure. For example, the NAP HU can form weakly bent hairpin turns or stiffen straight DNA, while NAPs IHF and FIS can form stiff local bends [37, 68, 108, 139]. These small changes in local structure have effects at longer length scales, which play a role in nucleoid organization [54, 242, 244]. In addition to the direct architectural role these proteins play, they also indirectly play a role in several biological functions, such as DNA replication, transcription, and gene expression [32, 38, 47, 48, 51, 52, 54, 72].

Many of these biological processes can exert forces on the DNA, such as the forces stemming from DNA and RNA polymerases [200, 202, 203]. These pN scale forces can affect how proteins interact with the DNA, especially those that bind weakly such as NAPs. Single molecule studies can give us information about how forces affect the behavior of protein-DNA interactions. Studies done with NAPs such as FIS, IHF, and HU have shown a range of force and concentration dependent extension behaviors [39, 67, 68, 71, 99, 100, 102, 103, 108]. When low concentrations of these proteins are bound to the DNA, the extension at a given

---

[i] Reproduced from Dahlke, K. and C.E. Sing. 2018. Force-extension behavior of DNA in the presence of DNA-bending nucleoid associated proteins *J. Chem Phys.* 148:084902. with the permission of AIP Publishing

force decreases, indicating that these proteins are compacting the DNA [39, 67, 68, 71, 99, 100, 102, 103, 108]. However, at high concentrations of proteins, reduced compaction or even a stiffening effect can be observed [39, 67, 68, 71, 99, 100, 102, 103, 108]. The underlying mechanisms by which these behaviors occur is difficult to determine by single molecule experiments alone.

Simulations can give us insights into how the local interactions between the proteins and DNA are affecting the conformational behavior that is observed in these single molecule experiments. Previous studies have provided evidence that the NAP FIS has multiple binding states, where a protein can be partially bound or fully bound to a DNA strand [85]. Other NAPs such as HU, H-NS, and IHF, may also exhibit multiple binding states due to their dimeric nature [32, 40, 243]. These multiple bound states are thought to play a role in these different extension behaviors. Simulations allow us to directly track the states (and number) of bound proteins and how they correlate with the overall behavior of the DNA molecule.

Simulations have investigated protein-DNA interactions on a coarse grained scale. For example, Takada *et al.* have investigated the relationship between protein sliding and DNA bending using the NAP protein HU by using a three beads per nucleotide model for DNA (3SPN.2C) [116], and an atomistic interaction-based coarse grained model (AICG) for the protein [109]. They are able to look at the local, dynamic interactions between the protein and the DNA. This type of coarse grained model can be used to study other protein-DNA interactions, such as the transcription factor protein p53 [245–247], zinc finger proteins [248], and nucleosomes [249–251], but this level of coarse-graining cannot be extended past systems on the order of 1 μm [116]. There are also highly coarse-grained protein-DNA models, where there are multiple base pairs per DNA bead, and a protein is modeled with just a few particles [110, 252–255]. Many of these large-scale models are capable of reaching lengths on the order of nucleoid ($\sim$ mm), but the interactions between the DNA and protein are often phenomenologically motivated [110]. We want to create a model that is capable of capturing the equilibrium and dynamic behavior of NAP/DNA interactions that is built on physically motivated local interactions.

This work investigates the force-extension behavior of DNA as a function of concentration of FIS, whose binding behavior has been well-characterized [42, 46, 53, 57, 69, 99, 141, 154]. By controlling the dependence of FIS's binding affinity on the local shape of the DNA, we can demonstrate changes in the number of proteins bound as a function of force. The different local deformations that are based on FIS's bound state are the main drivers of the different force-extension behaviors. Our model allows us to look at the behavior of FIS/DNA interactions as the DNA strand is being pulled out of equilibrium.

4.2 Materials and Methods

We aim to create a simulation model that allows us to not only study NAP/DNA interactions at equilibrium, but also investigate their dynamics. In order to achieve this, we model single molecule systems of interest with a coarse-grained Brownian Dynamics (BD) simulation. A strand of dsDNA is represented by a chain of $N = 100$ beads of radius $a = 4$ nm, resulting in a simulated strand that corresponds to approximately 2350 base pairs, shown in Fig. 4.1A. The size of the bead is chosen to correspond to the approximate size of a binding site of a FIS protein [46, 100, 141]. One end of the DNA strand is tethered, and the other end of the DNA strand is constricted to movement only along the x-axis. Distance, energy, and time in the system are non-dimensionalized by the radius of a bead a ($\tilde{r}_{ij} = r_{ij}/a$), k_BT ($\tilde{U} = U/k_BT$), and the diffusion time of a single particle $\tau_D = 6\pi\eta a^3/(k_BT)$ ($\tilde{t} = t/\tau_D$), respectively. Normalized (and dimensionless) values are denoted by a tilde.

The DNA strand can interact with a concentration field of implicit proteins. Each DNA bead can be in one of four bound states: no protein bound (unbound, or U), a protein fully bound (F), a protein partially bound (leaving one site per DNA bead open, or P), or a saturated bead with two proteins partially bound to it, (S). A representative schematic can be seen in Fig. 4.1B. This simplified four state model is motivated by previous simulations

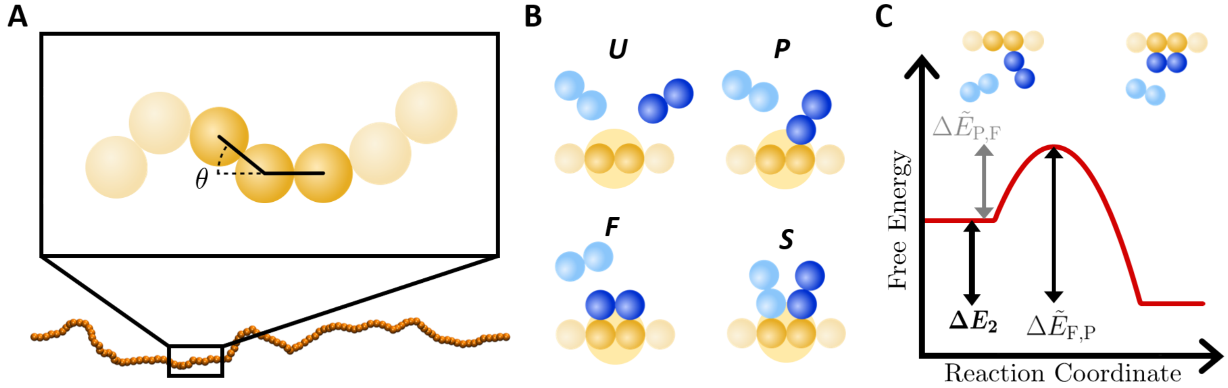

Figure 4.1: **A**. A snapshot of the tethered DNA strand from a simulation with the bending angle θ shown in the inset. **B**. Schematic of the four different coarse-grained DNA states. The small gold beads represent DNA binding sites, and the large yellow circle represents a single simulated DNA bead. Blue dimers represent protein dimers. **C**. An example energy landscape of the binding/unbinding model of the partially bound and fully bound states. Each ΔE is a function of θ, described by Eqs. 4.1 and 4.2.

[85, 106, 199] and experiments [99, 100, 105]. Movement between two states, A and B, is controlled by binding and unbinding energy barriers, $\Delta\tilde{E}_{\mathrm{a},b}$. We use arbitrary energy barriers that result in simulated binding kinetics that are much faster than experimentally measured values in order to make our simulations computationally tractable [100]. An example set of energy barriers for movement between states P and F are shown in Fig. 4.1C.

Force dependent binding and unbinding behavior has been experimentally observed [67, 103]. We incorporate this into our model by accounting for the energy penalty and force required to bend the DNA into a new equilibrium position. Bare DNA (with no bound proteins) has an equilibrium angle of $\theta_{0,\mathrm{U}} = 0.0$. Motivated by the DNA bending induced by the fully bound NAP FIS, we choose $\theta_{0,\mathrm{F}} = \pi/3$ [44–46, 139, 154]. $\theta_{0,\mathrm{S}} = \pi/6$ and $\theta_{0,\mathrm{P}} = 0.0$ are parameterized to qualitatively match the force versus DNA extension curves seen experimentally [68, 100].

The energy barrier for binding events (moving from U to P, from P to F, and from P to

S) has the following form:

$$\Delta\tilde{E}_{a,b} = \Delta\tilde{E}_B^* + \delta_{b,F}\tilde{\sigma} + \frac{\tilde{\kappa}_B}{2}\left(\theta - \theta_{0,b}\right)^2 \tag{4.1}$$

where $\Delta\tilde{E}_B^* = 3.0$ is the constant binding energy, and $\delta_{a,F}\tilde{\sigma} = 2.0$ is the entropic loss associated with moving from the singly bound state to the fully bound state. The last term is included in order to cause binding events to be more likely when the DNA strand is in a preferential conformation ($\theta_{0,b}$). This is not a direct effect of the applied force, since the force applied to DNA cannot affect a protein until it is bound. Force instead biases DNA into states that are far from ideal binding configurations, leading to an indirect effect on binding likelihood.

The force-dependent energy barrier for unbinding events (movement from P to U, from F to P, and from S to P) has the following form:

$$\Delta\tilde{E}_{b,a} = \Delta\tilde{E}_{\mathrm{UB,a}}^* + \lambda[\tilde{\kappa}_B\left(\theta - \theta_{0,b}\right)] \tag{4.2}$$

where $\Delta\tilde{E}_{\mathrm{UB,a}}^*$ are the constant unbinding energies associated with changing the bound state. These values are set to $\Delta\tilde{E}_{\mathrm{UB,F}}^* = 10.0$ and $\Delta\tilde{E}_{\mathrm{UB,P}}^* = \Delta\tilde{E}_{\mathrm{UB,S}}^* = 12.0$. The last term is associated with the change in energy landscape due to the bending force, which is related to the force applied to the DNA strand. $\lambda = 0.7$ is the strength of this force dependence, and is chosen to see a measurable change in binding behavior in our simulations.

When the DNA strand is being pulled by a low force, there are more local bends in the strand (higher average θ). This leads to a decrease in the binding energy barriers (last term in Eq. 4.1) and an increase in the unbinding energy barriers (last term in Eq. 4.2), making it easier for a protein to move from an unbound state to a bound state. Alternatively, at high force, there are fewer local bends in the DNA strand (lower average θ), which corresponds to an increase in binding energies and decrease in unbinding energies. Proteins therefore have an easier time moving from a bound state to an unbound state at high force.

A Monte Carlo type update of each DNA bead's bound state, denoted by Ω_i, occurs every $\tilde{\tau}_{MC} = 0.05$. This update time step is chosen to match the average constant binding time, τ_B, to the diffusion time, τ_D of a single bead, given that a protein is in a position to bind, which is dependent on concentration. This update also shows the statistical results of a Bell Model type reaction [152]. A random number ζ is generated, and the binding update occurs as follows:

$$\Omega_i(t) = \begin{cases} \begin{cases} \text{P if } \zeta < \gamma e^{-\Delta E_{\text{U,P}}} \\ \text{U if } \zeta > \gamma e^{-\Delta E_{\text{U,P}}} \end{cases} & \text{if } \Omega_i(\tilde{t} - \tilde{\tau}_0) = \text{U} \\ \begin{cases} \text{F if } \zeta < e^{-\Delta E_{\text{P,F}}} \\ \text{P if } \zeta > e^{-\Delta E_{\text{P,F}}} \end{cases} & \text{if } \Omega_i(\tilde{t} - \tilde{\tau}_0) = \text{P} \\ \begin{cases} \text{P if } \zeta < e^{-\Delta E_{\text{F,P}}} \\ \text{F if } \zeta > e^{-\Delta E_{\text{F,P}}} \end{cases} & \text{if } \Omega_i(\tilde{t} - \tilde{\tau}_0) = \text{F} \\ \begin{cases} \text{U if } \zeta < e^{-\Delta E_{\text{P,U}}} \\ \text{P if } \zeta > e^{-\Delta E_{\text{P,U}}} \end{cases} & \text{if } \Omega_i(\tilde{t} - \tilde{\tau}_0) = \text{P} \\ \begin{cases} \text{S if } \zeta < \gamma e^{-\Delta E_{\text{P,S}}} \\ \text{P if } \zeta > \gamma e^{-\Delta E_{\text{P,S}}} \end{cases} & \text{if } \Omega_i(\tilde{t} - \tilde{\tau}_0) = \text{P} \\ \begin{cases} \text{P if } \zeta < e^{-\Delta E_{\text{S,P}}} \\ \text{S if } \zeta > e^{-\Delta E_{\text{S,P}}} \end{cases} & \text{if } \Omega_i(\tilde{t} - \tilde{\tau}_0) = \text{S} \end{cases} \tag{4.3}$$

The γ coefficient corresponds to the concentration dependence of binding. We impose a chemical potential on our system, $\mu = \mu_o + \ln(c)$, where c is the concentration of the protein in μM and γ takes the form $\gamma = e^{-\mu} = e^{-\mu_0}c$. This impacts the probability that the DNA bead will move from the unbound state to the P (or S) state. The values of γ were found by matching to simulations done with explicit, freely-diffusing proteins, which indicated that $\mu_0 = 1.7$ μM.

The movement of each DNA bead i is governed by the Langevin equation,

$$\frac{\partial \mathbf{r}_i}{\partial t} = -\sum_{j}^{N_{total}} \mu_{\mathbf{ij}} \cdot \nabla_j U(t) + \xi_i \tag{4.4}$$

where $\mathbf{r_i}$ is the position of bead i, $\mu_{\mathbf{ij}} = \delta_{ij}\boldsymbol{\delta}/(6\pi\eta a)$ is the freely-draining Stokes mobility matrix, η is the solvent viscosity, δ is the identity matrix, δ_{ij} is the Kronecker delta, and ξ_i is a random velocity that satisfies the fluctuation dissipation theorem, $\langle \xi_i \xi_j \rangle = 2k_B T \mu_{ij} \delta_{ij}$.

U is the sum of the potential energies of the system: stretching (U_S), excluded volume (U_{LJ}), and bending (U_B). DNA beads are connected by Hookean springs, which gives the equation

$$\tilde{U}_S = \frac{\tilde{\kappa}_S}{2} \sum_{i,i+1} (\tilde{b} - \tilde{b}_0)^2 \tag{4.5}$$

where $\tilde{b}$ is the distance between adjacent beads i and j, and $\tilde{b}_0 = 2.0$ is the equilibrium distance between two beads. $\tilde{\kappa}_S$ is set to an arbitrary value of 200.0, to ensure that deviations from $\tilde{b}_0$ are small.

The excluded volume potential is of the shifted Lennard-Jones form

$$\begin{cases} \tilde{U}_{LJ} = \tilde{\epsilon} \sum_{ij} \left[\left(\frac{\tilde{b}_0}{\tilde{r}_{ij}} \right)^{12} - 2 \left(\frac{\tilde{b}_0}{\tilde{r}_{ij}} \right)^{6} + 1 \right] & \tilde{r}_{ij} \leq r_c \\ 0 & \tilde{r}_{ij} > r_c \end{cases} \tag{4.6}$$

where $\tilde{\epsilon} = 0.41$ controls the magnitude of the potential, and $\tilde{b}_0 = 2.0$ is where the potential is at its minimum. A cutoff of $\tilde{r}_c = 5.0$ is chosen due to the negligible forces at distances greater than 5.0a. Repulsive beads placed at the midpoint of the bond vectors also interact with this potential at a cutoff of $\tilde{r}_c = 2.0$ (to include only the repulsive portion of this potential), which is needed to prevent the DNA strand from crossing.

The bending potential is included to maintain the appropriate stiffness of DNA

$$\tilde{U}_B = \frac{\tilde{\kappa}_B}{2} \sum_{i=1}^{m-1} (\theta_i - \theta_0(\Omega_i))^2 \tag{4.7}$$

where $\tilde{\kappa}_B = 6.25$ is chosen to correspond to a DNA persistence length of 50 nm, and θ_i is the angle between bonds of beads $i-1$ and i, and i and $i+1$. $\theta_0(\Omega_i)$ is the equilibrium angle of the DNA bead in its bound state Ω.

A summarized list of simulation parameters can be found in Table 4.1, grouped into four rows. Row 1 contains parameters defining the simulated DNA strand, corresponding to a

DNA strand of length 800 nm. Row 2 contains parameters defining the equilibrium angle of DNA in a given bound state used in Eqs. 4.1, 4.2, and 4.7. Row 3 contains the energy barrier values used in Eqs. 4.1 and 4.2 and other binding parameters, all of which are chosen for computational convenience. Row 4 contains parameters used in the potential energies of the system (Eqs. 4.5-4.7).

Table 4.1: Summary of parameters used in the simulation. Tildes denote normalized values.

Simulation parameters	
$N = 100$	$a = 4$ nm
$\theta_{0,U} = 0$	$\theta_{0,F} = \pi/3$
$\theta_{0,P} = 0$	$\theta_{0,P} = \pi/6$
$\Delta\tilde{E}^*_B = 3.0$	$\Delta\tilde{E}^*_{\mathrm{UB,P}} = 12.0$
$\Delta\tilde{E}^*_{\mathrm{UB,F}} = 10.0$	$\Delta\tilde{E}^*_{\mathrm{UB,S}} = 12.0$
$\lambda = 0.7$	$\tilde{\tau}_{MC} = 0.05$
$\tilde{b}_0 = 2.0$	$\tilde{\epsilon} = 0.41$
$\tilde{\kappa}_S = 200.0$	$\tilde{\kappa}_B = 6.25$

4.3 Results and Discussion

4.3.1 Binding Equilibrium

To verify that our 4-state model captures the appropriate binding behavior, we compare the expected binding equilibrium results from statistical mechanics to those obtained from our simulations. These simulations can also show us the effect of force on the number of NAPs bound to DNA. Similar measurements can be calculated from experimental force versus extension curves [103]. Simulations allow us to measure the number of DNA beads in a bound state directly, and they also allow us to measure the number DNA sites in a specific state. At low forces, there is a large change in energy between the partially and fully bound states, $\Delta\tilde{E}_2 = \Delta\tilde{E}_{\mathrm{P,F}} - \Delta\tilde{E}_{\mathrm{F,P}}$ (and similarly between the partially bound and saturated states, $\Delta\tilde{E}_3 = \Delta\tilde{E}_{\mathrm{P,S}} - \Delta\tilde{E}_{\mathrm{S,P}}$). This is due to the higher values of the unbinding energies ($\Delta\tilde{E}_{\mathrm{F,P}}$ and $\Delta\tilde{E}_{\mathrm{S,P}}$) and lower values of the binding energies ($\Delta\tilde{E}_{\mathrm{P,F}}$ and $\Delta\tilde{E}_{\mathrm{P,S}}$). Force thus

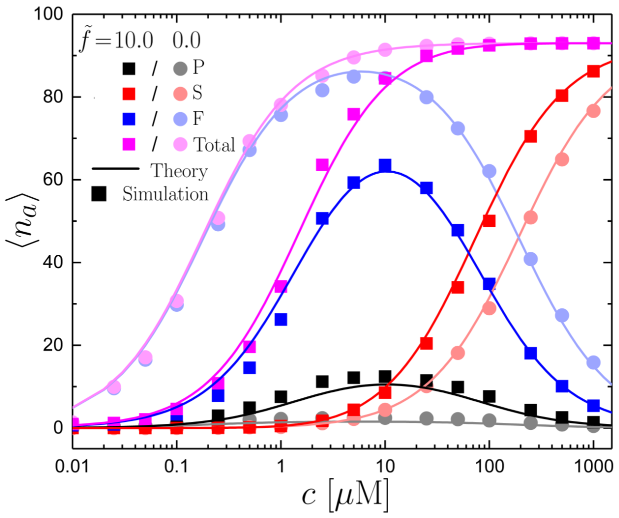

Figure 4.2: The number of DNA beads in each bound state at a force of 10.0 pN (darker lines and square data points) and 0.0 pN (lighter lines and circle data points). The data points correspond to simulation data, and lines are calculated from Eq. 4.8.

drives the system away from both the fully bound and saturated states towards the partially bound state.

We observe the result of these force-dependent transitions in the binding behavior of our model NAP. The changes in $\Delta\tilde{E}_2$ and $\Delta\tilde{E}_3$, caused by the force exerted on the DNA molecule, change the number of proteins bound at equilibrium, shown by the data points for forces of 0.0 pN and 10.0 pN in Fig. 4.2. At high forces, there are fewer total proteins bound because there is a lower change in energy between states. If we look at the differences between the different bound states (P, F, and S), we see that at high forces, there is an increase in the number of DNA sites in the partially bound state compared to the low force value. This can be explained by the increase in energy required to move from the partially bound to fully bound state ($\Delta\tilde{E}_{\mathrm{P,F}}$), leading to more proteins staying in the partially bound state. The differences in the fully bound state behavior at low and high forces is again described by the changes in $\Delta\tilde{E}_{\mathrm{P,F}}$ and $\Delta\tilde{E}_{\mathrm{F,P}}$. At high forces, there is an overall lower $\Delta\tilde{E}$ between unbound and fully bound states, leading to fewer proteins fully bound to the DNA strand. The saturated state is the state most dependent on the concentration of proteins in the system, and we start to see the force effects at high concentration. We see fewer DNA sites in the saturated states at lower force due to the high number of DNA sites in the fully bound state. At higher forces, there are fewer DNA beads in the fully bound state, which allows the DNA to become oversaturated with partially bound proteins (beads are in the S state).

We compare the values from our simulation to the value predicted by statistical mechanics:

$$\langle n_p \rangle = k_B T \frac{\partial \ln \Xi}{\partial \mu} \tag{4.8}$$

where n_p is the number of bound proteins. Ξ is the grand partition function of our system:

$$\Xi = \left[e^{(\Delta \tilde{E}_1 + \tilde{\mu})} + e^{(\Delta \tilde{E}_1 + \Delta \tilde{E}_3 + 2\tilde{\mu})} + e^{(\Delta \tilde{E}_1 + \Delta \tilde{E}_2 + \tilde{\mu}}) + 1 \right]^N \tag{4.9}$$

Substituting this expression into Eq. 4.8, we get

$$\langle n_p \rangle = N \frac{e^{\Delta \tilde{E}_1 + \tilde{\mu}} + 2e^{(\Delta \tilde{E}_1 + \Delta \tilde{E}_3 + 2\tilde{\mu})} + e^{\Delta \tilde{E}_1 + \Delta \tilde{E}_2 + \tilde{\mu}}}{e^{\Delta \tilde{E}_1 + \tilde{\mu}} + e^{(\Delta \tilde{E}_1 + \Delta \tilde{E}_3 + 2\tilde{\mu})} + e^{\Delta \tilde{E}_1 + \Delta \tilde{E}_2 + + \tilde{\mu}} + 1} \tag{4.10}$$

for the average total number of NAPs bound to DNA. We can also modify Eq. 4.10 to calculate the number of DNA beads in each state by doing the derivative of Ξ with respect to an arbitrary μ_a, which will give us the number of DNA beads in state a. The predicted values for $\langle n_a \rangle$ are plotted as lines in Fig. 4.2, and demonstrate quantitative matching with simulations (points).

4.3.2 Force-Extension at Equilibrium

Elasticity behavior of a strand of DNA, such as extension (z) as a function of force (f), can be dependent on the number of proteins bound to it (which depends on the concentration of proteins, c) [39, 67, 68, 71, 100, 102, 103, 108]. Fig. 4.3A shows the simulated force versus extension behavior obtained by exerting a constant force on the DNA strand and measuring

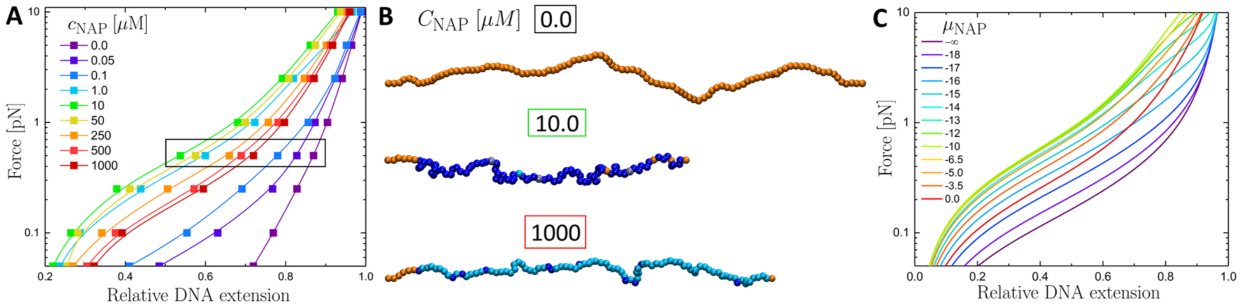

Figure 4.3: **A**. Force versus extension behavior as a function of NAP concentration. The extension of a DNA molecule decreases as concentration is increased to 10.0 μM, but begins to re-extend as protein concentration is increased to 1000 μM as the DNA strand becomes saturated with proteins. Data points are from simulations, and the lines are provided to guide the eye. **B**. Simulation snapshots of the DNA at different protein concentrations. Orange beads represent unbound DNA beads, gray beads are partially bound DNA beads, dark blue beads are fully bound DNA, and cyan beads are saturated DNA beads. **C**. Theoretical concentration dependent force-extension behavior from Eq. 4.16.

the extension of the chain at equilibrium. From $c = 0$ μM to $c = 10.0$ μM, extension decreases at a given force as more proteins are added. This is due to the increase in number of DNA sites that are in a fully bound state and the local bending that occurs at each of these sites. At $c = 10.0$ μM, the DNA strand is nearly "saturated" with fully bound sites (see Fig. 4.3B), leading to a high number of sites with the highest degree of local bending. When the concentration of proteins increases past $c = 10.0$ μM, more proteins bind to the DNA, which start to displace some of the fully bound states with saturated states and above $c = 1000$ μM, the DNA is "saturated" with two proteins bound per DNA site (S) (see Fig. 4.3B). The DNA sites in this state have a higher degree of bending than bare DNA, but less than the DNA saturated with fully bound sites.

We adapt a theory developed in the literature to describe the force-extension behavior of DNA that can undergo local bending when proteins are bound to it [66, 256–258]. The model is based on a semi-flexible polymer composed of discrete segments, each of which can adapt a bent conformation at equilibrium when a protein is bound. We expand this model to account for the multiple binding modes in our model. The energy of a strand is

$$
\begin{aligned}
\tilde{E} = \sum_{i=1}^{N} \Big[& -bfu_i \cdot \hat{x} + \frac{\kappa_B}{2} \left(\operatorname{acos}(u_i \cdot u_{i+1}) \right) \delta_{iU} \\
& + \left\{ \frac{\kappa_B}{2} \left(\operatorname{acos}(u_i \cdot u_{i+1}) - \theta_S \right) - E_1 - \mu \right\} \delta_{iP} \\
& + \left\{ \frac{\kappa_B}{2} \left(\operatorname{acos}(u_i \cdot u_{i+1}) - \theta_S \right) - E_1 - E_3 - 2\mu \right\} \delta_{iS} \\
& + \left\{ \frac{\kappa_B}{2} \left(\operatorname{acos}(u_i \cdot u_{i+1}) - \theta_F \right) - E_1 - E_2 - \mu \right\} \delta_{iF} \Big]
\end{aligned}
\tag{4.11}
$$

where b is the length of a segment, f is the force, $\hat{x}$ is a unit vector in the direction of the force, u_i are the normalized bond vectors, θ_a are the equilibrium bending angles for the binding state, and μ is the chemical potential.

To get the force extension behavior, we numerically solve the partition function using a transfer matrix formalism. We use a discretized set of $t = 1000$ possible bond vectors (u_i) that are uniformly distributed along the surface of a unit sphere. We consider a $4t$-component vector $\boldsymbol{\psi}_i$, with each component representing the partition function where the i-th monomer has a given unit vector u_i and state Ω_i. This vector $\boldsymbol{\psi}_i$ can be related to the vector $\boldsymbol{\psi}_{i+1}$ describing a chain with $i+1$ monomers via a $4t \times 4t$ transfer matrix, $\mathbf{T} = (u_{i+1}, \Omega_{i+1} | u_i, \Omega_i)$. This matrix is composed of the Boltzmann factors that incorporate the $i+1$-th monomer contributions into the i-monomer partition function, with this new monomer u_{i+1} in the unbound ($\Omega = U$), partially bound ($\Omega = P$), saturated ($\Omega = S$), or fully bound ($\Omega = F$) states, given that the i-th monomer had a segment u_i in a state Ω:

$$
\mathbf{T}(u_{i+1}, U | u_i, \Omega_i) = \exp\left[-\left(\frac{\tilde{\kappa}_B}{2} \right) \left(\operatorname{acos}(u_i \cdot u_{i+1}) \right) + \tilde{b}\tilde{f} u_{i+1} \cdot \hat{x} \right] \tag{4.12}
$$

$$
\mathbf{T}(u_{i+1}, P | u_i, \Omega_i) = \exp\left[-\left(\frac{\tilde{\kappa}_B}{2} \right) \left(\operatorname{acos}(u_i \cdot u_{i+1} - \theta_S) + \tilde{E}_1 + \tilde{\mu} \right) + \tilde{b}\tilde{f} u_{i+1} \cdot \hat{x} \right] \tag{4.13}
$$

$$\mathbf{T}(u_{i+1}, S|u_i, \Omega_i) = \\ \exp\left[-\left(\frac{\tilde{\kappa}_B}{2}\right)(\mathrm{acos}(u_i \cdot u_{i+1} - \theta_S) + \tilde{E}_1 + \tilde{E}_3 + 2\tilde{\mu}) + \tilde{b}\tilde{f}u_{i+1} \cdot \hat{x}\right] \tag{4.14}$$

$$\mathbf{T}(u_{i+1}, F|u_i, \Omega_i) = \\ \exp\left[-\left(\frac{\tilde{\kappa}_B}{2}\right)(\mathrm{acos}(u_i \cdot u_{i+1} - \theta_F) + \tilde{E}_1 + \tilde{E}_2 + \tilde{\mu}) + \tilde{b}\tilde{f}u_{i+1} \cdot \hat{x}\right] \tag{4.15}$$

The partition function is calculated by operating on a single-monomer vector $\boldsymbol{\psi}_0$ with $\mathbf{T}$ N-times to obtain $\boldsymbol{\psi}_N$. The components of this final $\boldsymbol{\psi}_N$ are summed to obtain the partition function $\mathcal{Z} = \mathbf{I} \cdot \boldsymbol{\psi}_N$ ($\mathbf{I}$ is a vector of 1s) for a strand of N segments. The extension of the strand (z) is calculated by taking the derivative of ($\ln \mathcal{Z}$) with respect to the force:

$$z = \frac{\partial \ln \mathcal{Z}}{Nb\partial\tilde{f}} \tag{4.16}$$

Fig. 4.3C shows the theoretical force-extension behavior as a function of chemical potential, μ. The theoretically predicted behavior is qualitatively similar to what is seen in our simulations and in previous experiments [68, 100]. The quantitative differences between the theoretical prediction and the simulation data are due to simulation parameters, such as excluded volume interactions, that cannot be included in the theoretical model.

4.3.3 Rapid Force-Extension

Our model allows us to look past this system at equilibrium, and we can anticipate the interplay of timescales as the system is driven out of equilibrium. We investigate the behavior of a DNA strand with stretching, bending, and LJ potentials as a function of pulling rate, v, and concentration, c, where each variable has associated timescales. The simulations are initiated in a fully extended state ($z = 200a$) and are slowly compressed to $z = 50a$ to allow protein binding to equilibrate. The strand is then pulled at both ends at a rate $v/2$ back to its fully extended state. 40 trajectories are averaged for each v, which range from 1.0×10^{-4}

to 1.0×10^{-1} a/τ_D (or 0.15 to 151 μm/s), and each c, ranging from 0 to 1000 μM, to obtain force and number of bound proteins as a function of extension. The system allows us to examine timescales associated with the pulling rate and FIS-DNA interactions: the time it takes a protein to go from fully bound to partially bound, $\tilde{\tau}_{\text{UB}}$, and the time it takes the DNA strand to move one bead length, or $2a$, $\tilde{\tau}_P$. The average time it takes for a protein to partially unbind (F to P) can be calculated by

$$\tilde{\tau}_{\text{UB}} = \tilde{\tau}_{MC} e^{\Delta \tilde{E}_{F,P}} \tag{4.17}$$

where $\Delta \tilde{E}_{\text{F,P}}$ is calculated from Eq. 4.2, which is dependent on force. At low extension ($\tilde{z} = 50$) where the DNA strand can adopt many conformations, the average $\Delta \tilde{E}_{F,P} \approx 9.1$, leading to an average $\tilde{\tau}_{\text{UB}} = 405$. At high extensions ($\tilde{z} = 200$), where the pulling force and bending force are strongly competing, $\Delta \tilde{E}_{F,P} \approx 7.7$, leading to an average $\tilde{\tau}_{\text{UB}} = 107$. The characteristic pulling time, $\tilde{\tau}_P = 1/v$ ranges from 10000 for $v = 1 \times 10^{-4}$ to 20 for $v = 1.0 \times 10^{-1}$. The relationship between these two timescales can be described by the dimensionless number $\Gamma = \tilde{\tau}_P/\tilde{\tau}_{\text{UB}}$.

We can measure the force as a function of extension and v, and an example force-extension curve at $c = 0.0$ μM can be seen in Fig. 4.4A. At low extension, the forces measured for the slower pulling rates ($v < 5.0 \times 10^{-3}$) are nearly identical. At higher extensions, shown in the inset to Fig. 4.4A, we see an increase in measured force, which matches for all $v < 5.0 \times 10^{-3}$. For $v > 5.0 \times 10^{-3}$, we see measurably different behavior. Instead of a constant force at low extension, we see different linear increases in the measured force. At high extension and high v, we see a similar sharp increase in force just as we did for low v. This is due to hydrodynamic drag effects, which are negligible at low v. The work dissipated due to drag can be calculated by the following integral:

$$W_D = \int_{z_i}^{z_f} dz (f_v(z) - f_{eq}(z)) \tag{4.18}$$

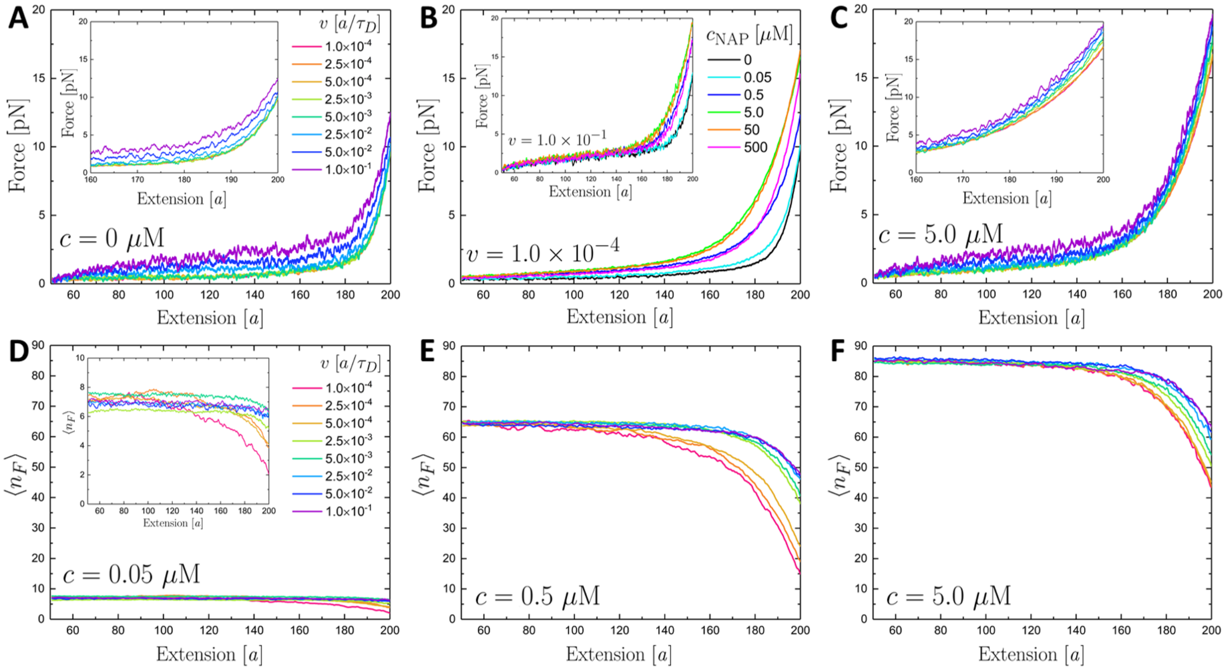

Figure 4.4: **A**. Force versus extension behavior of bare DNA ($c = 0\ \mu$M) as a function of pulling rate v. The lines are a moving average of 50 data points, where each data point is an average of the force at a given extension of 40 trajectories. The inset shows the force-extension behavior at high extension ($z \geq 160a$). **B**. Force versus extension behavior as a function of NAP concentration at $v = 1.0 \times 10^{-4}$, which we take to be the equilibrium force-extension behavior. The inset shows the force-extension behavior as a function of NAP concentration at $v = 1.0 \times 10^{-1}$. **C**. The force versus extension data at $c = 5.0\ \mu$M. We see an increase in measured force as we increase v that is not solely due to drag, especially above $z = 140a$. The inset shows force measured at high extension, where the differences in measured force at different rates is most pronounced. **D-F:** The number of DNA beads in the fully bound state as a function of extension and v at $c = 0.05\ \mu$M (D), $c = 0.5\ \mu$M (E), and $c = 5.0\ \mu$M (F). The inset of (D) is a magnification of the number of fully bound states at $c = 0.05\ \mu$M.

where f_v is the measured force at the pulling rate v at an extension z, and f_{eq} is the measured force at extension z at equilibrium. This value increases as we increase v, since there are higher drag forces at higher pulling rates.

We also compared the force-extension curves of different concentrations at a constant pulling rate, which can be seen in Fig. 4.4B. We see qualitatively similar non-monotonic behavior with constant v at high extension as we did with constant f, shown previously in Fig. 4.3A. As concentration is increased, we observe a higher measured force at a given extension as we increase concentration from 0 μM to 10.0 μM. We then see the expected decrease in force as concentration increases further to 1000 μM. The inset to Fig. 4.4B shows the behavior at $v = 1.0 \times 10^{-1}$ and shows the same qualitative concentration-dependent trends as the low pulling rate, but also exhibits hydrodynamic drag effects.

Fig. 4.4C shows the force-extension behavior when $c = 5.0$ μM, which corresponds to the concentration where the most DNA sites are in the fully bound state. We see many qualitative similarities to the DNA only system, such as the constant force at low v and low z, hydrodynamic drag at high v and low z, and a sharp increase in measured force at high extension for all v. The effects of proteins on the system are most evident at high extension, which are shown in the inset to Fig. 4.4C. The forces measured at extensions above $180a$ increase with increasing v, which is not observed for all v in the bare DNA system. We see this effect when most of the DNA beads are in the fully bound state at low force with low numbers of the saturated bound state, which occurs between $c = 0.01$ μM and $c = 10.0$ μM. These fully proteins cause the greatest local bends in the backbone (via the equilibrium bending angle θ_0), which leads to a higher force required to extend the DNA molecule. This force also changes the binding and unbinding energies of these proteins, and these proteins "pop off" more easily as the force is increased. We see very similar behavior when $v < 2.5 \times 10^{-3}$, which corresponds to $\Gamma < 1$. When $\Gamma \geq 1$, we see marked changes in the force-extension behavior.

In addition to measuring the force as a function of extension, we can track the number of DNA sites in a given state as a function of extension and v. The most significant changes occur with the fully bound state, which corresponds to the differences seen in the equilibrium binding behavior, and is shown in Fig. 4.4D-F. At low concentrations ($c \leq 0.05$ μM), there are slight decreases in the number of beads in the fully bound state as a function of extension (Fig. 4.4D), which are most pronounced for the low pulling rates. For all concentrations, the number of proteins bound can re-equilibrate at slow pulling rates due to extremely high Γ, where the timescales associated with binding and unbinding are far faster than the timescales associated with pulling. At a faster pulling rate v, the number of proteins bound in a given state cannot re-equilibrate as the strand is extended, leading to a less of a decrease in the number of proteins fully bound. The total number of DNA beads in any bound state (P, F, or S) changes at low v, but at high v, proteins do not have time to become fully unbound from the DNA strand, leading to near constant values of total number of DNA beads in any bound state.

This v dependent unbinding behavior a function of extension is most pronounced at concentrations where there is a large difference in number of fully bound DNA beads at low extension ($\tilde{z} = 50$) and high extension ($\tilde{z} = 200$), which we call ΔC. The maximum value of ΔC occurs at $c = 0.5$ μM (Fig. 4.4E). The DNA strand starts with ≈ 65 beads in the fully bound state, and decreases to ≈ 14 beads when allowed to re-equilibrate during slow pulling, leading to $\Delta C = 51$. As we increase v, we see a decrease in ΔC, and at the fastest pulling rate $v = 1.0 \times 10^{-1}$, $\Delta C = 17$. The difference in these ΔC's (denoted by $\Delta\Delta C$) is the difference in number of fully bound proteins between the slow and fast pulling rates, leading to $\Delta\Delta C = 34$ for $c = 0.5$ μM.

We can compare these ΔCs and $\Delta\Delta C$ to those at $c = 5.0$ μM, where we see the largest number of fully bound DNA beads, shown in Fig. 4.4F. At equilibrium, $\Delta C = 42$, and at $v = 1.0 \times 10^{-1}$, $\Delta C = 23$, leading to $\Delta\Delta C = 19$. Even though there are more DNA beads in the fully bound state at $c = 5.0$ μM, there is a bigger $\Delta\Delta C$ between the slow and fast pulling rates at $c = 0.5$ μM.

This effect caused by the change in number of fully bound proteins becomes less important as the system increases in concentration beyond $c = 5.0$ μM and we begin to see more DNA beads in the saturated state at both low and high-forces. When a fully bound protein undergoes an unbinding event, it opens up a site on the DNA bead, which can be filled by another partially bound protein at high enough concentrations. The time it takes for that empty site to fill with another protein decreases as we increase the concentration. In this high concentration regime, we move from a highly bent state ($\theta_{0,F} = \pi/3$) to a less highly bent state ($\theta_{0,S} = \pi/6$), which does not decrease the force required to extend the DNA as much as movement between a highly bent state to a no-bent state.

We look at the value $\Delta C' = \Delta C - \Delta C_S/2$, where ΔC_S is the change in number of DNA sites in the saturated states. The factor of 0.5 is included because the saturated state bends the DNA less than the fully bound state. When $c < 5.0$ μM, $\Delta C \approx \Delta C'$ because there are so few DNA sites in the saturated state. At higher concentrations, these two values differ due to the increase in number of saturated states (and consequently a decrease in number of fully bound states). At 500 μM and at equilibrium, $\Delta C' = 11$, while the change in number of fully bound states is $\Delta C = 20$. If we look at the overall change in number of DNA bent sites between equilibrium and $v = 1.0 \times 10^{-1}$, we observe a $\Delta\Delta C' = 4$ at 500 μM, while $\Delta\Delta C = 10$.

We can compare the cooperative effects of pulling rate and concentration by looking at the rate- and concentration-normalized dissipative work, $\check{W}_D$, where the drag force is negligible. We can use Eq. 4.18 at a given concentration to calculate the work dissipated due to the effect of rate on the binding/unbinding behavior of the proteins. These normalized work values ($\check{W}_D$) are shown in Fig. 4.5A. We observe a region (the red area of the plot) where there is a large amount of work dissipated due to pulling rate effects on protein binding and unbinding behavior. This corresponds to the area where $\Delta\Delta C$ is high; this is caused by the greater change in force required to extend the DNA strand at higher v. This stems from two attributes of this region; (1) DNA beads tend to be in the fully bound state in equilibrium but leave the strand at high force (a high $\Delta C'$), and (2) the DNA is being pulled sufficiently quickly that the proteins do not have time to unbind. We demonstrate the first attribute by plotting $\Delta C'$ in Fig. 4.5B, which demonstrates a maximum at a concentration corresponding to the high-dissipation region seen in Fig. 4.5A. This concentration regime is the range where we see the greatest change in number of DNA beads in a bent state ($\Delta C'$), which is the underlying cause of protein unbinding regardless of the pulling rate. The second attribute reflects the dependence on pulling rate, and we thus see large values of $\check{W}_D$ occur

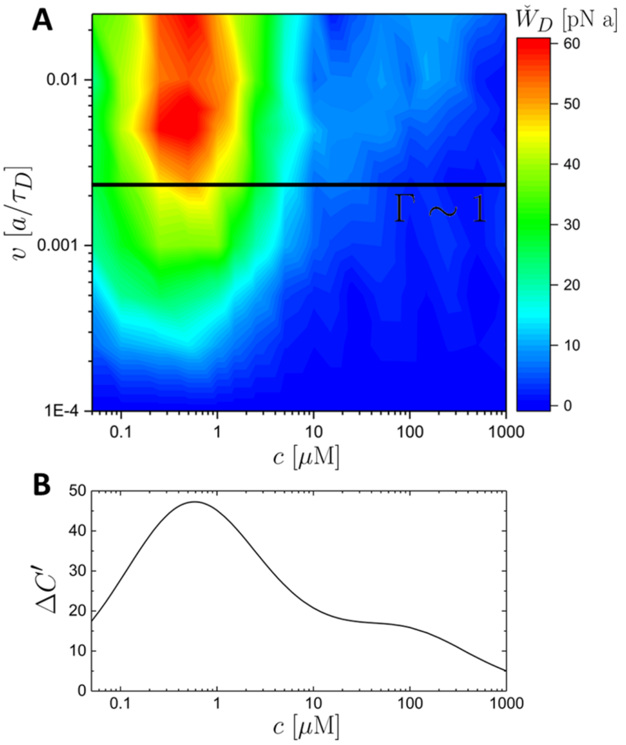

Figure 4.5: **A**. A heat map of the concentration normalized dissipative work. Data points (at a given c and v) are calculated using Eq. 4.18, where f_{eqm} is the extension-dependent force at at c and $\check{f}_v$ is the drag-normalized extension-dependent force at v. The black line is where $\Gamma \approx 1$ **B**. A representative plot of $\Delta C'$ at equilibrium.

where $\Gamma \leq 1$ (shown by the black line in Fig. 4.5A). Here, τ_P becomes less than τ_{UB}, and therefore proteins do not have time to re-equilibrate as the strand is pulled.

4.4 Conclusion

NAP-DNA interactions affect DNA conformations in ways that have been measured experimentally with single-molecule studies. This work uses coarse-grained models to demonstrate how local interactions, specifically the bending induced by the protein FIS and corresponding force-dependent binding and unbinding energies, impacts DNA equilibrium and dynamic behavior in a system with external forces. The local bending equilibrium angle is a function of the bound state of DNA, and we can thus change the force-extension behavior as a function of protein concentration in our model. This reflects previous experimental studies that postulate that FIS can partially bind to DNA [85, 105, 106, 199], and this partial binding behavior leads to non-monotonic force-extension behavior [39, 100, 103]. We are able to show how the interplay of timescales of the system can impact dynamic behavior.

This model made several simplifying assumptions about the FIS-DNA system; for example, the bending and twisting rigidity of the DNA is not changed when NAPs become bound. This may be important if we want to capture effects such as DNA stiffening behavior seen with the NAP HU [67], or more extreme bending that can cause a change in twisting rigidity such as the hairpins caused by IHF [37]. Our simulation method can be easily manipulated to account for these types of effects. We can see different types of concentration dependent force-extension behavior by changing (for example) the local equilibrium angle's stiffness κ_B or the extent that force affects the unbinding energy barrier λ. In order to take into account effects such as the dependence of binding behavior on salt, we can change the binding and unbinding energies or add in other particle-DNA interactions [67, 105].

While the focus of this work was to demonstrate fundamental equilibrium and dynamic competitions in DNA-NAP systems by mimicking experimental single molecule studies, our coarse-grained BD model can be extended past the single molecule scale. This will allow us to investigate behaviors that occur at the nucleoid scale using a model that is built up from local interactions.

Chapter 5

Influence of nucleoid associated proteins on DNA supercoiling behavior

5.1 Introduction

The nucleoid is the prokaryotic cellular structure that holds most of the genomic information in a bacterial cell. In addition to DNA, the nucleoid contains a class of proteins called nucleoid associated proteins (NAPs). NAPs bind non-specifically to the DNA and help physically organize the genetic material [32–34, 36, 40]. These interactions not only play an architectural role, but also affect biological functions such as gene expression [32, 38, 47, 48, 259], DNA replication [32, 56, 57], and transcription [32, 41, 52–54, 260].

In order for the long DNA strand (on the order of mm for prokaryotes) to fit into the much smaller cell (on the order of μm), different methods of compaction must act on the DNA [3, 9, 68, 242, 261, 262]. One of these compaction mechanisms is known as supercoiling. This occurs when the DNA double helix, which when relaxed has 1 twist per 10.5 base pairs, is torsionally stressed (such as by topoisomerases) by adding or subtracting twists [263, 264]. DNA can relieve this torsional stress by forming writhed structures. The bacterial chromosome is naturally negatively supercoiled, meaning that there is fewer than one twist per 10.5 base pairs, which is necessary for several biological functions to occur [30, 265–267]. Processes such as DNA replication or transcription require local unwinding of DNA, which produces additional twists in the DNA helix ahead of the local strand separation [268]. Negative supercoiling helps mitigate some of the positive torsional stress occurring from this process.

Single molecule studies can be used to study the physical behavior of DNA supercoiling.

Several strand properties such as extension, torque, and force can be measured as a function of how much the strand is over- or under-wound [132, 133, 269–271]. Both atomistic [272, 273] and coarse-grained simulations have been used to study supercoiling behavior [111, 131, 135, 274–278]. This approach can provide more localized information, such as the types of coils formed [111] and local defects caused by DNA supercoiling, such as kinks and bubbles [272]. Theoretical models and descriptions of DNA supercoiling have also been established [133, 134, 276, 278, 279].

A torsionally constrained strand, such as the circular plasmids found in the cell or the DNA strands used in experimental and computational single molecule studies can be defined by the topological linking number Lk. This is a constant integer that is the sum of the twist (Tw) and writhe (Wr) of the system. Twist describes how many times the individual strands of dsDNA coil around the central axis of the DNA helix. Writhe is a measure of how many times the dsDNA coils around itself. Oftentimes, a supercoiled system is described by the supercoil density σ, which is the change in linking number from its relaxed value $(Lk - Lk_0)$ normalized by the relaxed value (Lk_0), which accounts for a more direct comparison between strands of different lengths.

While DNA supercoiling has been well-characterized both experimentally and theoretically, the role that NAPs have in this process is not well understood [50]. These proteins are abundant in the cell, and many of their interactions with the DNA are well-characterized, such as their effect on force and extension behavior of DNA and some of their mesoscale roles in nucleoid architecture [67, 68, 71, 102, 103, 108, 227, 280, 281]. Some single molecule studies have investigated the role of H-NS and HU on DNA supercoiling behavior [112, 113]. With the addition of different NAPs, there is evidence of NAP-dependent supercoiling behavior as a function of force and torque. At high concentrations of H-NS, which can form stiff DNA strands, supercoil writhes start to form at higher ΔLk. Alternatively, at low concentrations of HU, which create a more compact DNA strand, coils form at a lower torque. A full understanding of the interplay between DNA supercoiling and NAPs remains to be elucidated.

This work will show how DNA supercoiling is impacted by the NAP FIS, whose binding behavior and local manipulation of DNA has been well characterized [53, 57, 99, 100, 227]. We have developed a coarse-grained simulation method to study DNA supercoiling behavior in the presence of FIS. These simulations provide a physical understanding of the different roles that FIS plays in DNA supercoiling, specifically how FIS enables the formation of writhes due to its local bending effects. Using a combination of information obtained directly from simulations, as well as theoretical predictions, we can develop a phase diagram based on the effects of FIS on the local energies of the system, including bending, excluded volume, and stretching as a function of both concentration and force. This qualitatively matches with the phase behavior measured from simulation. While the work presented here is based on FIS-DNA interactions, the theory can be easily applied to other types of proteins that have different local effects on DNA.

5.2 Materials and Methods

We use a coarse-grained Monte Carlo simulation to study our system, which is designed to be analogous to experimental single molecule studies of DNA supercoiling. A dsDNA molecule is modeled as a linear strand of $N = 100$ beads of radius $a = 4$ nm, whose locations are denoted by $\mathbf{r}_i$. The first two ($i = 1$ and $i = 2$) and last two beads ($i = 99$ and $i = 100$) are tethered along the x-axis, which limits movement of those beads to a single dimension. We include the second and second-to-last beads in this restriction to one dimensional movement to ensure that the strand is torsionally constrained throughout the simulation (constant ΔLk). All other beads are allowed to move in three dimensions.

Each bead (except for the last bead) has 3 unit vectors that fall along the axes of the body-fixed coordinate (bfc) system associated with each bead i: $\mathbf{u}_i$ is the unit vector that follows the bond vector between beads i and $i+1$:

$$\mathbf{u}_i = \frac{\mathbf{r}_{i+1} - \mathbf{r}_i}{|\mathbf{r}_{i+1} - \mathbf{r}_i|}, \tag{5.1}$$

$\mathbf{f}_i$ is perpendicular to the bond vector $\mathbf{u}_i$ (such that $\mathbf{f}_i \cdot \mathbf{u}_i = 0$), and $\mathbf{v}_i$ is the cross product of the others ($\mathbf{v}_i = \mathbf{f}_i \times \mathbf{u}_i$). This allows us to use a Euler transformation to define the twisting motion in our system, similar to previous works [131, 135].

Stretching (U_S), excluded volume (U_{EV}), bending (U_B), and twisting (U_T) potentials make up the total potential of the system. These are all included in order to correctly simulate experimentally observed DNA supercoiling behavior. Each individual potential is shown below:

$$U_S = \frac{\kappa_S}{2} \sum_{i,i+1} (b - b_0)^2 \tag{5.2}$$

where b is the distance between adjacent beads i and $i+1$ and $\kappa_S = 200\ kT$ to minimize deviations from the equilibrium bond length of $b_0 = 2.0a$,

$$U_B = \frac{\kappa_B}{2} \sum_{i=2}^{N-1} (\theta - \theta_0)^2 \tag{5.3}$$

where $\kappa_B = 6.25a$ to match the DNA persistence length of 50 nm, θ_i is the angle between the bonds of beads $i-1$ and i, and i and $i+1$, and θ_0 is the equilibrium angle between these same bonds.

$$U_T = \frac{\kappa_T}{2} \sum_{i=1}^{N-1} (\omega_i - \omega_0)^2 \tag{5.4}$$

where $\kappa_T = 12.5$ to set the twisting persistence length of DNA to 100 nm, and

$$\omega_i = \arccos((\mathbf{f}_i \cdot \mathbf{f}_{i+1} + \mathbf{v}_i \cdot \mathbf{v}_{i+1})/(1 + \mathbf{u}_i \cdot \mathbf{u}_{i+1})) \tag{5.5}$$

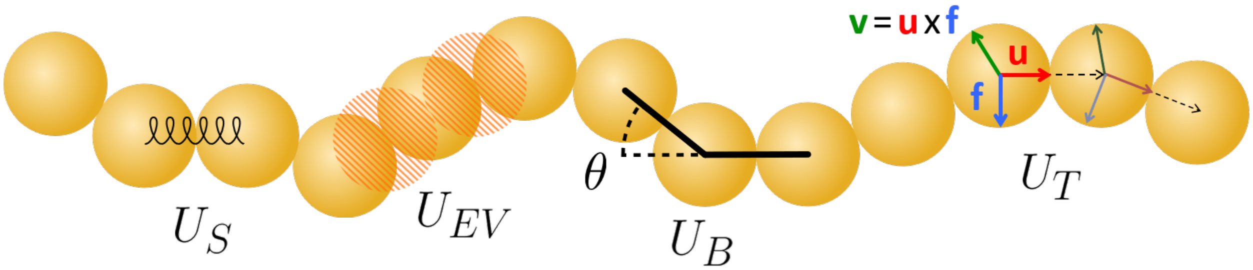

Figure 5.1: A schematic showing the potentials used in the Monte Carlo simulation. Adjacent beads are connected with stiff springs (U_S), beads (and repulsive beads located at the midpoint of each bond vector) have excluded volume (U_{EV}), the strand has a persistence length of $12.5a$ (or 50 nm) (U_B), and the strand has a twisting persitence length of $25a$ (or 100 nm) (U_T).

where **u**, **f**, and **v** are the vectors associated with the coordinate system discussed above, and

$$\begin{cases} U_{EV} = \epsilon \sum_{ij} \left(\frac{r_0}{r_{ij}}\right)^{12} & r_{ij} \leq 5.0a \\ 0 & r_{ij} > 5.0a \end{cases} \tag{5.6}$$

where $e = 0.41$. This is a purely repulsive potential to ensure that the DNA strand does not cross over itself, as that would change ΔLk of the system. To further ensure that the DNA strand does not cross over itself when several beads are in close proximity, as they can be when the strand is supercoiled, we also include repulsive beads at the midpoint of each bond vector that have only interact with each other via the excluded volume potential at very short distances ($b < 2.0a$). A representative schematic of these four types of interactions in the system can be seen in Fig. 5.1.

An implicit field of FIS proteins interact with the DNA beads and locally induce DNA bending via the equilibrium bending angle, θ_0. FIS is assumed to have multiple binding states (unbound, partially bound, or fully bound), reflecting physical intermediates in the DNA and FIS binding process that have been shown in the literature [85, 100]. This leads to a four state DNA model that has been used in previous works [227], where a single DNA site can be in one of four states: unbound (U), partially bound (P), fully bound (F), or oversaturated (S), where two proteins are partially bound to a single DNA bead. For the U and P states, the DNA prefers to be straight ($\theta_0 = 0°$), and for the F and S states, the DNA is preferentially bent ($\theta_{0,F} = 60°$ and $\theta_{0,S} = 30°$).

Because these proteins can deform the DNA locally, it follows that their binding and unbinding kinetics depend on the local structure of the DNA. In our model, a protein is more likely to bind to a DNA bead that has a bent conformation, rather than a straight one, due to a lower bending energy cost to move from the unbound to bound state. Similarly, a protein will also be less likely to unbind from a bent DNA bead than a straight one. This local structure is dependent on the force applied to the strand, as well as DNA topology (in this case, supercoiling.) The details of the FIS-DNA binding kinetics and the forms of the energy barriers can be found in Chapter 3.

5.3 Results

Simulation

To ensure that our simulation correctly captures supercoiling behavior that has been observed experimentally, we compare a set of simulations with no proteins ($c = 0$) to existing experimental data [133]. Our simulations are initiated with a linear DNA strand with a constant linking number (ΔLk, or number of extra twists added) ranging from 0 to 20. The strand is torsionally constrained at both ends to ensure that ΔLk is constant throughout the simulation. We exert a pulling force (f) on both ends of the DNA strand, within the physiologically relevant range of $0 - 10.0$ pN [161]. We allow the simulation to reach equilibrium, and measure the average extension for each pair of ΔLk and f, which can be seen in Fig. 5.2A.

At low forces (f <0.25 pN), supercoils are formed at low ΔLk, where the twists added into the system are converted into writhes. This occurs because there is effectively no penalty for decreasing the extension of the DNA strand. At mid-range forces (0.5 to 5 pN), the extension

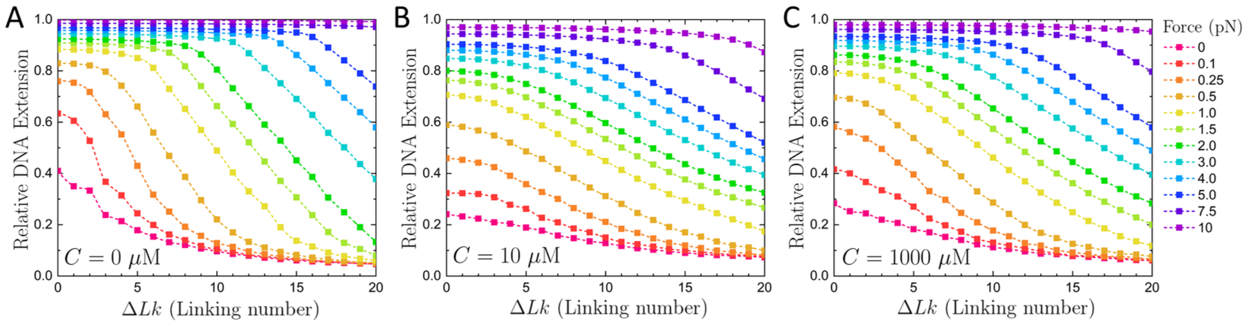

Figure 5.2: **A.** DNA extension as a function of ΔLk and force at $c = 0$. At $f < 7.5$ pN, the transitions between constant extension and decreasing extension at a constant force indicate the formation of supercoils. These transitions are not seen in this range of ΔLk for forces greater than 7.5 pN. **B.** Extension vs ΔLk for $c = 10.0\ \mu$M. We see an overall decrease in extension (at the same force) compared to the $c = 0$ plot due to the local bends caused by the fully bound state of the DNA sites, and also a shift towards lower ΔLk in the transition from constant extension to decreasing extension. **C.** Extension vs ΔLk for $c = 1000.0\ \mu$M. We see an overall decrease in extension (at the same force) compared to the $c = 0$ plot (panel A), but an increase from the $c = 10\ \mu$M (panel B) due to the smaller local bends caused by the oversaturated state of the DNA, and also a shift towards lower ΔLk in the transition from constant extension to decreasing extension.

is constant at low ΔLk but decreases linearly at high ΔLk. This is due to the conversion of extended DNA to writhed DNA. This transition begins when the penalty for decreasing the extension is less than the torsion, and the DNA strand begins writhing to alleviate the torsional stress it feels. At high forces (f >7.5 pN), the extension remains constant as ΔLk increases. The extra twists in the system remain twists and are not converted into writhes. The rising torsion of the strand is not enough to offset the penalty of decreasing the extension of the molecule at these high forces. These observations match both qualitatively and quantitatively with positively supercoiled results from the literature [133].

We introduce FIS into the simulations at a different concentrations ranging from $c = 0.1\ \mu$M to $1000\ \mu$M, resulting in a marked change in supercoiling behavior. Plots showing the extension as a function of ΔLk and force at $c = 10.0\ \mu$M and $c = 1000\ \mu$M are shown in 5.2B and C, respectively. As proteins are added into the system (up to $c = 10\ \mu$M, where the strand is effectively saturated with fully bound proteins at low force), we see an overall decrease in the measured extension at all ΔLk, due to local kinks in the DNA strand caused by protein binding [100, 227]. Above $c = 10$ μM, the extension increases slightly from its minimum value at $c = 10$ μM, due to the lesser bending caused when the strand is oversaturated with proteins, as has been shown previously [39, 100, 103, 227]. Similarly, we see a shift to a lower ΔLk where writhe formation begins at a given force (for example, writhes begin to form at $\Delta Lk = 15$ at $c = 0$ and $\Delta Lk = 7$ at $c = 10$ μM when $f = 5$ pN). This indicates that fewer twists (which corresponds to a lower applied torque, τ,) are needed to form a supercoil.

Using these sets of extension versus ΔLk at different concentrations, we can construct a DNA supercoiling phase diagram, which can be seen in Fig. 5.3. Each point on the phase transition curve comes from the ΔLk (and corresponding measured torque, τ) where supercoiling begins at a given force. Above this phase transition, DNA exists in the purely extended form (shown by the upper right inset in Fig. 5.3), where there are no writhed structures along the DNA strand. Below the transition, DNA exists in a fully supercoiled state, where the entire strand is part of a writhed structure (shown by the lower middle insets in Fig. 5.3). Along the curve is a large coexistence region, where there are both extended and writhed sections within the same DNA strand. The decreasing portions of the data in Fig. 5.2 corresponds to this coexistence region.

We observe a non-monotonic shift in this phase transition with respect to concentration, which corresponds to previously observed non-monotonic force-extension behavior [39, 100, 103, 227]. As the concentration of FIS is increased from 0 μM (black data points) to 10 μM (dark blue data points), we see a shift in supercoil formation to lower τ at a given force; this is related to the increasing number of fully bound sites along the DNA strand as c is increased. However, increasing concentration past $c = 10$ μM shifts the phase transition towards higher τ until the DNA is oversaturated with FIS, which occurs at $c = 1000\mu$M (cyan data points).

We are also able to observe an interesting change in the type of supercoil formed as concentration changes. Bare DNA forms plectonemes (both singular and branched) in our

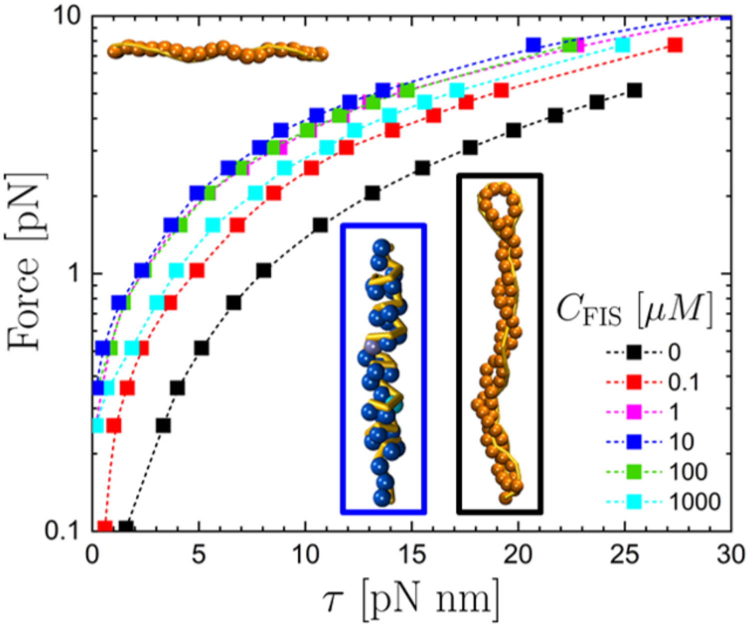

Figure 5.3: Phase transition of DNA supercoiling. Data points are from simulation with dotted lines to guide the eye. Above the transition (high force and low torque), DNA exists in an extended state, shown by the simulation example in the top left of the plot. Below the transition, DNA exists in a fully writhed state, which is shown by simulation examples in the lower right of the plots. Along the boundary exists both extended and writhed structures in the same DNA strand.

simulations, where the supercoil has a high pitch and the start and end of a given supercoil are in close proximity to each other (black boxed inset to Fig 5.3). However, when a critical number of adjacent sites are in the F or S states (≥ 6), the DNA can form a solenoid-like structure, where loops are stacked next to each other (blue boxed inset to Fig 5.3). We hypothesize that this would change to a toroid-like structure if we had a closed circular strand instead of a linear one.

The change in supercoil shape is due to the local deformations that proteins cause. When a DNA bead is the fully bound or oversaturated state, it becomes energetically favorable to adopt a more bent conformation. While there is a large bend at the apical loop of the plectoneme (seen at the top of the black box inset to Fig 5.3), most beads have just a slight bend associated with being in the main body of the plectoneme. There is a consistently larger bend for DNA beads in the entirety of the solenoid. Thus, the solenoid is the preferred conformation when several adjacent DNA sites are in the F or S states.

Theory

Theoretical models have been developed to describe DNA supercoiling behavior in a wide phase space [134]. One such theoretical model calculates the phase transition boundaries by calculating the free energies of each phase (Φ_{Ext} for extended DNA and Φ_{Sc} for supercoiled DNA) as a function of force f and torque τ. The phase transition occurs when $\Phi_{\text{Ext}} = \Phi_{\text{Sc}}$. We are interested to see how the free energies of the phases change not only with f and τ, but also with concentration. To do this, we use a combination of data from simulations, as well as theoretical estimations, to account for the effect of concentration on the terms that make up the free energies of the two different phases.

The free energy of the extended phase per a in the constant $f - \tau$ ensemble is:

$$\Phi_{\text{Ext}} = \Phi_{S,\text{Ext}}(f, c) - \Phi_{T,\text{Ext}}(\tau) \tag{5.7}$$

where the first term $\Phi_{S,\text{Ext}}$ is the stretching free energy and the last term $\Phi_{T,\text{Ext}}$ is the twisting free energy. The free energy of the supercoiled phase per a is:

$$\Phi_{\text{Sc}} = \Phi_B(f, c) - \Phi_{T,\text{Sc}}(\tau) + \Phi_{EV}(f, c) \tag{5.8}$$

where the first term Φ_B is the bending free energy, the second term accounts for the energy due to twisting ($\Phi_{T,\text{Sc}} = \Phi_{T,\text{Ext}} + \tau(-2\pi\text{Wr})$, where $\Phi_{T,\text{Ext}}$ is the same as the twisting free energy in the extended phase, and Wr is the writhe), and the last term Φ_{EV} accounts for the confinement.

The concentration-dependent energy terms are going to be affected by the number of DNA sites in a given state (U, P, F, or S), which is a function of both c and f due to the force-dependent energy barriers discussed in Chapter 3. We can calculate the fraction of DNA sites in a given state A (ϕ_A) in the extended phase with the following equations:

$$\Xi = \left[e^{(\Delta E_1+\mu_P)} + e^{(\Delta E_1+\Delta E_3+2\mu_S)} + e^{(\Delta E_1+\Delta E_2+\mu_F)} + 1\right]^N \tag{5.9}$$

where Ξ is the grand partition function of the system, ΔE_1 is the energy difference between the U and P states, ΔE_2 is the difference between the P and F states, and ΔE_3 is the difference between the P and S states (all in units of k_BT). These energy differences can be measured directly from simulations at different forces. The chemical potentials are all equal $\mu_P = \mu_S = \mu_F = \mu_0 + \ln(c)$, where $\mu_0 = 2.5$ from fits to simulation data. Eq. 5.9 can be used in the following equation to calculate ϕ_A:

$$\langle\phi_A\rangle = \frac{k_BT}{N}\frac{\partial \ln \Xi}{\partial \mu_A} \tag{5.10}$$

and the fraction of unbound states can be calculated from the following:

$$\langle\phi_U\rangle = 1 - \phi_P - \phi_F - \phi_S \tag{5.11}$$

The fraction of DNA sites in the F and S states at different c and f can be seen in Fig. 5.4. At low forces, the DNA strand has a high fraction of fully bound proteins from $c = 5$ to $c = 20$ μM, after which the fraction in the oversaturated state begins to increase. As force is increased, the fraction of fully bound states decreases due to the less-relaxed nature of the DNA strand. This allows for more oversaturated states, which have a lesser degree of bending than the fully bound states. This change in the number of F and S states will impact the concentration-dependent terms in Eqs. 5.7 and 5.8. The fraction of P states, which is not shown in Fig. 5.4, is significantly smaller than either the F or S states. ϕ_P increases slightly with force, but to a much less extent than ϕ_F or ϕ_S is changed.

For the fraction of DNA sites in a given state in the supercoil phase, we use ϕ_A at $f = 0$ for the extended phase. Proteins will be much more likely to bind to DNA in a supercoiled

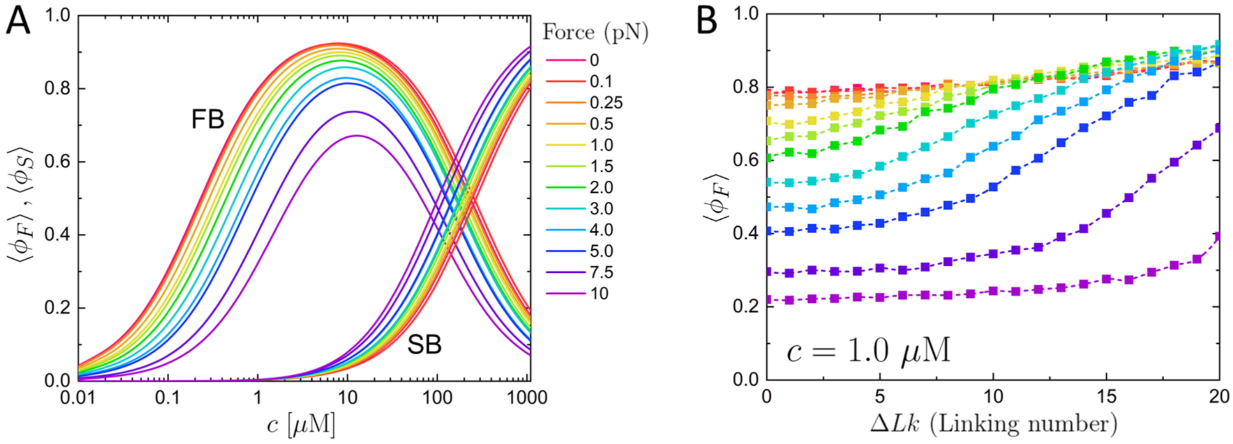

Figure 5.4: **A.** The fraction of DNA sites in the fully bound state (lines labeled FB) and oversaturated state (lines labeled SB) as a function of c and f. As force increases (red to purple), there is a decrease in F states and an increase in S. There is a peak in number of F states between 5-10 μM, which is where the number of oversaturated states begins to increase. Not shown in the plot is the fraction of DNA sites in the partially bound state, due to $\phi_P < 0.12$ for all concentrations and forces. At low forces ($f < 1$ pN), there are effectively no partially bound states. As force is increased, there is a slight increase in ϕ_P between $c = 5$ and $c = 10$ μM, corresponding to the region where the number of fully bound is very high. **B.** The fraction of DNA sites in the fully bound state as a function of f and ΔLk at $c = 1.0$ μM. When $\Delta Lk = 0$, ϕ_F matches with the theoretically predicted ϕ_F shown in panel (A). As writhes are formed at higher ΔLk, there is a significant increase ϕ_F. This increase in ϕ_F can be seen for all concentrations, but the effect is greatest between $c = 1$ and $c = 10$ μM.

phase because of the local bends, so there will be a higher number of DNA sites in one of the preferentially bent states (moreso the F state than the S state) in this phase at the same concentration. This phenomena can be observed when tracking the number of fully bound DNA sites as a function of ΔLk in the simulations, an example of which can be seen in Fig. 5.4. When the DNA strand is fully extended (at low ΔLk), the number of proteins bound is relatively constant. As a supercoil begins to form and grow (via twists being converted to writhes as ΔLk increases), there is an increase in the number of proteins bound as well.

The stretching free energy term in Eq. 5.7 can be calculated directly from a theory that has been developed to describe force-extension behavior of DNA with protein-induced local bending [227, 256]. This theory accounts for multiple binding states (and consequent multiple bending deformations) as a function of concentration. The force-extension behavior calculated from this theory via a transfer matrix formalism has been shown to qualitatively

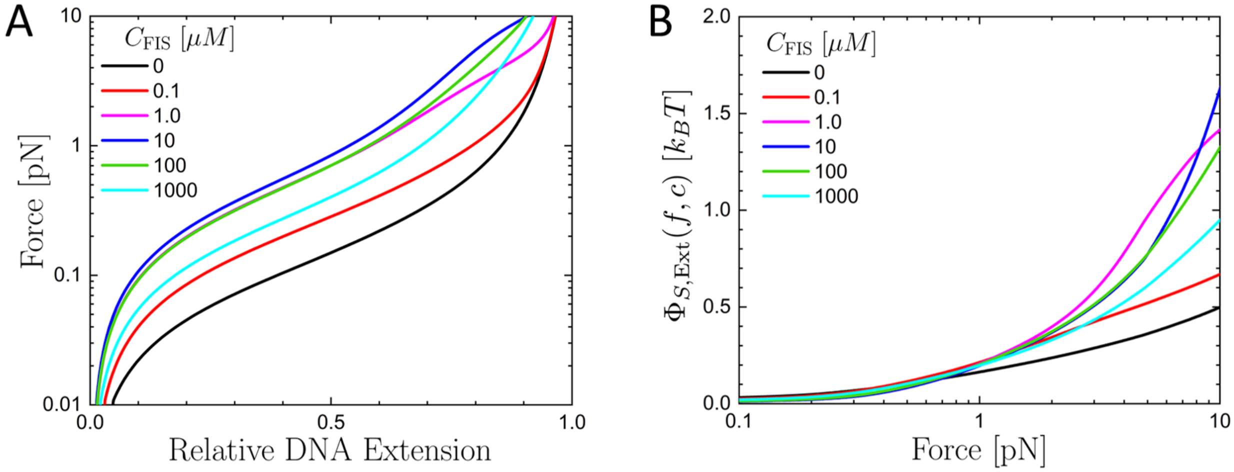

Figure 5.5: **A.** The force-extension curves calculated via the transfer matrix formalism from prior work [227]. This qualitatively matches the values from our simulations. **B.** The stretching free energy ($\Phi_{S,\text{Ext}}$) as a function of f and c, calculated from Eq. 5.12 and the transfer matrix formalism that provided $f(z)$ shown in panel (A) [227, 256].

match both experiment [100, 103] and prior simulations [227]. By integrating the force-extension curve (shown in Fig. 5.5A) up to the f of interest, we can get the stretching free energy as a function of force and concentration:

$$\Phi_{S,\text{Ext}}(f,c) = \int_0^{z_f} f(z)dz \tag{5.12}$$

where z_f is the extension at which we reach the desired f. Slight modifications to the concentrations used in this theory are necessary to better quantitatively match the limiting cases (high ϕ_F and high ϕ_S, specifically) that were observed in simulations. The stretching energy values calculated can be seen in Fig. 5.5B. We observe an increase in the energy required to fully extend the strand as c increases from 0 to 10 μM due to the addition of local kinks in the backbone, even at high forces. There is a subsequent, expected decrease as c increases to 1000 μM due to smaller local bends.

The twist free energy $\Phi_{T,\text{Ext}}$ is found in both Φ_{Ext} and Φ_{Sc}. We can measure $\Phi_{T,\text{Ext}}$ in our simulations for different c, f, and ΔLk. We find that, as expected, the average twist energy per a is the same in the extended and supercoiled phase for a given set of variables.

Therefore, these two terms cancel each other out in Eq. 5.7 and 5.8.

The bending free energy $\Phi_{B,\mathrm{Sc}}$ is, more accurately, the energetic penalty for a DNA to be in the supercoiled state instead of the extended state:

$$\Phi_B = \Phi_{B,\mathrm{Sc}} - \Phi_{B,\mathrm{Ext}} \tag{5.13}$$

The bending angle of DNA in the extended state is non-zero ($\langle \theta \rangle \neq 0$), even at very high forces, which should be accounted for in the theoretical model. We can calculate the bending energy for either phase with the following equation:

$$\Phi_{B,\mathrm{Ext,Sc}} = \phi_U \Phi_{B,U} + \phi_P \Phi_{B,P} + \phi_F \Phi_{B,F} + \phi_S \Phi_{B,S} \tag{5.14}$$

where ϕ_A is calculated from Eq. 5.10-5.11 for the extended phase, and ϕ_A for the supercoiled phase is assumed to be the values calculated at $f = 0$. $\Phi_{B,A}$ is the average bending energy for a bead in a given state (U, P, S, or F), and, like ϕ_A, is different for the extended phase and supercoiled phase. The partition function Q of a given state A of DNA in the extended phase is:

$$Q_A = \int_0^{2\pi} d\psi \int_0^{\pi} d\theta \sin\theta \exp\left[-\frac{\kappa}{2}(\theta - \theta_{0,A})^2\right] \exp\left[4f \cos\frac{\theta}{2}\right] \tag{5.15}$$

where the first Boltzmann factor is the bending energy, which accounts for different states A, and the second Boltzmann factor is the energy from the conjugate pair (fl), where $l = 4\cos\theta/2$. Eq. 5.15 can be used to calculate the average energy:

$$\Phi_{B,A} = \frac{1}{2} \frac{\frac{\kappa}{2} \int_0^{2\pi} d\psi \int_0^{\pi} d\theta (\theta - \theta_{0,A})^2 \sin\theta \exp\left[-(\frac{\kappa}{2}(\theta - \theta_{0,A})^2 - 4f\cos\frac{\theta}{2})\right]}{\int_0^{2\pi} d\psi \int_0^{\pi} d\theta \sin\theta \exp\left[-(\frac{\kappa}{2}(\theta - \theta_{0,A})^2 - 4f\cos\frac{\theta}{2})\right]} \tag{5.16}$$

where there is an extra factor of 1/2 to ensure that $\Phi_{B,A}$ is per a. The results from Eq. 5.16 quantitatively match values from our simulation and can be seen in Fig. 5.6A.

For the U and P states, as force is increased, the bending energy in the extended phase

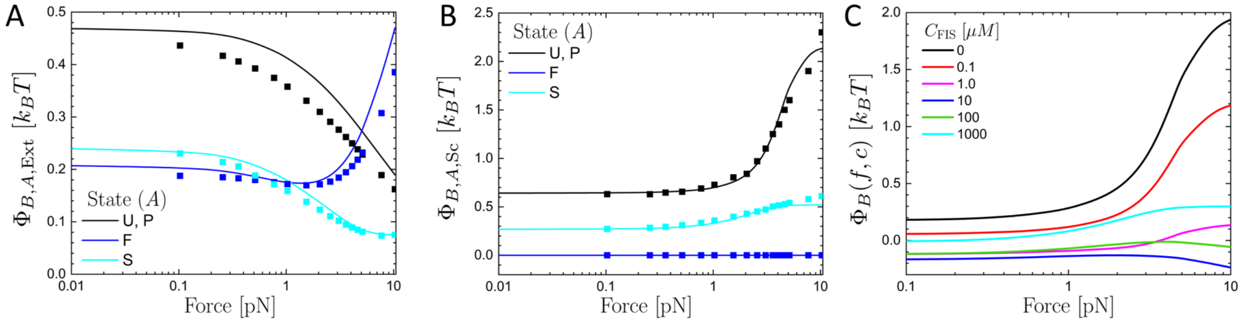

Figure 5.6: **A.** The bending free energies in the extended phase for DNA in the U and P (black), S (cyan), and F (dark blue) states. The data points are values measured in simulation, and the lines are calculated from Eq. 5.16. Because the equilibrium angle θ_0 is the same for both the U and P states, the bending energies will also be the same $\Phi_{B,U} = \Phi_{B,P}$. **B.** The bending free energies in the supercoiled phase for DNA in the U and P (black), S (cyan), and F (dark blue). The U/P and S curves are calculated from the simulation-motivated two state model in Eq. 5.17 and 5.18. $\Phi_{B,F}$ is approximated as 0 k_BT. The data points are values measured from simulation. **C.** The overall bending free energy (Φ_B) as a function of f and c calculated from Eq. 5.13 and 5.14, as well as the values shown in panels (A) and (B). As the fraction of sites in the F state increases to $c = 10$ μM, there is a significantly lower bending energy penalty due to the preference for F sites to be in a bent state, which becomes negative when the DNA strand is saturated with F states. The expected nonmonotonic behavior is observed as c increases to 1000 μM.

decreases (shown by the black line and data points in Fig 5.6A). The strand becomes more linear, leading to a smaller difference in $\theta - \theta_0$, which in turn lowers the bending energy. For beads in the F state, there is a very slight decrease, then an increase in bending energy in the extended phase as f increases, shown by the dark blue line and data points in Fig. 5.6A. This is due to the strand's local kinks becoming slightly more bent ($f < 2$ pN) and then less bent ($f \geq 2$ pN), which leads to a larger $\theta - \theta_{0,F}$ and subsequently larger $\Phi_{B,F}$. The bending energy for DNA beads in the S state have qualitatively similar trends to those found in the U or P state, seen by the light blue line and data points in Fig. 5.6A. The local angle decreases as force is increased and approaches the equilibrium angle $\theta_{0,S}$ in the extended state.

For $\Phi_{B,A}$ in the supercoiled phase, we take inspiration from the bending energies from the supercoiled phase observed in simulation. For the U, P, and S states, we use a two-state approximation for the force-dependent bending energies in the supercoiled phase:

$$\Phi_{B,U} = \Phi_{B,P} = 0.6 + \frac{0.04e^{0.95f}}{1+0.026e^{0.95f}} \tag{5.17}$$

$$\Phi_{B,S} = 0.22 + \frac{0.0525e^{1.2f}}{1+0.175e^{1.2f}} \tag{5.18}$$

These equations quantitatively match the values estimated from our simulations (see Fig. 5.6B), although there is some uncertainty at higher forces ($f \geq 7.5$ pN). This phenomenological force-dependence must be included to observe the same qualitative behavior shown in our simulations. However, more investigation is required for a full molecular understanding of the origin of this force dependence. The bending energy for DNA sites in the F state in the supercoiled phase is $\Phi_{B,F} \approx 0$, because the DNA must adopt a bent conformation in the supercoiled phase, which is favorable for the fully bound state. This nearly quantitatively matches what we observe in our simulations.

We see an increase in the bending energy as force is increased for the U, P, and S states (black and cyan lines and data points, respectively), which is in contrast to the trend shown in the extended phase (shown in Fig. 5.6A). The opposite occurs in the supercoiled phase as force is increased; the bending energy increases due to the higher bends found in the more tightly coiled plectoneme. Our approximation of $\Phi_{B,F} = 0\ k_BT$ is shown by the dark blue line and data points in Fig. 5.6B.

These force- and state-dependent energies can be used in Eq. 5.14, along with ϕ_A, to calculate a force- and concentration-dependent bending energy for the extended phase and supercoiled phase. The difference between the two, (Φ_B, which is used to calculate Φ_{Sc} in Eq. 5.8), is shown in Fig. 5.6C. As c increases, there is a non-monotonic decrease, then increase in Φ_B, due to the non-monotonic fraction of sites in the F state and an increasing number of sites in the S state. In fact, when there is a high fraction of F sites in the supercoiled phase ($c = 10\ \mu$M, blue line in Fig. 5.6C), the energy penalty becomes negative, indicating that there is actually an energy benefit for DNA to be in the supercoiled state instead of the extended state. As c increases beyond 100 μM, this energetic benefit goes away, but the resulting bending penalty (such as the one for $c = 1000$ μM shown in cyan in **??**C) is much smaller compared to the $c = 0$ case (black line in 5.6C).

The writhe used to calculate the twisting free energy of the supercoiled phase, can be calculated directly from simulations with the following equation:

$$4\pi \mathrm{Wr} = \sum_{j} \sum_{i \neq j} \left[(\mathbf{r}_{j+1} - \mathbf{r}_j) \times (\mathbf{r}_{i+1} - \mathbf{r}_i) \right] \cdot \frac{(\mathbf{r}_j - \mathbf{r}_i)}{|\mathbf{r}_j - \mathbf{r}_i|^3} \tag{5.19}$$

which calculates how many times the DNA strand crosses. This accounts for both positive and negative crossings to ensure that a relaxed DNA strand ($\Delta Lk = 0$) that crosses over and under itself multiple times has an average $\mathrm{Wr} = 0$. The average Wr per a is effectively constant for DNA that is supercoiled in our simulations, regardless of f or c, and is measured as $\mathrm{Wr} = 0.5$. There is no Wr for DNA in the extended state.

Lastly, we consider the confinement penalty for being in the supercoiled phase instead of the extended phase, $\Phi_{EV} = \Phi_{EV,\mathrm{Sc}} - \Phi_{EV,\mathrm{Ext}}$. Measurements from simulations showed only slight variations in this energy (< 0.1 k_BT) as force increased for DNA in the extended phase, and effectively no differences between the different types of DNA states. As expected, we observed a larger value of the confinement energy in the supercoiled phase, since the DNA beads are more closely packed regardless of state (which can be seen in the insets to Fig. 5.3). Because the changes are so minute between different forces and concentrations, especially compared to the absolute values of the other energy terms in Eq. 5.8, we utilize a single, constant value for Φ_{EV} in Eq. 5.8, which we approximate to be 0.1 k_BT.

With a full accounting of how each of the phases' free energies changes with force and concentration, we are able to predict how the transition between the extended and supercoiled phase changes when FIS is added to the system. The theoretical $f-\tau$ phase diagram is shown in Fig. 5.7. This qualitatively matches the phase diagram from our simulations (shown in Fig. 5.3), with the same sort of nonmonotonic shift in the phase transition (a shift to higher

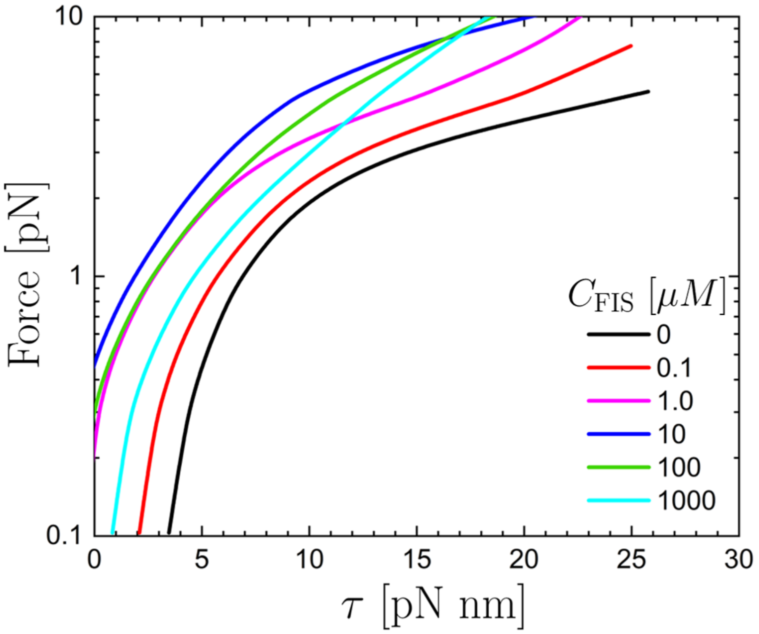

Figure 5.7: The phase transition between extended and supercoiled DNA as predicted by Eq. 5.7 and 5.8. This nearly quantitatively matches the phase behavior measured from simulations, which is shown in Fig. 5.3.

forces as c increases from 0 to 10 μM, and a subsequent decrease as $c > 10$ μM). As more DNA-deforming proteins are added to the system, the energy of the extended phase (Φ_{Ext}) increases because of an increase in the stretching energy, $\Phi_{S,\text{Ext}}$. At the same conditions (increasing c at constant f and τ), the energy in the supercoiled phase decreases because of the decrease in the bending penalty, Φ_B. There are slight quantitative differences which can be attributed to a number of factors not taken into account in our theory, such as the wall potentials used in our simulation and uncertainty in some of our energetic predictions when f is large.

5.4 Discussion

This theory allows us to understand the protein-induced molecular effects that drive DNA supercoiling beyond just FIS. For proteins such as IHF that cause a much higher degree of bending than FIS in the fully bound state, we would expect to see an even higher bending benefit because the bending energy in the extended phase (calculated from Eq. 5.16) increases significantly with a higher $\theta_{0,F}$ ($> 3\ k_BT$ for $\theta_{0,F} = 5\pi/6$), and we would expect a similar bending energy of 0 k_BT in the supercoiled phase. The stretching free energy would also increase due to the significant bends in the backbone, leading to a higher Φ_{Ext}. Together, these changes would shift the phase diagram to an even higher force than the largest one (dark blue) in Fig. 5.7.

The opposite behavior would be observed for proteins such as HU that cause a DNA stiffening effect when oversaturated. The equilibrium angle for this state would change, $\theta_{0,S} = 0$, as would the bending stiffness, κ_B. There would be a quantitative effect on the bending energy in the extended phase (Eq. 5.16) and a significant increase in the energy of bending in the supercoiled phase due to the increase in stiffness. The extended phase would become more energetically favorable to due a lower Φ_S, and this would lead to a shift to a lower force in the phase transition than even the bare DNA case (black line in Fig. 5.7).

While our model did not incorporate electrostatic effects, they can be added and would impact the confinement penalty and binding energies. For a low ionic strength system, we would expect to see an increase in the confinement penalty (which would inhibit supercoil formation), since the negatively-charged DNA strand would have a significant electrostatic repulsion. In a high salt limit (high ionic strength), these electrostatics would be screened by the ions in the solution, decreasing the confinement penalty due to electrostatics and enabling supercoil formation. Salt has also been shown to affect the binding behavior of NAPs [67, 100] and could be incorporated into the binding and unbinding energy barriers, which would change the fraction of proteins bound.

5.5 Conclusions

Understanding NAP's role in the DNA supercoiling process is important in understanding how DNA is packaged within a cell. Here, we have shown using coarse-grained simulation and theoretical techniques that FIS, an NAP which locally bends DNA, eases the formation of supercoils. These local bends make it more energetically favorable for DNA to form supercoils, which results in a lower torque required to create writhes. While simulation and theory results presented here were based on the NAP FIS, this method is not limited to this one protein. We can extend these results to other NAPs, such as HU and H-NS, which have been experimentally shown to affect DNA supercoiling, by changing some of the parameters in our simulation such as the equilibrium angles and bending stiffness. Other factors that play an important role *in vivo* and *in vitro*, including ionic strength and DNA form (such as Z-DNA or A-DNA) can also be included with parameter modifications to both the simulation and theory. This work is based on linear, single-molecule behavior, but can describe behavior at much longer length scales. Additionally, by coarse-graining several base pairs per bead (27 bp/DNA bead), we can extend our simulations to much longer time and length scales than those shown here, while maintaining computational tractability.

Chapter 6

Conclusions and future directions

This collection of work has demonstrated that the local interactions between the NAP FIS and DNA have long scale consequences. We investigated how the multivalent binding nature of NAPs leads to complex and atypical solution concentration-dependent dissociation behavior. By changing the energy barriers between different binding states, we change a protein's binding state preference at equilibrium, which in turn leads to a range of dissociation behaviors. These dissociation rates were normalized to a single off-rate curve. This universal curve describes the dissociation kinetics of not just our model FIS-DNA system, but also complexes that exhibit an intermediate, partially bound state.

We also demonstrated that the dissociation kinetics in our system are not only affected by external concentration, but also applied force. Instead of manually manipulating the energy barriers between states, we allowed them to change based on the applied force and how it impacted the local geometry of a DNA binding site. This again biased the protein into different states based on the force applied, which changed how the protein dissociated from its DNA substrate. We saw a competition between the force-driven unbinding of these complexes, which sped up the dissociation process, and the force-inhibited binding of the proteins in solution, which slowed the dissociation process. While this phenomena has not been experimentally observed for NAP-DNA systems, this competitive effect of force and concentration may be a route that cells use to dissociate a NAP from DNA *in vivo*.

This force-dependent kinetic binding and unbinding also has effects on DNA elasticity, which we studied under equilibrium and dynamic conditions. We found that the relative timescales of the system, one associated with proteins and one associated with DNA, worked in concert to change DNA elasticity and protein kinetics simutaneously. While the timescales in our simulation were short in real time (<seconds), we could point to the importance of these timescales relative to each other, which can be extrapolated to real-time dynamics that occur *in vitro* or *in vivo*.

Lastly, we studied how the local deformations of these proteins impact the formation and stability of mesoscale DNA supercoils. We showed that FIS's preference for bent DNA impacted whether it was more likely to be bound to DNA that was supercoiled or extended, and that this in turn stabilized the DNA supercoils. A theory based on energies of the system (like bending and stretching) was able to qualitatively describe the supercoiling behavior we observed in our simulations. The theory can be readily modified to account for different concentration and deformation effects that might be caused by other proteins.

While the work presented here was focused on a simple model system of a single type of NAP (FIS) and DNA, this method can be easily extended to incorporate many types of NAPs. Each different type of protein can have its own independent set of binding and unbinding energies, as well as local deformations. For example, fully bound IHF causes "U-turn" bends up to 160° which can be incorporated via the equilibrium bending angle, while a DNA strand oversaturated with HU causes DNA stiffening, which can be changed via the bending stiffness, κ_B. Different proteins will undoubtedly change the mesoscale behaviors studied here, but our work provides a foundation for understanding how these different local effects will affect behaviors like facilitated dissociation and concentration-dependent DNA elasticity. The inclusion of more proteins will move us closer to the complexity of a nucleoid, where proteins and forces interact at the local scale to change the overall structure.

In addition to diversifying the set of NAPs in our system, we can make other biologically inspired changes to our model to approach nucleoid-scale behavior. We can model DNA as plasmid, a closed circle of DNA, which is how DNA naturally exists in prokaryotic cells. Other biological factors, including ionic and crowding effects [282, 283], can be incorporated into our model via the addition of an electrostatic potential (ionic strength) or macromolecules with excluded volume (crowding).

This level of coarse-graining (many base pairs per bead, corresponding to a single FIS-DNA binding site) does not limit us to the short single molecule length scales investigated here (~ 1 μm). A non-optimized simulation with 100 beads and a mean field of proteins (typical simulation for the work presented here) takes approximately one day on a single CPU thread to reach real time scales on the order of seconds. With optimization, systems reaching lengths of ~ 100 μM can still be computationally tractable at this level of coarse graining.

In addition to simply increasing the size of our simulation, we can further coarse-grain our model to longer "real" lengths by incorporating the mesoscale effects we show at a longer scale. For example, we showed that FIS bound to DNA decreases the extension of the DNA strand, and we can incorporate this effect with different bending stiffnesses and different equilibrium bending angles at longer length scales, where a single bead may represent many binding sites instead of the single binding site used in the work presented here. This would allow us to reach even longer time and length scales that approach the scale of the full nucleoid (>mm and >seconds)

The theories developed to describe different aspects of our model NAP-DNA system can also be extended to other protein-DNA systems. For example, protein binding and DNA elasticity have a symbiotic relationship that is related to the force and time scales of the system. Our work with FIS gives us insight into how different NAP systems, such as IFH-DNA or HU-DNA, might behave under the same sort of dynamic conditions. These sorts of hypothesis, built from our understanding of local interactions, can be easily tested and implemented into a more comprehensive model that includes many types of proteins as mentioned above.

Bibliography

1. 2008. Genome. In: *Encyclopedia of Genetics, Genomics, Proteomics and Informatics.* Springer Netherlands, Dordrecht, 785–786.
2. Pombo, A., and N. Dillon. 2015. Three-dimensional genome architecture: players and mechanisms. *Nature Nat. Rev. Mol. Cell Biol.* 16:245.
3. Hofmann, A., and D. W. Heermann. 2015. The role of loops on the order of eukaryotes and prokaryotes. *FEBS letters.* 589:2958–2965.
4. Nora, E. P., B. R. Lajoie, E. G. Schulz, L. Giorgetti, I. Okamoto, N. Servant, T. Piolot, N. L. van Berkum, J. Meisig, J. Sedat, et al. 2012. Spatial partitioning of the regulatory landscape of the x-inactivation centre. *Nature.* 485:381.
5. Thanbichler, M., and L. Shapiro. 2006. Chromosome organization and segregation in bacteria. *J. Struct. Biol.* 156:292–303.
6. Dixon, J. R., S. Selvaraj, F. Yue, A. Kim, Y. Li, Y. Shen, M. Hu, J. S. Liu, and B. Ren. 2012. Topological domains in mammalian genomes identified by analysis of chromatin interactions. *Nature.* 485:376.
7. Lieberman-Aiden, E., N. L. Van Berkum, L. Williams, M. Imakaev, T. Ragoczy, A. Telling, I. Amit, B. R. Lajoie, P. J. Sabo, M. O. Dorschner, et al. 2009. Comprehensive mapping of long-range interactions reveals folding principles of the human genome. *Science.* 326:289–293.
8. Nuebler, J., G. Fudenberg, M. Imakaev, N. Abdennur, and L. A. Mirny. 2018. Chromatin organization by an interplay of loop extrusion and compartmental segregation. *Proc. Natl. Acad. Sci. U. S. A.* 115:E6697–E6706.
9. Sinden, R. R., and D. E. Pettijohn. 1981. Chromosomes in living Escherichia coli cells are segregated into domains of supercoiling. *Proc. Natl. Acad. Sci. U. S. A.* 78:224–228.
10. Maurer, S., J. Fritz, and G. Muskhelishvili. 2009. A systematic in vitro study of nucleoprotein complexes formed by bacterial nucleoid-associated proteins revealing novel types of DNA organization. *J. Mol. Biol.* 387:1261–1276.
11. Postow, L., C. D. Hardy, J. Arsuaga, and N. R. Cozzarelli. 2004. Topological domain structure of the Escherichia coli chromosome. *Genes Dev.* 18:1766–1779.

12. Travers, A., and G. Muskhelishvili. 2005. Bacterial chromatin. *Curr. Opin. Genet. Dev.* 15:507–514.

13. Valens, M., S. Penaud, M. Rossignol, F. Cornet, and F. Boccard. 2004. Macrodomain organization of the Escherichia coli chromosome. *EMBO J.* 23:4330–4341.

14. Cunha, S., C. L. Woldringh, and T. Odijk. 2005. Restricted diffusion of DNA segments within the isolated Escherichia coli nucleoid. *J. Struct. Biol.* 150:226–232.

15. Cavalli, G., and T. Misteli. 2013. Functional implications of genome topology. *Nat. Struct. Mol. Biol.* 20:290.

16. Hou, C., and V. G. Corces. 2012. Throwing transcription for a loop: expression of the genome in the 3D nucleus. *Chromosoma.* 121:107–116.

17. Gilbert, N., and J. Allan. 2014. Supercoiling in DNA and chromatin. *Curr. Opin. Genet. Dev.* 25:15–21.

18. Dorman, C. J. 2006. DNA supercoiling and bacterial gene expression. *Sci. Prog.* 89:151–166.

19. Baranello, L., D. Levens, A. Gupta, and F. Kouzine. 2012. The importance of being supercoiled: how DNA mechanics regulate dynamic processes. *BBA-Gene Regul. Mech.* 1819:632–638.

20. Vogelstein, B., D. M. Pardoll, and D. S. Coffey. 1980. Supercoiled loops and eucaryotic DNA replication. *Cell.* 22:79–85.

21. Schultz, M., S. Brill, Q. Ju, R. Sternglanz, and R. Reeder. 1992. Topoisomerases and yeast rRNA transcription: negative supercoiling stimulates initiation and topoisomerase activity is required for elongation. *Genes Dev.* 6:1332–1341.

22. Higgins, C. F., C. J. Dorman, D. A. Stirling, L. Waddell, I. R. Booth, G. May, and E. Bremer. 1988. A physiological role for DNA supercoiling in the osmotic regulation of gene expression in S. typhimurium and E. coli. *Cell.* 52:569–584.

23. Wu, H.-Y., S. Shyy, J. C. Wang, and L. F. Liu. 1988. Transcription generates positively and negatively supercoiled domains in the template. *Cell.* 53:433–440.

24. Liu, L. F., and J. C. Wang. 1987. Supercoiling of the DNA template during transcription. *Proc. Natl. Acad. Sci. U. S. A.* 84:7024–7027.

25. García-Rubio, M. L., and A. Aguilera. 2011. Topological constraints impair RNA polymerase II transcription and causes instability of plasmid-borne convergent genes. *Nucleic Acids Res.* 40:1050–1064.

26. Rovinskiy, N., A. A. Agbleke, O. Chesnokova, Z. Pang, and N. P. Higgins. 2012. Rates of gyrase supercoiling and transcription elongation control supercoil density in a bacterial chromosome. *PLoS Genet.* 8:e1002845.

27. Naughton, C., N. Avlonitis, S. Corless, J. G. Prendergast, I. K. Mati, P. P. Eijk, S. L. Cockroft, M. Bradley, B. Ylstra, and N. Gilbert. 2013. Transcription forms and remodels supercoiling domains unfolding large-scale chromatin structures. *Nat. Struct. Mol. Biol.* 20:387.

28. Corless, S., and N. Gilbert. 2016. Effects of DNA supercoiling on chromatin architecture. *Biophys. Rev.* 8:245–258.

29. Bermudez, I., J. García-Martínez, J. E. Pérez-Ortín, and J. Roca. 2010. A method for genome-wide analysis of DNA helical tension by means of psoralen-DNA photobinding. *Nucleic Acids Res.* 38:e182–e182.

30. Marians, K. J. 1992. Prokaryotic DNA replication. *Annu. Rev. Biochem.* 61:673–715.

31. Luijsterburg, M., M. Noom, and G. Wuite. 2006. The architectural role of nucleoid-associated proteins in the organization of bacterial chromatin: a molecular perspective. *J. Struct. Biol.* 156:262–272.

32. Dillon, S. C., and C. J. Dorman. 2010. Bacterial nucleoid-associated proteins, nucleoid structure and gene expression. *Nat. Rev. Micro.* 8:185–195.

33. Dorman, C. J. 2009. Nucleoid-associated proteins and bacterial physiology. *Adv. Appl. Microbiol.* 67:47–64.

34. Luijsterburg, M. S., M. C. Noom, G. J. Wuite, and R. T. Dame. 2006. The architectural role of nucleoid-associated proteins in the organization of bacterial chromatin: a molecular perspective. *J. Struct. Biol.* 156:262–272.

35. Luijsterburg, M. S., M. F. White, R. van Driel, and R. T. Dame. 2008. The major architects of chromatin: Architectural proteins in bacteria, archaea and eukaryotes. *Crit. Rev. Biochem. Mol. Biol.* 43:393–418.

36. Grainger, D. C., D. Hurd, M. D. Goldberg, and S. J. W. Busby. 2006. Association of nucleoid proteins with coding and non-coding segments of the Escherichia coli genome. *Nucleic Acids Res.* 34:4642–4652.

37. Swinger, K. K., and P. A. Rice. 2004. IHF and HU: flexible architects of bent DNA. *Curr. Opin. Struct. Biol.* 14:28 – 35.

38. Browning, D. F., D. C. Grainger, and S. J. Busby. 2010. Effects of nucleoid-associated proteins on bacterial chromosome structure and gene expression. *Curr. Opin. Microbiol.* 13:773–780.

39. Skoko, D., B. Wong, R. Johnson, and J. Marko. 2004. Micromechanical analysis of the binding of DNA-bending proteins HMGB1, NHP6A, and HU reveals their ability to form highly stable DNA-protein complexes. *Biochemistry.* 43:13867–13874.

40. Drlica, K., and R. J. 1987. Histonelike proteins of bacteria. *Microbiol. Rev.* 51:301–319.

41. Rice, P., S. Yang, K. Mizuuchi, and H. Nash. 1996. Crystal structure of an IHF-DNA complex: a protein-induced DNA U-turn. *Cell.* 87:1295–306.

42. Yuan, H., S. Finkel, J. Feng, K. M, R. Johnson, and R. Dickerson. 1991. The molecular structure of wild-type and a mutant Fis protein: relationship between mutational changes and recombinational enhancer function or DNA binding. *Proc. Natl. Acad. Sci. U. S. A.* 88:9558–62.

43. Swinger, K. K., K. M. Lemberg, Y. Zhang, and P. A. Rice. 2003. Flexible DNA bending in HU–DNA cocrystal structures. *The EMBO Journal.* 22:3749–3760.

44. Stella, S., D. Cascio, and R. C. Johnson. 2010. The shape of the DNA minor groove directs binding by the DNA-bending protein Fis. *Genes Dev.* 24:814–826.

45. Hancock, S. P., T. Ghane, D. Cascio, R. Rohs, R. Di Felice, and R. C. Johnson. 2013. Control of DNA minor groove width and Fis protein binding by the purine 2-amino group. *Nucleic Acids Res.* 41:6750.

46. Pan, C. Q., S. E. Finkel, S. E. Cramton, J.-A. Feng, D. S. Sigman, and R. C. Johnson. 1996. Variable structures of Fis-DNA complexes determined by flanking DNA-protein contacts. *J. Mol. Biol.* 264:675 – 695.

47. Atlung, T., and H. Ingmer. 1997. H-NS: a modulator of environmentally regulated gene expression. *Mol. Microbiol.* 24:7–17.

48. Zwir, I., W.-S. Yeo, D. Shin, T. Latifi, H. Huang, and E. A. Groisman. 2014. Bacterial nucleoid-associated protein uncouples transcription levels from transcription timing. *mBio.* 5:e01485–14.

49. Odermatt, N. T., C. Sala, A. Benjak, and S. T. Cole. 2018. Essential nucleoid associated protein mIHF (Rv1388) controls virulence and housekeeping genes in mycobacterium tuberculosis. *Sci. Rep.* 8:14214.

50. Rimsky, S., and A. Travers. 2011. Pervasive regulation of nucleoid structure and function by nucleoid-associated proteins. *Curr. Opin. Microbiol.* 14:136–141.

51. Schechter, L. M., S. Jain, S. Akbar, and C. A. Lee. 2003. The small nucleoid-binding proteins H-NS, HU, and Fis affect hilA expression in Salmonella enterica Serovar Typhimurium. *Infect. Immun.* 71:5432–5435.

52. Hengge-Aronis, R. 1999. Interplay of global regulators and cell physiology in the general stress response of Escherichia coli. *Curr. Opin. Microbiol.* 2:148–152.

53. Finkel, S. E., and R. C. Johnson. 1992. The Fis protein: it's not just for DNA inversion anymore. *Mol. Microbiol.* 6:3257–3265.

54. Berger, M., A. Farcas, M. Geertz, P. Zhelyazkova, K. Brix, A. Travers, and G. Muskhelishvili. 2010. Coordination of genomic structure and transcription by the main bacterial nucleoid-associated protein HU. *EMBO Rep.* 11:59–64.

55. Chen, T.-Y., A. G. Santiago, W. Jung, Ł. Krzemiński, F. Yang, D. J. Martell, J. D. Helmann, and P. Chen. 2015. Concentration-and chromosome-organization-dependent regulator unbinding from dna for transcription regulation in living cells. *Nat. Commun.* 6:7445.

56. Leonard, A. C., and J. E. Grimwade. 2005. Building a bacterial orisome: emergence of new regulatory features for replication origin unwinding. *Mol, Microbiol.* 55:978–985.

57. Gille, H., J. B. Egan, A. Roth, and W. Messer. 1991. The Fis protein binds and bends the origin of chromosomal DNA replication, oriC, of Escherichia coli. *Nucleic Acids Res.* 19:4167–4172.

58. Humphrey, W., A. Dalke, and K. Schulten. 1996. VMD – Visual Molecular Dynamics. *J. Mol. Graphics.* 14:33–38.

59. Luger, K., A. W. Mäder, R. K. Richmond, D. F. Sargent, and T. J. Richmond. 1997. Crystal structure of the nucleosome core particle at 2.8 Å resolution. *Nature.* 389:251.

60. Kim, D.-H., H. Im, J.-G. Jee, S.-B. Jang, H.-J. Yoon, A.-R. Kwon, S.-M. Kang, and B.-J. Lee. 2014. β-Arm flexibility of HU from Staphylococcus aureus dictates the DNA-binding and recognition mechanism. *Acta Crystallogr. D.* 70:3273–3289.

61. Jenuwein, T., and C. D. Allis. 2001. Translating the histone code. *Science.* 293:1074–1080.

62. Thoma, F., and T. Koller. 1977. Influence of histone H1 on chromatin structure. *Cell.* 12:101–107.

63. Misteli, T., A. Gunjan, R. Hock, M. Bustin, and D. T. Brown. 2000. Dynamic binding of histone H1 to chromatin in living cells. *Nature.* 408:877.

64. Dame, R. T., C. Wyman, and N. Goosen. 2000. H-NS mediated compaction of DNA visualised by atomic force microscopy. *Nucleic Acids Res.* 28:3504–3510.

65. Ali Azam, T., A. Iwata, A. Nishimura, S. Ueda, and A. Ishihama. 1999. Growth phase-dependent variation in protein composition of the Escherichia coli nucleoid. *J. Bacteriol.* 181:6361–6370.

66. Yan, J., and J. F. Marko. 2003. Effects of DNA-distorting proteins on DNA elastic response. *Phys. Rev. E.* 68:011905.

67. Xiao, B., R. C. Johnson, and J. F. Marko. 2010. Modulation of HU-DNA interactions by salt concentration and applied force. *Nucleic Acids Res.* 38:6176.

68. Skoko, D., D. Yoo, H. Bai, B. Schnurr, J. Yan, M. S. M, J. F. Marko, and R. C. Johnson. 2006. Mechanism of chromosome compaction and looping by the Escherichia coli nucleoid protein Fis. *J. Mol. Biol.* 364:777–798.

69. Nowak-Lovato, K., L. B. Alexandrov, A. Banisadr, A. L. Bauer, A. R. Bishop, A. Usheva, F. Mu, E. Hong-Geller, K. Rasmussen, W. S. Hlavacek, and B. S. Alexandrov. 2013. Binding of nucleoid-associated protein Fis to DNA is regulated by DNA breathing dynamics. *PLoS Comput. Biol.* 9:e1002881.

70. Dixon, N. E., and A. Kornberg. 1984. Protein HU in the enzymatic replication of the chromosomal origin of Escherichia coli. *Proc. Natl. Acad. Sci. U. S. A.* 81:424–428.

71. Lin, J., H. Chen, P. Drge, and J. Yan. 2012. Physical organization of DNA by multiple non-specific DNA-binding modes of integration host factor (IHF). *PLOS ONE.* 7:1–10.

72. Owen-Hughes, T. A., G. D. Pavitt, D. S. Santos, J. M. Sidebotham, C. S. Hulton, J. C. Hinton, and C. F. Higgins. 1992. The chromatin-associated protein H-NS interacts with curved DNA to influence DNA topology and gene expression. *Cell.* 71:255–265.

73. Yamada, H., S. Muramatsu, and T. Mizuno. 1990. An Escherichia coli protein that preferentially binds to sharply curved DNA. *J. Biochem.* 108:420–425.

74. Rimsky, S. 2004. Structure of the histone-like protein H-NS and its role in regulation and genome superstructure. *Curr. Opin. Microbiol.* 7:109–114.

75. Dame, R. T., M. C. Noom, and G. J. Wuite. 2006. Bacterial chromatin organization by H-NS protein unravelled using dual DNA manipulation. *Nature.* 444:387.

76. Martinez, A., and R. Kolter. 1997. Protection of DNA during oxidative stress by the nonspecific dna-binding protein dps. *J. Bacteriol.* 179:5188–5194.

77. Grant, R., D. Filman, S. Finkel, R. Kolter, and J. Hogle. 1998. The crystal structure of Dps, a ferritin homolog that binds and protects DNA. *Nat. Struct. Biol.* 5:294–303.

78. Sonnenfield, J., C. Burns, C. Higgins, and J. Hinton. 2001. The nucleoid-associated protein StpA binds curved DNA, has a greater DNA-binding affinity than H-NS and is present in significant levels in hns mutants. *Biochimie.* 83:243–249.

79. Zhang, A., and M. Belfort. 1992. Nucleotide sequence of a newly-identified Escherichia coli gene, stpA, encoding an H-NS-like protein. *Nucleic Acids Res.* 20:6735.

80. Rouvire-Yaniv, J., M. Yaniv, and J.-E. Germond. 1979. E. coli DNA binding protein HU forms nucleosome-like structure with circular double-stranded DNA. *Cell.* 17:265 – 274.

81. Datta, C., R. K. Jha, S. Ganguly, and V. Nagaraja. 2019. NapA (Rv0430), a novel nucleoid-associated protein that regulates a virulence operon in Mycobacterium tuberculosis in a supercoiling-dependent manner. *J. Mol. Bio.* 431:1576–1591.

82. Liu, Y., H. Wang, T. Cui, X. Zhou, Y. Jia, H. Zhang, and Z.-G. He. 2016. NapM, a new nucleoid-associated protein, broadly regulates gene expression and affects mycobacterial resistance to anti-tuberculosis drugs. *Mol. Microbiol.* 101:167–181.

83. Ogura, M., and Y. Kanesaki. 2018. Newly identified nucleoid-associated-like protein YlxR regulates metabolic gene expression in Bacillus subtilis. *mSphere.* 3:e00501–18.

84. de Barsy, M., L. Herrgott, V. Martin, T. Pillonel, P. H. Viollier, and G. Greub. 2019. Identification of new DNA-associated proteins from Waddlia chondrophila. *Sci. Rep.* 9:1–12.

85. Tsai, M.-Y., B. Zhang, W. Zheng, and P. G. Wolynes. 2016. Molecular mechanism of facilitated dissociation of Fis protein from DNA. *J. Am. Chem. Soc.* 138:13497–13500. PMID: 27685351.

86. Wagner, C., C. Olbrich, H. Brutzer, M. Salomo, U. Kleinekathöfer, U. F. Keyser, and F. Kremer. 2011. DNA condensation by TmHU studied by optical tweezers, AFM and molecular dynamics simulations. *J. Biol. Phys.* 37:117–131.

87. Nguyen, H., T. Pham, H. L. Nguyen, and T. Phan. 2018. Investigation of binding affinity between prokaryotic proteins (AHU-IHF) and DNAs: Steered molecular dynamics approach. *Biotechnol. Appl. Biochem.* 186:834–846.

88. Wang, W., G.-W. Li, C. Chen, X. S. Xie, and X. Zhuang. 2011. Chromosome organization by a nucleoid-associated protein in live bacteria. *Science.* 333:1445–1449.

89. Coquel, A.-S., J.-P. Jacob, M. Primet, A. Demarez, M. Dimiccoli, T. Julou, L. Moisan, A. B. Lindner, and H. Berry. 2013. Localization of protein aggregation in Escherichia coli is governed by diffusion and nucleoid macromolecular crowding effect. *PLoS computational biology.* 9:e1003038.

90. Lee, S. F., M. A. Thompson, M. A. Schwartz, L. Shapiro, and W. Moerner. 2011. Super-resolution imaging of the nucleoid-associated protein HU in Caulobacter crescentus. *Biophys. J.* 100:L31–L33.

91. Uphoff, S., R. Reyes-Lamothe, F. G. de Leon, D. J. Sherratt, and A. N. Kapanidis. 2013. Single-molecule DNA repair in live bacteria. *Proc. Natl. Acad. Sci. U. S. A.* 110:8063–8068.

92. Fisher, J. K., A. Bourniquel, G. Witz, B. Weiner, M. Prentiss, and N. Kleckner. 2013. Four-dimensional imaging of E. coli nucleoid organization and dynamics in living cells. *Cell.* 153:882–895.

93. Stracy, M., S. Uphoff, F. G. de Leon, and A. N. Kapanidis. 2014. In vivo single-molecule imaging of bacterial DNA replication, transcription, and repair. *FEBS Lett.* 588:3585–3594.

94. Naumova, N., M. Imakaev, G. Fudenberg, Y. Zhan, B. R. Lajoie, L. A. Mirny, and J. Dekker. 2013. Organization of the mitotic chromosome. *Science.* 342:948–953.

95. Le, T. B., M. V. Imakaev, L. A. Mirny, and M. T. Laub. 2013. High-resolution mapping of the spatial organization of a bacterial chromosome. *Science.* 342:731–734.

96. Jun, S., and B. Mulder. 2006. Entropy-driven spatial organization of highly confined polymers: lessons for the bacterial chromosome. *Proc. Natl. Acad. Sci. U. S. A.* 103:12388–12393.

97. Chaudhuri, D., and B. M. Mulder. 2018. Molecular dynamics simulation of a feather-boa model of a bacterial chromosome. *In* Bacterial Chromatin. Springer. 403–415.

98. Lioy, V. S., A. Cournac, M. Marbouty, S. Duigou, J. Mozziconacci, O. Espéli, F. Boccard, and R. Koszul. 2018. Multiscale structuring of the E. coli chromosome by nucleoid-associated and condensin proteins. *Cell.* 172:771–783.

99. Graham, J. S., R. C. Johnson, and J. F. Marko. 2011. Concentration-dependent exchange accelerates turnover of proteins bound to double-stranded DNA. *Nucleic Acids Res.* 39:2249–2259.

100. Giuntoli, R. D., N. B. Linzer, E. J. Banigan, C. E. Sing, M. O. de la Cruz, J. S. Graham, R. C. Johnson, and J. F. Marko. 2015. DNA-segment-facilitated dissociation of Fis and NHP6A from DNA detected via single-molecule mechanical response. *J. Mol. Biol.* 427:3123 – 3136.

101. Kamagata, K., E. Mano, K. Ouchi, S. Kanbayashi, and R. C. Johnson. 2018. High free-energy barrier of 1D diffusion along DNA by architectural dna-binding proteins. *J. Mol. Biol.* 430:655–667.

102. Ali, B. M. J., R. Amit, I. Braslavsky, A. B. Oppenheim, O. Gileadi, and J. Stavans. 2001. Compaction of single DNA molecules induced by binding of integration host factor (IHF). *Proc. Natl. Acad. Sci. U. S. A.* 98:10658–10663.

103. Xiao, B., H. Zhang, R. C. Johnson, and J. F. Marko. 2011. Force-driven unbinding of proteins HU and Fis from DNA quantified using a thermodynamic maxwell relation. *Nucleic Acids Res.* 39:5568–5577.

104. Hadizadeh, N., R. C. Johnson, and J. F. Marko. 2016. Facilitated dissociation of a nucleoid protein from the bacterial chromosome. *J. Bacteriol.* 198:1735–42.

105. Kamar, R. I., E. J. Banigan, A. Erbas, R. D. Giuntoli, M. Olvera de la Cruz, R. C. Johnson, and J. F. Marko. 2017. Facilitated dissociation of transcription factors from single DNA binding sites. *Proc. Natl. Acad. Sci. U. S. A.* 114:E3251–E3257.

106. Sing, C. E., M. Olvera de la Cruz, and J. F. Marko. 2014. Multiple-binding-site mechanism explains concentration-dependent unbinding rates of DNA-binding proteins. *Nucleic Acids Res.* 42:3783–3791.

107. Yan, J., D. Skoko, and J. F. Marko. 2004. Near-field-magnetic-tweezer manipulation of single DNA molecules. *Phys. Rev. E.* 70:011905.

108. van Noort, J., S. Verbrugge, N. Goosen, C. Dekker, and R. T. Dame. 2004. Dual architectural roles of HU: Formation of flexible hinges and rigid filaments. *Proc. Natl. Acad. Sci. U. S. A.* 101:6969–6974.

109. Tan, C., T. Terakawa, and S. Takada. 2016. Dynamic coupling among protein binding, sliding, and DNA bending revealed by molecular dynamics. *J. Am. Chem. Soc.* 138:8512–8522. PMID: 27309278.

110. Brackley, C. A., B. Liebchen, D. Michieletto, F. Mouvet, P. R. Cook, and D. Marenduzzo. 2017. Ephemeral protein binding to DNA shapes stable nuclear bodies and chromatin domains. *Biophys. J.* 112:1085 – 1093.

111. Krajina, B. A., and A. J. Spakowitz. 2016. Large-scale conformational transitions in supercoiled DNA revealed by coarse-grained simulation. *Biophys. J.* 111:1339–1349.

112. Lim, C. J., L. J. Kenney, and J. Yan. 2014. Single-molecule studies on the mechanical interplay between DNA supercoiling and H-NS DNA architectural properties. *Nucleic Acids Res.* 42:8369.

113. Schnurr, B., C. Vorgias, and J. Stavans. 2006. Compaction and supercoiling of single, long DNA molecules by HU protein. *Biophys. Rev. Lett.* 01:29–44.

114. Czapla, L., D. Swigon, and W. K. Olson. 2008. Effects of the nucleoid protein HU on the structure, flexibility, and ring-closure properties of DNA deduced from monte carlo simulations. *J. Mol. Biol.* 382:353–370.

115. Potoyan, D. A., A. Savelyev, and G. A. Papoian. 2013. Recent successes in coarse-grained modeling of DNA. *Wiley Interdiscip. Rev. Comput. Mol. Sci.* 3:69–83.

116. Knotts, T. A., N. Rathore, D. C. Schwartz, and J. J. de Pablo. 2007. A coarse grain model for DNA. *J. Chem. Phys.* 126:084901.

117. Sambriski, E., D. Schwartz, and J. De Pablo. 2009. A mesoscale model of DNA and its renaturation. *Biophys. J.* 96:1675–1690.

118. Hinckley, D. M., G. S. Freeman, J. K. Whitmer, and J. J. De Pablo. 2013. An experimentally-informed coarse-grained 3-site-per-nucleotide model of DNA: Structure, thermodynamics, and dynamics of hybridization. *J. Chem. Phys.* 139:10B604_1.

119. Li, W., P. G. Wolynes, and S. Takada. 2011. Frustration, specific sequence dependence, and nonlinearity in large-amplitude fluctuations of allosteric proteins. *Proc. Natl. Acad. Sci. U. S. A.* 108:3504–3509.

120. Langowski, J. 2006. Polymer chain models of DNA and chromatin. *Eur. Phys. J. E.* 19:241–249.

121. Hur, J. S., E. S. Shaqfeh, and R. G. Larson. 2000. Brownian dynamics simulations of single DNA molecules in shear flow. *J. Rheol.* 44:713–742.

122. Korolev, N., Y. Fan, A. P. Lyubartsev, and L. Nordenskiöld. 2012. Modelling chromatin structure and dynamics: status and prospects. *Curr. Opin. Struct. Biol.* 22:151–159.

123. Grigoryev, S. A., G. Arya, S. Correll, C. L. Woodcock, and T. Schlick. 2009. Evidence for heteromorphic chromatin fibers from analysis of nucleosome interactions. *Proc. Natl. Acad. Sci. U. S. A.* 106:13317–13322.

124. Wedemann, G., and J. Langowski. 2002. Computer simulation of the 30-nanometer chromatin fiber. *Biophys. J.* 82:2847–2859.

125. Koslover, E. F., C. J. Fuller, A. F. Straight, and A. J. Spakowitz. 2010. Local geometry and elasticity in compact chromatin structure. *Biophys. J.* 99:3941–3950.

126. Korolev, N., L. Nordenskioeld, and A. P. Lyubartsev. 2016. Multiscale coarse-grained modelling of chromatin components: DNA and the nucleosome. *Adv. Colloid Interface Sci.* 232:36–48.

127. Korolev, N., A. P. Lyubartsev, and L. Nordenskiöld. 2006. Computer modeling demonstrates that electrostatic attraction of nucleosomal DNA is mediated by histone tails. *Biophys. J.* 90:4305–4316.

128. Liu, Y., C. Lu, Y. Yang, Y. Fan, R. Yang, C.-F. Liu, N. Korolev, and L. Nordenskiöld. 2011. Influence of histone tails and H4 tail acetylations on nucleosome–nucleosome interactions. *J. Mol. Biol.* 414:749–764.

129. Lyubartsev, A. P., N. Korolev, Y. Fan, and L. Nordenskiöld. 2015. Multiscale modelling of nucleosome core particle aggregation. *J. Phys. Condens. Matter.* 27:064111.

130. Ozer, G., A. Luque, and T. Schlick. 2015. The chromatin fiber: multiscale problems and approaches. *Curr. Opin. Struct. Biol.* 31:124–139.

131. Allison, S., R. Austin, and M. Hogan. 1989. Bending and twisting dynamics of short linear DNAs. analysis of the triplet anisotropy decay of a 209 base pair fragment by Brownian simulation. *J. Chem. Phys.* 90:3843–3854.

132. Strick, T. R., J.-F. Allemand, D. Bensimon, A. Bensimon, and V. Croquette. 1996. The elasticity of a single supercoiled DNA molecule. *Science.* 271:1835–1837.

133. Strick, T., J.-F. Allemand, D. Bensimon, and V. Croquette. 1998. Behavior of supercoiled DNA. *Biophys. J.* 74:2016 – 2028.

134. Marko, J. F., and S. Neukirch. 2013. Global force-torque phase diagram for the DNA double helix: Structural transitions, triple points, and collapsed plectonemes. *Phys. Rev. E.* 88:062722.

135. Chirico, G., and J. Langowski. 1994. Kinetics of DNA supercoiling studied by Brownian dynamics simulation. *Biopolymers.* 34:415–433.

136. Pabo, C. O., and R. T. Sauer. 1984. Protein-DNA recognition. *Annu. Rev. Biochem.* 53:293–321.

137. Johnson, D. S., A. Mortazavi, R. M. Myers, and B. Wold. 2007. Genome-wide mapping of in vivo protein-DNA interactions. *Science.* 316:1497–1502.

138. Halford, S. E., and J. F. Marko. 2004. How do site-specific DNA-binding proteins find their targets? *Nucleic Acids Res.* 32:3040–3052.

139. Perkins-Balding, D., D. P. Dias, and A. C. Glasgow. 1997. Location, degree, and direction of DNA bending associated with the Hin recombinational enhancer sequence and Fis-enhancer complex. *J. Bacteriol.* 179:4747–53.

140. Swinger, K. K., and P. A. Rice. 2007. Structure-based analysis of HU-DNA binding. *J. Mol. Biol.* 365:1005–1016.

141. Bétermier, M., D. Galas, and M. Chandler. 1994. Interaction of Fis protein with DNA: Bending and specificity of binding. *Biochimie.* 76:958 – 967.

142. Paramanathan, T., D. Reeves, L. J. Friedman, J. Kondev, and J. Gelles. 2014. A general mechanism for competitor-induced dissociation of molecular complexes. *Nat. Commun.* 5.

143. Parsaeian, A., M. O. de la Cruz, and J. F. Marko. 2013. Binding-rebinding dynamics of proteins interacting nonspecifically with a long DNA molecule. *Phys. Rev. E.* 88:040703.

144. Cocco, S., J. F. Marko, and R. Monasson. 2014. Stochastic ratchet mechanisms for replacement of proteins bound to DNA. *Phys. Rev. Lett.* 112:238101.

145. Chen, C., and R. Bundschuh. 2014. Quantitative models for accelerated protein dissociation from nucleosomal DNA. *Nucleic Acids Res.* 42:9753–9760.

146. Åberg, C., K. E. Duderstadt, and A. M. van Oijen. 2016. Stability versus exchange: a paradox in DNA replication. *Nucleic Acids Res.* 44:4846–4854.

147. Fried, M., and D. Crothers. 1984. Kinetics and mechanism in the reaction of gene regulatory proteins with DNA. *J. Mol. Biol.* 172:263–282.

148. Menetski, J. P., and S. C. Kowalczykowski. 1987. Transfer of recA protein from one polynucleotide to another. kinetic evidence for a ternary intermediate during the transfer reaction. *J. Biol. Chem.* 262:2085–2092.

149. Luo, Y., J. A. North, S. D. Rose, and M. G. Poirier. 2014. Nucleosomes accelerate transcription factor dissociation. *Nucleic Acids Res.* 42:3017–3027.

150. Joshi, C. P., D. Panda, D. J. Martell, N. M. Andoy, T. Y. Chen, A. Gaballa, J. D. Helmann, and P. Chen. 2012. Direct substitution and assisted dissociation pathways for turning off transcription by a MerR-family metalloregulator. *Proc. Natl. Acad. Sci. U. S. A.* 109:15121–6.

151. Geertsema, H. J., A. W. Kulczyk, C. C. Richardson, and A. M. van Oijen. 2014. Single-molecule studies of polymerase dynamics and stoichiometry at the bacteriophage T7 replication machinery. *Proc. Natl. Acad. Sci. U. S. A.* 111:4073–4078.

152. Bell, G. I. 1978. Models for the specific adhesion of cells to cells. *Science.* 200:618–627.

153. Sing, C. E., and A. Alexander-Katz. 2011. Equilibrium structure and dynamics of self-associating single polymers. *Macromolecules.* 44:6962–6971.

154. Pan, C. Q., J. A. Feng, S. E. Finkel, R. Landgraf, D. Sigman, and R. C. Johnson. 1994. Structure of the Escherichia coli Fis-DNA complex probed by protein conjugated with 1,10-phenanthroline copper(i) complex. *Proc. Natl. Acad. Sci. U. S. A.* 91:1721–1725.

155. Pollard, T. D. 2010. A guide to simple and informative binding assays. *Mol. Biol. Cell.* 21:4061–4067.

156. Ninio, J. 1987. Alternative to the steady-state method: derivation of reaction rates from first-passage times and pathway probabilities. *Proc. Natl. Acad. Sci. U. S. A.* 84:663–667.

157. Elf, J., G.-W. Li, and X. S. Xie. 2007. Probing transcription factor dynamics at the single-molecule level in a living cell. *Science.* 316:1191–1194.

158. Kim, S., E. Broströmer, D. Xing, J. Jin, S. Chong, H. Ge, S. Wang, C. Gu, L. Yang, Y. Q. Gao, X.-d. Su, Y. Sun, and X. S. Xie. 2013. Probing allostery through DNA. *Science.* 339:816–819.

159. Hamill, O. P., and B. Martinac. 2001. Molecular basis of mechanotransduction in living cells. *Physiol. Rev.* 81:685–740.

160. Gruenbaum, Y., and R. Foisner. 2015. Lamins: nuclear intermediate filament proteins with fundamental functions in nuclear mechanics and genome regulation. *Annu. Rev. Biochem.* 84:131–164.

161. Tajik, A., Y. Zhang, F. Wei, J. Sun, Q. Jia, W. Zhou, R. Singh, N. Khanna, A. S. Belmont, and N. Wang. 2016. Transcription upregulation via force-induced direct stretching of chromatin. *Nat. Mater.* 15:1287.

162. Cho, S., J. Irianto, and D. E. Discher. 2017. Mechanosensing by the nucleus: From pathways to scaling relationships. *J. Cell Biol.* 216:305–315.

163. Wang, N. 2017. Review of cellular mechanotransduction. *J. Phys. D Appl. Phys.* 50:233002.

164. Kramers, H. A. 1940. Brownian motion in a field of force and the diffusion model of chemical reactions. *Physica.* 7:284 – 304.

165. Hänggi, P., P. Talkner, and M. Borkovec. 1990. Reaction-rate theory: Fifty years after Kramers. *Rev. Mod. Phys.* 62:251–342.

166. Evans, E., and K. Ritchie. 1997. Dynamic strength of molecular adhesion bonds. *Biophys. J.* 72:1541–1555.

167. Dudko, O. K., G. Hummer, and A. Szabo. 2006. Intrinsic rates and activation free energies from single-molecule pulling experiments. *Phys. Rev. Lett.* 96:108101.

168. Dudko, O. K., G. Hummer, and A. Szabo. 2008. Theory, analysis, and interpretation of single-molecule force spectroscopy experiments. *Proc. Natl. Acad. Sci. U. S. A.* 105:15755–15760.

169. Suzuki, Y., and O. K. Dudko. 2010. Single-molecule rupture dynamics on multidimensional landscapes. *Phys. Rev. Lett.* 104:048101.

170. Suzuki, Y., and O. K. Dudko. 2011. Biomolecules under mechanical stress: a simple mechanism of complex behavior. *J. Chem. Phys.* 134:02B616.

171. Vogel, V. 2006. Mechanotransduction involving multimodular proteins: converting force into biochemical signals. *Annu. Rev. Biophys. Biomol. Struct.* 35:459–488.

172. Jaalouk, D. E., and J. Lammerding. 2009. Mechanotransduction gone awry. *Nat. Rev. Mol. Cell Biol.* 10:63–73.

173. Poh, Y. C., S. P. Shevtsov, F. Chowdhury, D. C. Wu, S. Na, M. Dundr, and N. Wang. 2012. Dynamic force-induced direct dissociation of protein complexes in a nuclear body in living cells. *Nat. Commun.* 3:866.

174. Brower-Toland, B. D., C. L. Smith, R. C. Yeh, J. T. Lis, C. L. Peterson, and M. D. Wang. 2002. Mechanical disruption of individual nucleosomes reveals a reversible multistage release of DNA. *Proc. Natl. Acad. Sci. U. S. A.* 99:1960–1965.

175. Bustamante, C., Y. R. Chemla, N. R. Forde, and D. Izhaky. 2004. Mechanical processes in biochemistry. *Annu. Rev. Biochem.* 73:705–748.

176. Pope, L., M. L. Bennink, K. van Leijenhorst-Groener, D. Nikova, J. Greve, and J. Marko. 2005. Single chromatin fiber stretching reveals physically distinct populations of disassembly events. *Biophys. J.* 88:3572–3583.

177. Chen, T.-Y., Y.-S. Cheng, P.-S. Huang, and P. Chen. 2018. Facilitated unbinding via multivalency-enabled ternary complexes: New paradigm for protein–DNA interactions. *Acc. Chem. Res.* 51:860–868.

178. Doucleff, M., and G. M. Clore. 2008. Global jumping and domain-specific intersegment transfer between DNA cognate sites of the multidomain transcription factor Oct-1. *Proc. Natl. Acad. Sci. U. S. A.* 105:13871–13876.

179. Bergqvist, S., V. Alverdi, B. Mengel, A. Hoffmann, G. Ghosh, and E. A. Komives. 2009. Kinetic enhancement of NF-κB$\cdot$ DNA dissociation by IκBα. *Proc. Natl. Acad. Sci. U. S. A.* 106:19328–19333.

180. Alverdi, V., B. Hetrick, S. Joseph, and E. A. Komives. 2014. Direct observation of a transient ternary complex during IκBα-mediated dissociation of NF-κB from DNA. *Proc. Natl. Acad. Sci. U. S. A.* 111:225–230.

181. Luo, Y., J. A. North, S. D. Rose, and M. G. Poirier. 2014. Nucleosomes accelerate transcription factor dissociation. *Nucleic Acids Res.* 42:3017–3027.

182. Kilic, S., A. L. Bachmann, L. C. Bryan, and B. Fierz. 2015. Multivalency governs HP1α association dynamics with the silent chromatin state. *Nat. Commun.* 6:7313.

183. Yang, J., Z. Zhuang, R. M. Roccasecca, M. A. Trakselis, and S. J. Benkovic. 2004. The dynamic processivity of the T4 DNA polymerase during replication. *Proc. Natl. Acad. Sci. U. S. A.* 101:8289–8294.

184. Loparo, J. J., A. W. Kulczyk, C. C. Richardson, and A. M. van Oijen. 2011. Simultaneous single-molecule measurements of phage T7 replisome composition and function reveal the mechanism of polymerase exchange. *Proc. Natl. Acad. Sci. U. S. A.* .

185. Kath, J. E., S. Jergic, J. M. Heltzel, D. T. Jacob, N. E. Dixon, M. D. Sutton, G. C. Walker, and J. J. Loparo. 2014. Polymerase exchange on single DNA molecules reveals processivity clamp control of translesion synthesis. *Proc. Natl. Acad. Sci. U. S. A.* :201321076.

186. Beattie, T. R., N. Kapadia, E. Nicolas, S. Uphoff, A. J. Wollman, M. C. Leake, and R. Reyes-Lamothe. 2017. Frequent exchange of the DNA polymerase during bacterial chromosome replication. *Elife.* 6:e21763.

187. Lewis, J. S., L. M. Spenkelink, S. Jergic, E. A. Wood, E. Monachino, N. P. Horan, K. E. Duderstadt, M. M. Cox, A. Robinson, N. E. Dixon, and A. M. van Oijen. 2017. Single-molecule visualization of fast polymerase turnover in the bacterial replisome. *Elife.* 6:e23932.

188. Scheuermann, J., F. Viti, and D. Neri. 2003. Unexpected observation of concentration-dependent dissociation rates for antibody–antigen complexes and other macromolecular complexes in competition experiments. *J. Immunol. Methods.* 276:129–134.

189. Kozlov, A. G., and T. M. Lohman. 2002. Kinetic mechanism of direct transfer of Escherichia coli SSB tetramers between single-stranded DNA molecules. *Biochemistry.* 41:11611–11627.

190. Kunzelmann, S., C. Morris, A. P. Chavda, J. F. Eccleston, and M. R. Webb. 2010. Mechanism of interaction between single-stranded DNA binding protein and DNA. *Biochemistry.* 49:843–852.

191. Ha, T. 2013. Single-molecule approaches embrace molecular cohorts. *Cell.* 154:723–726.

192. Sidorova, N. Y., T. Scott, and D. C. Rau. 2013. DNA concentration-dependent dissociation of EcoRI: direct transfer or reaction during hopping. *Biophys. J.* 104:1296–1303.

193. Gibb, B., L. F. Ye, S. C. Gergoudis, Y. Kwon, H. Niu, P. Sung, and E. C. Greene. 2014. Concentration-dependent exchange of replication protein A on single-stranded DNA revealed by single-molecule imaging. *PLOS ONE.* 9:1–13.

194. Eggel, A., G. Baravalle, G. Hobi, B. Kim, P. Buschor, P. Forrer, J. S. Shin, M. Vogel, B. M. Stadler, C. A. Dahinden, and T. S. Jardetzky. 2014. Accelerated dissociation of IgE-Fcεri complexes by disruptive inhibitors actively desensitizes allergic effector cells. *J. Allergy Clin. Immunol.* 133:1709–1719.

195. Ma, C. J., B. Gibb, Y. Kwon, P. Sung, and E. C. Greene. 2016. Protein dynamics of human RPA and RAD51 on ssDNA during assembly and disassembly of the RAD51 filament. *Nucleic Acids Res.* 45:749–761.

196. Ivan, T., E. Enkvist, H. Sinijarv, and A. Uri. 2017. Competitive ligands facilitate dissociation of the complex of bifunctional inhibitor and protein kinase. *Biophys. Chem.* 228:17–24.

197. Singh, A. K., M. K. Ekka, A. Kaushik, V. Pandya, R. P. Singh, S. Banerjee, M. Mittal, V. Singh, and S. Kumaran. 2017. Substrate-induced facilitated dissociation of the competitive inhibitor from the active site of o-acetyl serine sulfhydrylase reveals a competitive-allostery mechanism. *Biochemistry.* 56:5011–5025.

198. Spenkelink, L. M., J. S. Lewis, S. Jergic, Z.-Q. Xu, A. Robinson, N. E. Dixon, and A. M. van Oijen. 2019. Recycling of single-stranded DNA-binding protein by the bacterial replisome. *Nucleic Acids Res.* .

199. Dahlke, K., and C. E. Sing. 2017. Facilitated dissociation kinetics of dimeric nucleoid-associated proteins follow a universal curve. *Biophys. J.* 112:543 – 551.

200. Yin, H., M. D. Wang, K. Svoboda, R. Landick, S. M. Block, and J. Gelles. 1995. Transcription against an applied force. *Science.* 270:1653–1657.

201. Wang, M. D., M. J. Schnitzer, H. Yin, R. Landick, J. Gelles, and S. M. Block. 1998. Force and velocity measured for single molecules of RNA polymerase. *Science.* 282:902–907.

202. Maier, B., D. Bensimon, and V. Croquette. 2000. Replication by a single DNA polymerase of a stretched single-stranded DNA. *Proc. Natl. Acad. Sci. U. S. A.* 97:12002–12007.

203. Wuite, G. J., S. B. Smith, M. Young, D. Keller, and C. Bustamante. 2000. Single-molecule studies of the effect of template tension on t7 DNA polymerase activity. *Nature.* 404:103.

204. Eeftens, J. M., S. Bisht, J. Kerssemakers, M. Kschonsak, C. H. Haering, and C. Dekker. 2017. Real-time detection of condensin-driven DNA compaction reveals a multistep binding mechanism. *EMBO J.* 36:3448–3457.

205. Keenholtz, R. A., T. Dhanaraman, R. Palou, J. Yu, D. D'amours, and J. F. Marko. 2017. Oligomerization and ATP stimulate condensin-mediated DNA compaction. *Sci. Rep.* 7:14279.

206. Ganji, M., I. A. Shaltiel, S. Bisht, E. Kim, A. Kalichava, C. H. Haering, and C. Dekker. 2018. Real-time imaging of DNA loop extrusion by condensin. *Science*. 360:102–105.

207. van Mameren, J., M. Modesti, R. Kanaar, C. Wyman, E. J. Peterman, and G. J. Wuite. 2009. Counting RAD51 proteins disassembling from nucleoprotein filaments under tension. *Nature*. 457:745.

208. Bartolo, D., I. Derényi, and A. Ajdari. 2002. Dynamic response of adhesion complexes: Beyond the single-path picture. *Phys. Rev. E*. 65:051910.

209. Evans, E., A. Leung, V. Heinrich, and C. Zhu. 2004. Mechanical switching and coupling between two dissociation pathways in a p-selectin adhesion bond. *Proc. Natl. Acad. Sci. U. S. A.* 101:11281–11286.

210. Sarangapani, K. K., T. Yago, A. G. Klopocki, M. B. Lawrence, C. B. Fieger, S. D. Rosen, R. P. McEver, and C. Zhu. 2004. Low force decelerates l-selectin dissociation from p-selectin glycoprotein ligand-1 and endoglycan. *J. Biol. Chem.* 279:2291–2298.

211. Barsegov, V., and D. Thirumalai. 2005. Dynamics of unbinding of cell adhesion molecules: transition from catch to slip bonds. *Proc. Natl. Acad. Sci. U. S. A.* 102:1835–1839.

212. Pereverzev, Y. V., O. V. Prezhdo, M. Forero, E. V. Sokurenko, and W. E. Thomas. 2005. The two-pathway model for the catch-slip transition in biological adhesion. *Biophys. J.* 89:1446–1454.

213. Pierse, C. A., and O. K. Dudko. 2017. Distinguishing signatures of multipathway conformational transitions. *Phys. Rev. Lett.* 118:088101.

214. Dembo, M., D. Torney, K. Saxman, and D. Hammer. 1988. The reaction-limited kinetics of membrane-to-surface adhesion and detachment. *Proc. R. Soc. Lond. B*. 234:55–83.

215. Thomas, W. E., V. Vogel, and E. Sokurenko. 2008. Biophysics of catch bonds. *Annu. Rev. Biophys.* 37:399–416.

216. Marshall, B. T., M. Long, J. W. Piper, T. Yago, R. P. McEver, and C. Zhu. 2003. Direct observation of catch bonds involving cell-adhesion molecules. *Nature*. 423:190.

217. Kong, F., A. J. García, A. P. Mould, M. J. Humphries, and C. Zhu. 2009. Demonstration of catch bonds between an integrin and its ligand. *The Journal of Cell Biology*. 185:1275–1284.

218. Buckley, C. D., J. Tan, K. L. Anderson, D. Hanein, N. Volkmann, W. I. Weis, W. J. Nelson, and A. R. Dunn. 2014. The minimal cadherin-catenin complex binds to actin filaments under force. *Science*. 346:1254211.

219. Thomas, W. E., E. Trintchina, M. Forero, V. Vogel, and E. V. Sokurenko. 2002. Bacterial adhesion to target cells enhanced by shear force. *Cell.* 109:913–923.

220. Thomas, W. E., L. M. Nilsson, M. Forero, E. V. Sokurenko, and V. Vogel. 2004. Shear-dependent 'stick-and-roll' adhesion of type 1 fimbriated *Escherichia coli*. *Mol. Microbiol.* 53:1545–1557.

221. Guo, B., and W. H. Guilford. 2006. Mechanics of actomyosin bonds in different nucleotide states are tuned to muscle contraction. *Proc. Natl. Acad. Sci. U. S. A.* 103:9844–9849.

222. Kunwar, A., S. K. Tripathy, J. Xu, M. K. Mattson, P. Anand, R. Sigua, M. Vershinin, R. J. McKenney, C. Y. Clare, A. Mogilner, and S. P. Gross. 2011. Mechanical stochastic tug-of-war models cannot explain bidirectional lipid-droplet transport. *Proc. Natl. Acad. Sci. U. S. A.* 108:18960–18965.

223. Leidel, C., R. A. Longoria, F. M. Gutierrez, and G. T. Shubeita. 2012. Measuring molecular motor forces in vivo: implications for tug-of-war models of bidirectional transport. *Biophys. J.* 103:492–500.

224. Biebricher, A., S. Hirano, J. H. Enzlin, N. Wiechens, W. W. Streicher, D. Huttner, L. H. C. Wang, E. A. Nigg, T. Owen-Hughes, Y. Liu, E. Peterman, G. J. L. Wuite, and I. D. Hickson. 2013. Pich: a DNA translocase specially adapted for processing anaphase bridge DNA. *Mol. Cell.* 51:691–701.

225. Akiyoshi, B., K. K. Sarangapani, A. F. Powers, C. R. Nelson, S. L. Reichow, H. Arellano-Santoyo, T. Gonen, J. A. Ranish, C. L. Asbury, and S. Biggins. 2010. Tension directly stabilizes reconstituted kinetochore-microtubule attachments. *Nature.* 468:576.

226. Hong, J., C. Ge, P. Jothikumar, Z. Yuan, B. Liu, K. Bai, K. Li, W. Rittase, M. Shinzawa, Y. Zhang, A. Palin, P. Love, X. Yu, K. Salaita, B. D. Evavold, A. Singer, and C. Zhu. 2018. A TCR mechanotransduction signaling loop induces negative selection in the thymus. *Nat. Immunol.* 19:1379.

227. Dahlke, K., and C. Sing. 2018. Force-extension behavior of DNA in the presence of DNA-bending nucleoid associated proteins. *J. Chem. Phys.* 148:084902.

228. McCauley, M., P. R. Hardwidge, L. J. Maher III, and M. C. Williams. 2005. Dual binding modes for an hmg domain from human hmgb2 on DNA. *Biophys. J.* 89:353–364.

229. McCauley, M. J., E. M. Rueter, I. Rouzina, L. J. Maher III, and M. C. Williams. 2013. Single-molecule kinetics reveal microscopic mechanism by which High-Mobility Group B proteins alter DNA flexibility. *Nucleic Acids Res.* 41:167–181.

230. Reimann, P., G. J. Schmid, and P. Hänggi. 1999. Universal equivalence of mean first-passage time and Kramers rate. *Phys. Rev. E.* 60:R1.

231. Erbaş, A., M. O. de la Cruz, and J. F. Marko. 2018. Effects of electrostatic interactions on ligand dissociation kinetics. *Phys. Rev. E.* 97:022405.

232. Lee, K. S., A. B. Marciel, A. G. Kozlov, C. M. Schroeder, T. M. Lohman, and T. Ha. 2014. Ultrafast redistribution of *E. coli* SSB along long single-stranded DNA via intersegment transfer. *J. Mol. Biol.* 426:2413–2421.

233. Skoko, D., J. Yan, R. C. Johnson, and J. F. Marko. 2005. Low-force DNA condensation and discontinuous high-force decondensation reveal a loop-stabilizing function of the protein Fis. *Phys. Rev. Lett.* 95:208101.

234. Wang, Z., D. A. Potoyan, and P. G. Wolynes. 2016. Molecular stripping, targets and decoys as modulators of oscillations in the NF-κB/IκBα/DNA genetic network. *J. Roy. Soc. Interface.* 13:20160606.

235. Potoyan, D. A., and P. G. Wolynes. 2017. Stochastic dynamics of genetic broadcasting networks. *Phys. Rev. E.* 96:052305.

236. Bednar, J., V. M. Studitsky, S. A. Grigoryev, G. Felsenfeld, and C. L. Woodcock. 1999. The nature of the nucleosomal barrier to transcription: direct observation of paused intermediates by electron cryomicroscopy. *Mol. Cell.* 4:377–386.

237. Hodges, C., L. Bintu, L. Lubkowska, M. Kashlev, and C. Bustamante. 2009. Nucleosomal fluctuations govern the transcription dynamics of RNA polymerase II. *Science.* 325:626–628.

238. Bintu, L., M. Kopaczynska, C. Hodges, L. Lubkowska, M. Kashlev, and C. Bustamante. 2011. The elongation rate of RNA polymerase determines the fate of transcribed nucleosomes. *Nat. Struct. Mol. Biol.* 18:1394.

239. Brennan, L. D., R. A. Forties, S. S. Patel, and M. D. Wang. 2016. DNA looping mediates nucleosome transfer. *Nat. Commun.* 7:13337.

240. Kujirai, T., H. Ehara, Y. Fujino, M. Shirouzu, S.-i. Sekine, and H. Kurumizaka. 2018. Structural basis of the nucleosome transition during RNA polymerase II passage. *Science.* 362:595–598.

241. Amitai, A. 2018. Chromatin configuration affects the dynamics and distribution of a transiently interacting protein. *Biophys. J.* 114:766–771.

242. Dame, R. T. 2005. The role of nucleoid-associated proteins in the organization and compaction of bacterial chromatin. *Mol. Microbiol.* 56:858–870.

243. Song, D., and J. J. Loparo. 2015. Building bridges within the bacterial chromosome. *Trends Genet.* 31:164 – 173.

244. Hodges-Garcia, Y., P. J. Hagerman, and D. E. Pettijohn. 1989. DNA ring closure mediated by protein HU. *J. Biol. Chem.* 264:14621–14623.

245. Khazanov, N., and Y. Levy. 2011. Sliding of p53 along DNA can be modulated by its oligomeric state and by cross-talks between its constituent domains. *J. Mol. Biol.* 408:335 – 355.

246. Givaty, O., and Y. Levy. 2009. Protein sliding along DNA: Dynamics and structural characterization. *J. Mol. Biol.* 385:1087 – 1097.

247. Terakawa, T., and S. Takada. 2015. p53 dynamics upon response element recognition explored by molecular simulations. *Sci. Rep.* 5:17107.

248. Zandarashvili, L., A. Esadze, D. Vuzman, C. A. Kemme, Y. Levy, and J. Iwahara. 2015. Balancing between affinity and speed in target DNA search by zinc-finger proteins via modulation of dynamic conformational ensemble. *Proc. Natl. Acad. Sci. U. S. A.* 112:E5142–E5149.

249. Sharma, S., F. Ding, and N. V. Dokholyan. 2007. Multiscale modeling of nucleosome dynamics. *Biophys. J.* 92:1457 – 1470.

250. Fan, Y., N. Korolev, A. P. Lyubartsev, and L. Nordenskild. 2013. An advanced coarse-grained nucleosome core particle model for computer simulations of nucleosome-nucleosome interactions under varying ionic conditions. *PLOS ONE.* 8:1–16.

251. Freeman, G. S., J. P. Lequieu, D. M. Hinckley, J. K. Whitmer, and J. J. de Pablo. 2014. DNA shape dominates sequence affinity in nucleosome formation. *Phys. Rev. Lett.* 113:168101.

252. Sun, J., Q. Zhang, and T. Schlick. 2005. Electrostatic mechanism of nucleosomal array folding revealed by computer simulation. *Proc. Natl. Acad. Sci. U. S. A.* 102:8180–8185.

253. Arya, G., Q. Zhang, and T. Schlick. 2006. Flexible histone tails in a new mesoscopic oligonucleosome model. *Biophys. J.* 91:133 – 150.

254. Shendruk, T., M. Bertrand, H. deHaan, J. Harden, and G. Slater. 2015. Simulating the entropic collapse of coarse-grained chromosomes. *Biophys. J.* 108:810 – 820.

255. Joyeux, M., and J. Vreede. 2013. A model of H-NS mediated compaction of bacterial DNA. *Biophys. J.* 104:1615 – 1622.

256. Zhang, H., and J. F. Marko. 2010. Intrinsic and force-generated cooperativity in a theory of DNA-bending proteins. *Phys. Rev. E.* 82:051906.

257. Yan, J., R. Kawamura, and J. F. Marko. 2005. Statistics of loop formation along double helix DNAs. *Phys. Rev. E.* 71:061905.

258. Efremov, A. K., R. S. Winardhi, and J. Yan. 2016. Transfer-matrix calculations of dna polymer micromechanics under tension and torque constraints. *Phys. Rev. E.* 94:032404.

259. Afflerbach, H., O. Schrder, and R. Wagner. 1998. Effects of the Escherichia coli DNA-binding protein H-NS on rRNA synthesis in vivo. *Mol. Microbiol.* 28:641–653.

260. Chen, T.-Y., A. G. Santiago, W. Jung, Ł. Krzemiński, F. Yang, D. J. Martell, J. D. Helmann, and P. Chen. 2015. Concentration-and chromosome-organization-dependent regulator unbinding from dna for transcription regulation in living cells. *Nat. Commun.* 6:7445.

261. Holmes, V. F., and N. R. Cozzarelli. 2000. Closing the ring: Links between SMC proteins and chromosome partitioning, condensation, and supercoiling. *Proc. Natl. Acad. Sci. U. S. A.* 97:1322–1324.

262. Cunha, S., C. L. Woldringh, and T. Odijk. 2001. Polymer-mediated compaction and internal dynamics of isolated Escherichia coli nucleoids. *J. Struct. Biol.* 136:53–66.

263. Wang, J. C. 1996. DNA topoisomerases. *Annu. Rev. Biochem.* 65:635–692. PMID: 8811192.

264. Zechiedrich, E. L., A. B. Khodursky, S. Bachellier, R. Schneider, D. Chen, D. M. J. Lilley, and N. R. Cozzarelli. 2000. Roles of topoisomerases in maintaining steady-state DNA supercoiling in Escherichia coli. *J. Biol. Chem.* 275:8103–8113.

265. Miller, W. G., and R. W. Simons. 1993. Chromosomal supercoiling in Escherichia coli. *Molecular Microbiology.* 10:675–684.

266. Drlica, K. 1984. Biology of bacterial deoxyribonucleic acid topoisomerases. *Microbiol. Rev.* 48:273–289.

267. Funnell, B., T. A. Baker, and A. Kornberg. 1986. Complete enzymatic replication of plasmids containing the origin of the Escherichia coli chromosome. *J. Biol. Chem.* 261:5616–5624.

268. Liu, L. F., and J. C. Wang. 1987. Supercoiling of the DNA template during transcription. *Proc. Natl. Acad. Sci. U. S. A.* 84:7024–7027.

269. Bustamante, C., Z. Bryant, and S. B. Smith. 2003. Ten years of tension: single-molecule DNA mechanics. *Nature.* 421:423–427.

270. Strick, T., J.-F. Allemand, V. Croquette, and D. Bensimon. 2000. Twisting and stretching single DNA molecules. *Progress in Biophysics and Molecular Biology.* 74:115 – 140.

271. Schlick, T., and W. K. Olson. 1992. Supercoiled DNA energetics and dynamics by computer simulation. *J. Mol. Biol.* 223:1089–1119.

272. Mitchell, J., C. Laughton, and S. A. Harris. 2011. Atomistic simulations reveal bubbles, kinks and wrinkles in supercoiled DNA. *Nucleic Acids Res.* 39:3928–3938.

273. Harris, S. A., C. A. Laughton, and T. B. Liverpool. 2007. Mapping the phase diagram of the writhe of DNA nanocircles using atomistic molecular dynamics simulations. *Nucleic Acids Res.* 36:21–29.

274. Ding, Y., C. Manzo, G. Fulcrand, F. Leng, D. Dunlap, and L. Finzi. 2014. DNA supercoiling: a regulatory signal for the λ repressor. *Proc. Natl. Acad. Sci. U. S. A.* 111:15402–15407.

275. Klenin, K. V., A. V. Vologodskii, V. V. Anshelevich, A. M. Dykhne, and M. D. Frank-Kamenetskii. 1991. Computer simulation of DNA supercoiling. *J. Mol. Biol.* 217:413–419.

276. Vologodskii, A. V., and N. R. Cozzarelli. 1994. Conformational and thermodynamic properties of supercoiled DNA. *Annu. Rev. Bioph Biom.* 23:609–643. PMID: 7919794.

277. Huang, J., T. Schlick, and A. Vologodskii. 2001. Dynamics of site juxtaposition in supercoiled DNA. *Proc. Natl. Acad. Sci. U. S. A.* 98:968–973.

278. Schlick, T. 1995. Modeling superhelical DNA: recent analytical and dynamic approaches. *Curr. Opin. Struct. Biol.* 5:245–262.

279. Marko, J. F., and E. D. Siggia. 1994. Fluctuations and supercoiling of DNA. *Science.* 265:506–508.

280. Lim, C. J., S. Y. Lee, J. Teramoto, A. Ishihama, and J. Yan. 2013. The nucleoid-associated protein Dan organizes chromosomal dna through rigid nucleoprotein filament formation in E. coli during anoxia. *Nucleic Acids Res.* 41:746–753.

281. Lee, S. Y., C. J. Lim, P. Dröge, and J. Yan. 2015. Regulation of bacterial DNA packaging in early stationary phase by competitive DNA binding of Dps and IHF. *Sci. Rep.* 5:18146.

282. Spitzer, J. 2011. From water and ions to crowded biomacromolecules: in vivo structuring of a prokaryotic cell. *Microbiol. Mol. Biol. Rev.* 75:491–506.

283. Ellis, R. J. 2001. Macromolecular crowding: an important but neglected aspect of the intracellular environment. *Curr. Opin. Struct. Biol.* 11:114–119.

Appendix A: Supplemental figures for Chapter 2

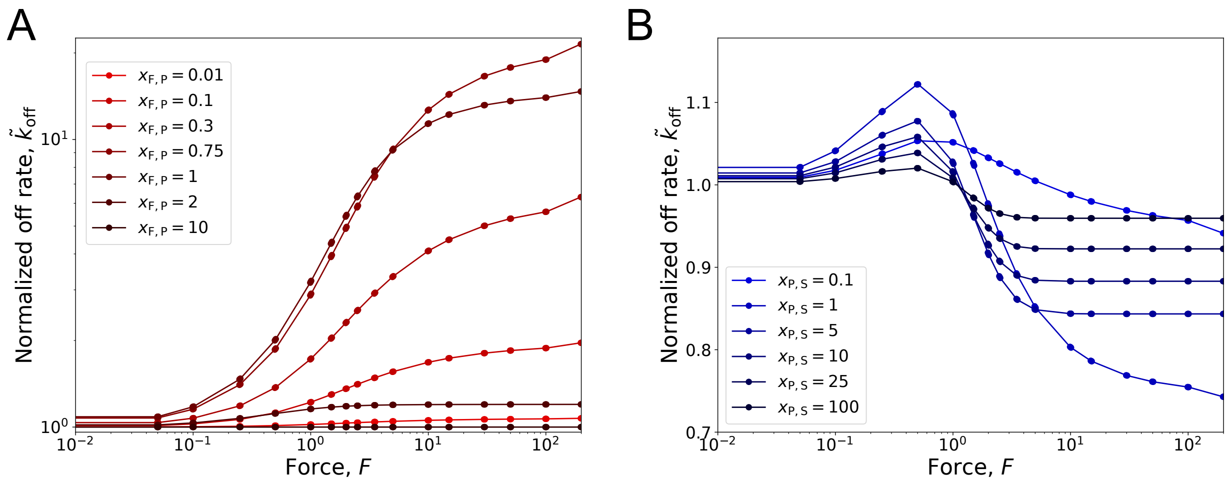

Figure A.1: **A:** Normalized dissociation rate, $\tilde{k}_{\mathrm{off}}$, for the theoretical model with force-dependent partial dissociation ($x_{\mathrm{F,P}} > 0$, increasing from light to dark red) and force-independent facilitated dissociation ($x_{\mathrm{P,S}} = 0$). **B:** Normalized dissociation rate, $\tilde{k}_{\mathrm{off}}$, for the theoretical model with force-independent partial dissociation ($x_{\mathrm{F,P}} = 0$) and force-dependent facilitated dissociation ($x_{\mathrm{P,S}} = 0$, increasing from light to dark blue). Plots show results for $c = 100$ μm and $\theta_0 = \pi/3$.

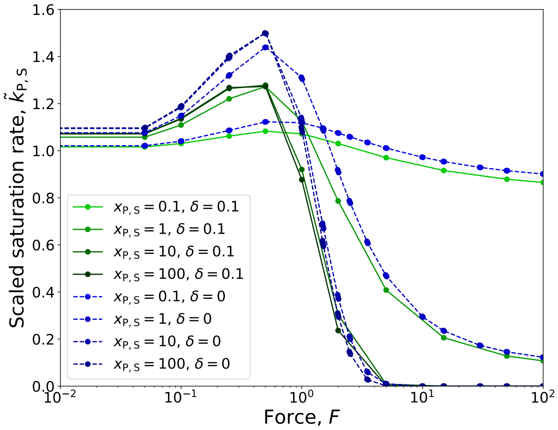

Figure A.2: Scaled saturation rate, $\tilde{k}_{\mathrm{P,S}}$, for the theoretical model with an additional free energy term included to account for excluded volume effects. Here, the free energy is given by $\mathcal{F} = \tilde{U}_B(\theta) - 2b_0 f \cos\theta + \delta\theta^2$, where $\delta = 0.1$ governs the effective stiffness imparted by excluded volume. This expression is used to compute $\langle k_{\mathrm{P,S}}(c, f)\rangle$ as in Eq. 10 in the main text. Scaled rate with excluded volume is shown by the solid green lines, with increasing $x_{\mathrm{P,S}}$ from light to dark green. Results for the theory without excluded volume are shown for comparison by dashed blue lines (increasing $x_{\mathrm{P,S}}$ from light to dark blue). Bending stiffness imparted by excluded volume effects reduces the non-monotonicity of $\tilde{k}_{\mathrm{P,S}}$.

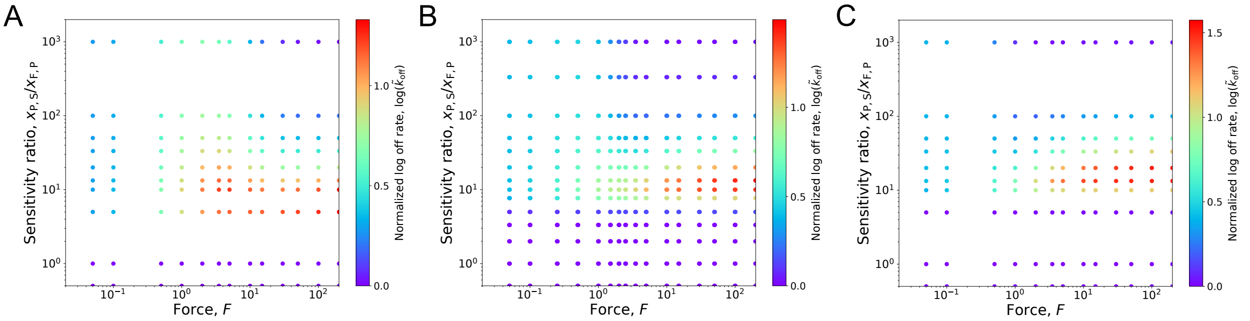

Figure A.3: Normalized dissociation rates, $\tilde{k}_{\mathrm{off}}$ for various sensitivity ratios, $x_{\mathrm{P,S}}/x_{\mathrm{F,P}}$, and forces, f. Value of $\tilde{k}_{\mathrm{off}}$ is indicated by color from purple to red for slow to fast rates for **A:** $\theta_0 = \pi/6$, **B:** $\theta_0 = \pi/3$, and **C:** $\theta_0 = \pi/2$.